CRANFIELD UNIVERSITY

ERIKA QUARANTA

NOISE RADIATION FROM A DUCTED ROTOR IN A SWIRLING-TRANSLATING FLOW

SCHOOL OF ENGINEERING

PhD THESIS

CRANFIELD UNIVERSITY

SCHOOL OF ENGINEERING

PhD THESIS

Academic Year 2009-10

ERIKA QUARANTA

Noise radiation from a ducted rotor in a swirling-translating flow

Supervisor: Prof. Dimitris Drikakis

December 2009

Abstract

This PhD dissertation investigates the noise radiation produced by a rotor inside a duct, which is convected by a swirling-translating mean flow. The study is based on an extension of Gennaretti's and Morino's boundary element method to the frequency domain for scattering problems in conjunction with a spinning rotor source model in the presence of a swirling-translating flow. Firstly, two different source models of the rotor are analyzed in absence of mean flow. The parametric study of the two dipole components distributed over a ring or a disc shows that the source radius is a crucial parameter. The scattered pressure directivity patterns of the ring and disc source models are in perfect agreement when a particular ratio between the two model radii is adopted. Therefore, the present analysis justifies the preference for the ring source model due to its simplicity. The proposed formulation is validated by means of exact solutions and used to investigate the effects of the translating flow Mach number and swirling flow angular velocity on noise radiation both in the far and in the near field. The scattered sound is highly affected by the convecting mean flow. The modal content of the scattered field increases when increasing the translating flow Mach number, while a swirling flow leads to a reduction of the mode propagation, if co-rotating with respect to the azimuthal order of the spinning source, or an increase of the modal content, if counter-rotating with respect to the source. This is clearly confirmed by the scattered pressure patterns and levels both in the far and in the near field for all the source frequencies. In general, the mean translating flow moves the main lobes of the directivity patterns downstream, whereas in some cases the mean swirling flow appears to neglect this effect and the downstream lobe is completely shifted. However, the investigation on the in-duct propagation shows that the main effect of the convecting mean flow is to change the modal duct characteristics, more than the pattern itself. This results in turn in the strong modification of the patterns noted in the far field.

Acknowledgements

I am very grateful to my advisor Prof. Dimitris Drikakis, who gave me the opportunity to join the fluid mechanics and computational science group of the aerospace department in Cranfield University. I would like to thank his willing to assist me till the end of this research project in spite of all my personal difficulties.

I also want to thank the patience of Dr. Panagiota Pantazopoulou, who always had a good word for me and helped me to find the right track for my research; and Dr. Evgeniy Shapiro and Dr. Vladimir Titarev, who often gave me a hand with all the computer matters.

A very special thank goes to my husband Alessandro, who affectionally supported me both emotionally and financially, not only during the years of this PhD, but also for a very long time of my life. I want to dedicate my thesis to him. I cannot end without mentioning my two and half little kids, Gaia, Mirko, and my future little girl, Zoe, who accompanied me all the time during the whole period of the PhD.

Finally, I want to thank the European Friendcopter project for the bursary I received for the PhD.

Contents

List of Figures

List of Tables

Nomenclature

(x, r, ψ)	duct cylindrical coordinates
α	angle, dummy variable
χ^I	$\partial\phi^I/\partial n$
δ	Dirac's function
ω	radial frequency, $2\pi f$
Ω_∞	mean flow angular velocity
$\mathbf{\Omega}(t)$	body-space rotation, $d\mathbf{U}/dt = \mathbf{U\Omega}$
$\mathbf{\Omega}_\infty$	uniform antisymmetric rotation matrix, Eq. (3.76)
ϕ	velocity potential
Π	power level
ψ_1	$\psi_s - \psi$
$\Psi_n(r, \psi)$	cross section duct modes
ρ	density
ϱ	$\|\boldsymbol{\varrho}\|$
$\boldsymbol{\varrho}$	$\boldsymbol{\xi}\ (\mathbf{x}, t) - \boldsymbol{\xi}\ (\mathbf{x}_\star, t_\star)$
$\check{\varrho}$	distance between the source and the evaluation points increased by the convecting factor$(1 + M_r)$ in the swirling-translating mean flow case, Eq. (3.77)
Θ	retarded time coefficient matrix, Eqs. (3.94), (3.96), (3.98)

θ	time delay due to compressibility, positive root of $g(t) = t - t_\star + \varrho/c = 0$, Eqs. (3.86), (3.78)
$\tilde{\theta}$	$(R_\beta + \mathbf{M_0} \cdot \mathbf{R})/(c\beta^2)$
τ	time, undisturbed air frame of reference
$\boldsymbol{\xi}$	position vector, undisturbed air frame of reference, Eq. (3.57)
a	duct radius, length scale
$A_{mn}(r)$	duct radial modes
B	integral coefficient matrix, Eqs. (3.93a), (3.95a), (3.97a)
b	rotor disc radius
B_{mn}	cylindrical duct mode amplitudes
C	integral coefficient matrix, Eqs. (3.93b), (3.95b), (3.97b)
c	speed of sound
C_n	axial duct mode amplitude
D	integral coefficient matrix, Eqs. (3.93c), (3.95c), (3.97c)
D	radius of the circle where the pressure is evaluated
$E(\mathbf{x})$	domain function, Eq. (3.31)
f	frequency
f_ψ	drag dipole source strength
f_x	thrust dipole source strength
G	Green's function, Eqs. (3.28), (3.46), (3.60)
G_0	free space Green's function, $-1/(4\pi r)$, $-1/(4\pi R_\beta)$, $-1/(4\pi \breve{\varrho})$
H	integral coefficient matrix, Eqs. (3.93d), (3.97d)
$\mathbf{I}$	identity operator
i	$\sqrt{-1}$

J_m	Bessel functions of order m
k	wavenumber, ω/c
$\mathbf{M}$	Mach vector, $(\mathbf{v_0} + \mathbf{\Omega}(t)\mathbf{x})/c$
M	duct axial Mach number
m	azimuthal mode order
M_n	Mach vector normal component, $\mathbf{M} \cdot \mathbf{n}$
M_t	rotor blade tip Mach number
$\mathbf{M}_\infty$	mean flow translating Mach vector, $\mathbf{v}_\infty/c$
N	number of discretization panels
$\mathbf{n}$	outward normal to S_B
n	radial mode order
$\tilde{N}$	number of interior collocation points for the CHIEF method
p	pressure
P_{ref}	reference power
Q	source strength
q	monopole source strength
$\mathbf{R}$	distance vector between the source and the evaluation points
R	distance vector module, $\|\mathbf{R}\|$
R_β	distance between the source and the evaluation points increased by the convecting factor$(1 + M_r)$ in the translating mean flow case, Eq.(3.43)
S_B	body surface
t	time, body frame of reference
$\mathbf{U}(t)$	rigid-body rotation matrix, Eq. (3.74)
V	volume

$\mathbf{v_0}$	body translation velocity vector
$\mathbf{v}_\infty$	mean flow translating velocity vector, $-\mathbf{v_0}$
$\mathbf{v}$	velocity vector
$X_n(x)$	axial duct modes
$\mathbf{x}$	position vector, body frame of reference
Y	left hand side system matrix, Eq. (3.101a)
Z	right hand side system matrix, Eq. (3.101b)
$\partial/\partial\tilde{n}$	$(\mathbf{n} - \mathbf{M}\cdot\mathbf{n}\,\mathbf{M})\cdot\nabla$
$\partial/\partial n$	normal derivative, $\mathbf{n}\cdot\nabla$

Subscripts

α	first adjacent panel
β	second adjacent panel
δ	third adjacent panel
γ	fourth adjacent panel
B	body quantity
h	hth edge of the panel
i	ith interior collocation point
j	jth panel
k	kth collocation point
m	azimuthal mode order component
n	radial mode order component
s	source variable
V	volume field quantity
x	axial variable

$\star$	evaluation point
∞	ambient / mean flow quantity

Superscripts

θ	quantity evaluated at the retarded time $t_\star - \theta$
I	incident field
S	scattered field
C	integral coefficient matrix for the solution in the least square sense using the CHIEF method
$-$	acoustic perturbation quantity
$\breve{}$	variable in the Prandtl-Glauert space for a translating mean flow
$\cdot$	time derivative
$\prime$	derivative with respect to the argument
$\sim$	integral coefficient matrix related to the interior points for the CHIEF method
$\wedge$	harmonic component, $[\,] = \widehat{[\,]}e^{i\omega t}$

Chapter 1

Introduction

In the last few years noise regulations have become stricter and stricter, thus noise abatement has gained increasing importance in the aerospace sector. In 2006 the ICAO (International Civil Aviation Organization), which defines the certification standard for aircraft noise in annex 16 (Environmental Protection, Volume I), adopted a new noise standard, decreasing the existing noise level accepted for certification. This new standard now applies to newly certificated aircraft and to aircraft for which re-certification is required.

One of the main sources of aircraft noise is the engine. There are several fluid dynamics phenomena involved in the sound generation. Turbulence is mainly responsible for the jet flow noise and the broadband component of turbomachinery noise. Unsteady aerodynamic loads on the compressor, fan and turbine rotor blades, interacting with the stator blade rows, produce tonal noise, which propagates to the far field after being strongly modified by the intake and exhaust ducts.

This research project investigates the effects of the mean swirling-translating flow on the tonal noise generated by a single rotor in a duct. In contrast to the case of purely convected waves in a duct, in swirling flows the waves do not form a complete basis system for all wave types, therefore, they must be constructed numerically. Generally, the effect of the mean flow swirl is to cut on or cut off modes depending on the sense of rotation with respect to the swirl.

In order to tackle the turbomachinery noise problem, several numerical methods have been employed in literature. Computational aeroacoustics (CAA) and finite

element methods (FEM) have been most widely applied for non-uniform mean flows. However, those methods require meshing of the entire fluid volume, therefore, they are generally used in conjunction with surface integral methods, as Kirchhoff and Ffowcs Williams Hawkings, for the propagation in the far field. Boundary element methods (BEM) have the advantage of being less expensive computationally, as they only require meshing of the body boundary surface, but have only been applied to uniform translating mean flow.

In this study, a new possibility for BEM is explored. A BEM formulation is presented, which is an extension of the one proposed by Morino [1] and Gennaretti and Morino [2, 3], to the frequency domain for scattering problems in conjunction with a spinning rotor source model. Specifically, it is based on the formulation developed by Gennaretti and Morino [2] for a frame of reference in rigid motion with respect to the undisturbed air. Therefore, it can form the basis for predicting the sound convected by a mean swirling-translating flow in a duct, by adding the swirl to the translation of the flow.

In order to model the rotor as an acoustic source, an investigation of two different source models for a wide range of frequencies is also carried out in absence of mean flow. Both the thrust and drag dipole acoustic source are considered and the singularities spanned over a ring or a disc inside the duct to assess the effects of the source model on the propagated sound field. They are further extended to the swirling-translating flow case and this analysis is used to define the model more suitable for the results in presence of mean flow.

In summary, this is the list of the tasks of this PhD research project:

1. Investigation of complex, internal aerodynamic flows;

2. Validation of the state-of-the-art of the BEM in the calculation of internal aeroacoustic flows;

3. Improvement of the BEM for internal aeroacoustics;

4. Investigation of the aeroacoustics for ducted rotor;

5. Application of the BEM aeroacoustics for complex internal flow.

1.1 Thesis Outline

The thesis is organized as follows. In Chapter 2 the numerical methods for duct acoustics, the swirling flow analytical investigations, and the rotor acoustic source models proposed in literature are discussed; in Chapter 3 a description of the classical duct acoustic theory, the rotor acoustic source models, and the BEM formulations without and with the mean flow are introduced; in Chapter 4 the rotor source model investigation is presented; in Chapter 5 the effects of the swirling-translating mean flow to the propagation to the far field is analyzed; while, in Chapter 6 the analysis is completed with the results of the propagation in the near field; finally, in Chapter 7 the conclusions and the overview of the possible future work end the thesis.

Chapter 2

Literature Review

In classical aeroacoustics, the noise generated by an aerodynamic source is computed using the Kirchhoff [4] or the Ffowcs Williams and Hawkings [5] formulation, the latter based on the Lighthill's acoustic analogy [6–8]. Both describe the propagation of the pressure fluctuation disturbance from the near to the far field through a boundary integral equation. The substantial difference is that in the Kirchhoff formulation the integral has to be evaluated on a fictitious arbitrary surface, including all the non linearities, while in the Ffowcs Williams and Hawkings' approach the integral is on the actual body surface and the non linearities are modelled through a volume integral (the quadrupole term), which is generally neglected for subsonic motion. These methods have been extensively used for aeroacoustics of external flow. However they are not applicable to internal duct aeroacoustics.

Other methods were developed to investigate the sound propagation in a duct, with and without mean flow. In 1948 an exact solution of the radiation from an unflanged cylinder was calculated by Levine and Schwinger [9] through the Wiener-Hopf technique. Due to the complexity of this solution, many approximate and numerical methods were later developed.

In the early 60's Tyler and Sofrin [10] modelled the radiation from a duct through a superposition of simple sources, as vibrating spheres, one per element of area at the open end. Later in the 80's, Wang and Tszeng [11] developed a new formulation to calculate the impedance of the opening of a finite length cylinder with a spinning source inside. They showed that the degree of interference decreases when the frequency or the duct length increases.

Ray theory was also used for research in this field. This method consists in an analytical approach, useful to analyze high-frequency sound, which can provide, in combination with the Keller's geometrical theory of diffraction (GTD) [12], the order of magnitude of the problem. In this field Chapman [13] did pioneer work. He modelled a duct acoustic mode as a field of rays and evaluated the sound radiated from the end of the duct. Many followed his work. Keith and Peake [14, 15] studied the thin-walled cylinder, both axisymmetric and scarfed, using the GTD combined with the uniform asymptotic technique, in agreement with the exact Wiener-Hopf solution.

Recently, other important techniques, taking advantage of the progress in numerical computation, were developed to attack the problem, such as finite element methods (FEM) and boundary element methods (BEM). FEM has the advantage of handling complex geometries and flows. On the other hand, it requires the discretization of the whole domain, therefore, noise prediction in the far field is computationally highly expensive. Astley and Eversman [16, 17] used FEM to study non-uniform ducts with and without flow. Kagana *et al* [18] studied non-linear acoustics through a FEM scheme, Giljohann and Bittner [19] proposed a time domain FEM formulation. Zhang, Wu, and Lee [20], used a coupled BEM/FEM method to overcome the FEM limits, because computationally expensive.

An interesting formulation close to classical FEM and finite difference (FD) was recently presented by Casalino and Di Francescantonio [21], the Green's function discretization (GFD) method. They took advantage of the physics of the propagation problem using the Green's function as shape function of the numerical discretization. Thus, accuracy with only 3-4 mesh points per wave length was achieved.

More recently, computational aeroacoustics (CAA) methods have been widely applied. CAA is a computational approach for solving the unsteady fluid flow equations using computational fluid dynamics (CFD) methods, with special emphasis on resolving acoustic perturbations [22]. The CAA analysis accounts for the complexity of turbomachinery flow, however, because of the very fine scale necessary for the acoustic analysis, it is computationally very expensive to apply to noise propagation to the far field. Hybrid methods can be used instead to tackle this problem. The CAA method is limited to the near field, whereas propagation to the far field is computed using surface integral methods, which do not require the discretization of the volume field. Two integral methods are generally adopted. The classical Kirchhoff

method [23] (see [24–28] and references therein) and the formulation of the Ffowcs Williams Hawkings method applicable to a permeable surface, see [29], Chap. 11. Recently, the later have been more extensively used [30–34], having few advantages over the Kirchhoff method [35].

Due to its computational advantage, model of the convention of sound in a duct can be more straightforward done by BEM. The method is based on the Kirchhoff-Helmholtz boundary integral equation (BIE). The integral is applied only on the body surface, because at infinity the equation is automatically satisfied, therefore only the body surface has to be discretized. However, the main difficulty with this method is that the integral operator breaks down at certain frequencies, which are called spurious or fictitious roots. It can be shown [36, 37] that an infinite set of wave numbers k exists for which the BIE has a multiplicity of solutions and these values coincide with the "resonant" wave numbers (or eigenvalues) of the associated interior problem. It must be emphasized that this problem is completely unphysical, because there are no real eigenvalues for the original exterior problem. The uniqueness of the exterior problem is not in question [38] and the connection with the interior domain has no physical meaning. The effect arises because of the boundary integral numerical discretization and the ill-conditioning is more severe at high frequency [39] . This problem, combined with the requirement of increasing the discretization elements, makes difficult to use the method at high frequency.

Several methods have been proposed to overcome this difficulty. Among them, in 1968 Schenck proposed a method, known as the combined Helmholtz interior integral equation formulation (CHIEF) method [40], which was extensively used in the literature, because it is easily applicable, regardless of the particular BEM formulation adopted. In order to determine a unique solution, the method adds additional constraints to the numerical system by applying the BIE to the interior problem and imposing that the solution is equal to zero. This solves the ill-conditioning of the system, provided that the internal points used for the additional constraints are carefully selected. Since the CHIEF method is easy to implement, in the present study this method was chosen to deal with the spurious root problem.

Quite a few BEM formulations are proposed in the literature for duct acoustics. Many authors applied BEM to the radiation and scattering of sound in absence of flow. Polacsek and Desbois-Lavergne [41] developed an original coupling between a CFD numerical approach and BEM to study the turbomachinery generation and

radiation of sound. In order to analyze the potentiality of noise reduction of a control grid (wake generator) mounted upstream of the rotor, they used CFD to provide the unsteady force components on the rotor blades and stator vanes as input to the BEM propagation code SysNoise [42].

BEM has been mainly applied to analyze the scattering of sound, in order to account for the surface acoustic shielding effects. In particular, recently, Monoha, Juvigny, and Roux [43] applied the parallel BEM solver BEMUSE, developed at ONERA, to investigate the shielding effect of the airframe for non-conventional installation configurations of the engine. They tested the solver and compared the experimental and computational results, obtained when the airframe scatters the sound produced by the engine. The latter was modelled as a simple point monopole source. However, the comparison suggested that a better model for the source was necessary.

Fan noise shielding was also studied by Chappuis, Ricouard, and Roger [44]. They considered a full aircraft configuration, modelling the engine and nacelle using BEM, using a given modal excitation as the sound source, and modelling the rest of the aircraft by coupling the BEM with the Fast Multipole Method (FMM) [45], to reduce the data storage and computational time. The exact formulation was used only for interations between close areas, while an approximate formulation was used for distant points. The results were compared with experiments.

BEM formulations were also developed to take into account the effect of a convecting mean flow. In 1986, Astley and Bain [46] proposed a BEM formulation for acoustic radiation in moving flows, restricted to uniform low Mach number flows. They applied the BEM to the test case of a pulsanting or juddering sphere [47]. Later, Dunn, Tweed, and Farassat [48, 49] presented a BEM formulation aimed to predict axisymmetric duct fan noise, including the effect of a uniform axial flow and liners. The method was validated through comparison between the predicted resonance wavenumbers for an infinite cylinder and the results evaluated for an actual thin duct. This approach was implemented in the TBIEM3D code developed at NASA Langley Center. Following this methodology, Yang, Wang, and Guan [50] developed a new formulation. The duct scattering problem was decomposed into two parts, one for the duct interior and one for the exterior. They compared their results with the TBIEM3D results and the solution for acoustic scattering by a non-rotating monopole inside the duct [51].

BEM in a uniform flow was also applied to the acoustic radiation from the intake

duct of a turbofan engine by Lidoine *et al* [52]. They performed a parametric study, comparing BEM and an analytical method, taking into account both uniform flow and liners, and introducing the concept of the *nearly uniform flow*. They noted that for a thick duct, the usual boundary conditions [53] on the inlet surface prescribe the presence of a grazing flow, which is incompatible with the assumption of a strictly uniform flow on the inlet lip. Therefore, they applied an approximate solution, including the effect of the flow distortion, only to the intake lip and used the usual uniform flow boundary condition to the overall intake surface. The numerical and analytical results showed a general agreement. Druon, Lidoine, and Roger [54] extended the comparison between analytical and numerical methods to the FEM, using the ACTRAM [55] software by FFT for the FEM and the ACTI3S [45] sofware by EADS-CRC-F for the BEM. They studied the radiation through the engine exhaust, also analyzing the pressure release condition at the duct trailing edge. The results showed that the BEM computations concided with the analytical solution obtained when the Kutta condition was imposed, while the FEM was close to the no-Kutta analytical solution. Wu and Lee [56] also proposed a BEM formulation tailored to be coupled with FEM [20]. The field was decomposed into two regions. The non-uniform flow zone was solved using FEM, while the uniform flow area was solved using BEM in the original coordinates, so that the interface between the two was easily resolved. That formulation was validated against the analytical solution of the acoustic scattering by a pulsanting sphere in a low Mach number flow [47].

In this research project, a BEM formulation is presented, which is based on the formulation proposed by Morino [1] and Gennaretti and Morino [2, 3], extended to the frequency domain for scattering problems. More specifically, the method is based on the BIE initially introduced for incompressible aerodynamic problems [57,58] and later on extended to compressible aerodynamic flows [1, 2] and aeroacoustics [3]. It has the advantage of being applicable to complex 3D duct geometries and having integral coefficient matrices, arising when replacing the BIE with a linear system of algebraic equations, independent of the incident frequency field. Therefore, it is very appealing for multiple frequency computations. Furthermore, Gennaretti and Morino [2] developed an extension of the formulation for a frame of reference in rigid motion with respect to undisturbed air. This formulation can form the basis for predicting the sound convected by a mean swirling-translating flow in a duct, by adding the swirl to the translation of the mean flow. This possibility is explored here with respect to duct aeroacoustics.

Swirling flows have been of interest for turbomachinery applications since the 70's. As opposed to purely convected waves in a duct, for general swirling flows the waves do not form a complete basis system for all wave types and they must be constructed numerically. Kerrebrock [59] was the first to apply the normal mode analysis to the linearized Euler equations of a swirling inviscid compressible flow in an annular duct. More recently, Kousen [60] followed his approach using a spectral method. He defined three families of modes: spinning acoustic waves (Tyler-Sofrin type), nearly convected modes (due to the swirl), and purely convected modes (a continuum of modes), but the physical meaning of the existence of unstable solutions was not completely clear. Driven from the Kousen's classification, which suggested a weak coupling between the pressure and vorticity waves, Golubev and H. Atassi [61] proposed a different modal analysis, by splitting the velocity field into two main parts: a nearly convected (vorticity dominated) and a nearly sonic (pressure dominated) part. The pseudo-spectral technique showed two families of solutions: pressure dominated modes, propagating upstream and downstream, and vorticity dominated modes, strongly dependent on the type of swirl involved. The above study initially focused on a rigid body and a free vortex swirl, but was later extended to a more general swirl profile [62].

Tam and Aurault [63] dealt with the ambiguities which can arise from the modal analysis if the normal modes do not form a complete set, by posing the problem as an initial-value problem. Their results were in agreement with the analysis of Golubev and H. Atassi. They identified two families of modes: acoustic modes, due to the compressibility effect, and rotational modes, due to the centrifugal force. They noted that the so-called purely convected modes do not exist, but are derived by a non-complete analysis of the problem. Golubev and H. Atassi [64] also criticized the pure normal mode approach. They used a combined eigenmode and initial-value analysis to represent the most general upstream disturbances spatially developing in the duct. They also identified that the pressure-dominated modes represent the acoustic part of the solution, while the initial-value solutions lead to the vorticity dominated nearly convected modes.

Later, Cooper and Peake [65] used the multiple-scales method to take into account the duct slow cross-sectional variations on the eigenvalues and eigenfunctions. They also addressed the problem of the conditions for acoustic resonance in the duct. A theoretical model was developed to predict the conditions of instability due to a varying cross section intake and a swirling flow behind the fan [66], because these con-

ditions modify the propagation properties of the modes. In particular, the swirling flow plays a crucial role, because a mode, which can be cut on ahead of the fan, can be cut off by the mean swirl, thus giving rise to trapped waves. They later extended the model in order to establish which characteristics of the geometry and flow influence the mode trapping [67].

The effect of the mean flow swirl on the scattering from a turbomachinery cascade was also object of many studies. H. Atassi *et al* [68] performed a numerical analysis concluding that the swirl has effect on the annular cascade scattering by modifying the number of propagating acoustic modes in the duct; changing the radial variation in the duct; and varying the amplitude and radial phase of the incident disturbance. Cooper and Peake [69] developed an analytical model to predict the rotor-stator interaction noise due to the effect of the rotor wake impinging on the stator row, taking into account the effect of the swirl on both the rotor wake evolution and the acoustic response in the duct. Furthermore, Heaton and Peake [70] completed the study on the instability arising in the swirling flow and corrected a number of errors in the previous analysis. Sawyer, Nallasamy, and Hixon [71] performed a time domain analysis by solving the fully non linear Euler equations and compared the results with the linear theory. Logue and H. Atassi [72] analyzed the blade geometry and mean swirling flow effects on the bandwidth of the mode trapping, which occurs in the rotor-stator interaction.

In the investigation of the noise propagation through a duct, the problem of modelling the rotor as an acoustic source was also considered. In the literature, the modal analysis is widely used to decompose the sound field in actual engine intake ducts [10]. It is common to apply the pressure field derived for a cylinder geometry, or, equivalently, the cylinder annular, to the fan interface and use one or even more different numerical methods to predict sound scattering to the far field. Alternatively, one can model the rotating sound of a ducted rotor field and study the radiation in the far field as a spinning acoustic source. This approach is not generally suitable to model a realistic complex source of noise, but can be used for a parametric study of the duct propagation.

Dunn, Tweed, and Farassat [48] used a set of spinning monopole point sources located on a ring inside the duct. Carley [73] used an integral distribution of spinning sources spanned over a disc. Jeon, Lee, and Choi [74, 75] used the Lowson model for a rotating source [76] to model the fan/compressor and an integral Kirchhoff surface,

including the rotating source, as the stationary source input for the BEM. Chappuis and Ricouard [44] performed an analysis to set up equivalent sources as two rings of spinning point monopoles to model the fan noise modes. Polacsek and Desbois-Lavergne [41], as mentioned above, used a CFD unsteady aerodynamic analysis of the flow around the blades as the acoustic source for BEM. Furthermore, many authors studied the inverse problem, using the reconstruction of simple acoustic sources propagating in a duct from near and far field measurements, e.g. see [77,78].

Here, two models for the rotor source were implemented [79]. The ring source model, spanning the singularities over a ring, and a disc source model, spanning the singularities over a disc. The two are compared in absence of mean flow, then further developed to include the swirling-translating mean flow effect.

Chapter 3

Methodology

Objects of this chapter are the models and methodologies adopted for the analysis of the acoustics of internal flows. The chapter presents the main concepts of acoustics, with particular reference to duct acoustics; a description of two spinning source models adopted to model the rotor as an acoustic source, both in absence of mean flow and extended to the swirling-translating mean flow case; and the BEM formulations: (i) BEM for a stationary body; (ii) BEM for a translating body; (iii) BEM for a body in arbitrary rigid-body motion, further extended to the frequency domain for scattering in a duct with swirling-translating mean flow.

3.1 Acoustic model

In this section the problem of the noise generated by a rotor and propagating through a duct is considered. The wave equation is derived for a fluid at rest, and the classical duct modal acoustic approach is summarized. Furthermore, two spinning rotor source models are presented and compared in absence of mean flow.

3.1.1 Wave equation

In classical linear acoustics the governing equations are derived by the continuity and momentum equations with the assumption of inviscid flow and negligible heat

conductivity. The equations are

$$\frac{\partial \rho}{\partial t} + \rho \nabla \cdot \mathbf{v} = 0, \tag{3.1a}$$

$$\rho \frac{D\mathbf{v}}{Dt} = -\nabla p. \tag{3.1b}$$

It is common to separate the acoustic (unsteady) field from the mean field by introducing

$$p = p_\infty + \bar{p}, \tag{3.2a}$$

$$\rho = \rho_\infty + \bar{\rho}, \tag{3.2b}$$

$$\mathbf{v} = \mathbf{v}_\infty + \bar{\mathbf{v}} \tag{3.2c}$$

where the bar $^-$ indicates acoustic quantities, and the subscript $_\infty$ represents ambient quantities.

Through substitution of Eqs. (3.2) into Eqs. (3.1), in the hypothesis of absence of mean flow ($\mathbf{v}_\infty = 0$), one obtains a linearized form of the governing equations

$$\frac{\partial \bar{\rho}}{\partial t} + \rho_\infty \nabla \cdot \bar{\mathbf{v}} = 0, \tag{3.3a}$$

$$\rho_\infty \frac{\partial \bar{\mathbf{v}}}{\partial t} = -\nabla \bar{p}. \tag{3.3b}$$

The flow field is assumed to be initially irrotational, therefore, Kelvin's theorem yields that it remains irrotational at all times. In such hypothesis, it is possible to define the velocity potential ϕ as

$$\bar{\mathbf{v}} = \nabla \phi. \tag{3.4}$$

The homogeneous wave equation is then derived upon definition of the isentropic speed of sound

$$c = \sqrt{\frac{\partial p}{\partial \rho}}, \tag{3.5}$$

and combination of Eqs. (3.3), as

$$\nabla^2 \phi - \frac{1}{c^2} \frac{\partial^2 \phi}{\partial t^2} = 0. \tag{3.6}$$

Initial conditions $\phi(\mathbf{x}, 0) = 0$ and $\dot{\phi}(\mathbf{x}, 0) = 0$ and boundary conditions complete the problem statement.

When one considers scattering from a tonal source, the velocity potential can be represented in the frequency domain as

$$\phi(\mathbf{x}, t) = \hat{\phi}(\mathbf{x}) e^{i\omega t}, \tag{3.7}$$

where $\omega = 2\pi f$ is the radial frequency. The wave equation (3.6) becomes the famous Helmholtz equation

$$\nabla^2 \hat{\phi} + k^2 \hat{\phi} = 0, \tag{3.8}$$

where k is the wave number defined as $k = \omega/c$.

3.1.2 Duct propagation

Sound waves in a duct can be described as guided wave modes [80]. Through the separation-of-variables technique [81], one can obtain appropriate solutions of the Helmholtz equation (3.8) in the form

$$\hat{\phi}_n(x, r, \psi) = X_n(x) \Psi_n(r, \psi), \tag{3.9}$$

where the X_n and Ψ_n are the modes, or eigenfunctions, respectively in the direction of the duct axis (the x coordinate) and cross section (the r, ψ cylindrical coordinates).

Substitution in Eq. (3.8) leads to the equation

$$\frac{1}{\Psi_n} \left(\frac{\partial^2}{\partial r^2} + \frac{1}{r} \frac{\partial}{\partial r} + \frac{\partial^2}{\partial \psi^2} \right) \Psi_n + \frac{1}{X_n} \frac{\partial^2 X_n}{\partial x^2} = -k^2. \tag{3.10}$$

Since the right-hand side of Eq. (3.10) is a constant, the left hand side must be a constant too. Thus, both the terms of the sum, being dependent on different variables, must be constant, that is

$$\left(\frac{\partial^2}{\partial r^2} + \frac{1}{r} \frac{\partial}{\partial r} + \frac{\partial^2}{\partial \psi^2} \right) \Psi_n + k_n^2 \Psi_n = 0, \tag{3.11a}$$

$$\frac{\partial^2 X_n}{\partial x^2} + (k^2 - k_n^2) X_n = 0, \tag{3.11b}$$

where the k_n are the eigenvalues related to the cross section modes Ψ_n.

Possible solutions of Eq. (3.11) for the axial modes X_n are $C_n e^{\pm i k_{x_n} x}$ where C_n is a constant depending on the boundary conditions and $k_{x_n} = \sqrt{(k^2 - k_n^2)}$ for $k^2 > k_n^2$ or $k_{x_n} = i\sqrt{(k_n^2 - k^2)}$ for $k^2 < k_n^2$.

Therefore, a propagating guided wave is described by the expression

$$\hat{\phi}_n(x,r,\psi) = C_n e^{-ik_{x_n}x}\Psi_n(r,\psi) \quad \text{for} \quad k^2 > k_n^2, \tag{3.12a}$$

$$\hat{\phi}_n(x,r,\psi) = C_n e^{-|k_{x_n}|x}\Psi_n(r,\psi) \quad \text{for} \quad k^2 < k_n^2. \tag{3.12b}$$

Thus, for a given frequency, i.e. a given k, there are a limited number of modes for which $k^2 > k_n^2$, these are propagating modes. There is at least one for which $k_n = 0$ and so Ψ_n is constant, this is the plane wave or fundamental mode. Modes for which $k^2 < k_n^2$ are evanescent, i.e. the disturbance exponentially dies out along x.

The above defines the well-known cutoff frequency concept. If ω is greater than the cutoff frequency, $\omega_{c,n} = c\ k_n$, the mode propagates in the duct and the propagation is dispersive (i.e. different modes propagates at a different phase velocity $v_{ph} = \omega_n/\sqrt{k^2 - k_n^2}$), but below that frequency the mode decays. The total sound field is given by superposition of each nth mode.

For a spinning sound field propagating through a duct, the azimuthal field can also be obtained by superposition of azimuthal modes. Introducing the azimuthal order m, the radial modes $A_{mn}(r)$, associated to the eigenvalues k_{mn} and the axial wave numbers $k_{x_{mn}}$ defined as before, the acoustic field is

$$\hat{\phi}(x,r,\psi) = \sum_{m,\ n} A_{mn}(r) e^{-i(k_{x_{mn}}x + m\psi)}. \tag{3.13}$$

Both k_{mn} and $A_{mn}(r)$ depend on the duct wall boundary condition, therefore they strongly depend on the actual duct geometry.

If the duct is an infinitely long rigid circular cylinder of radius a, the radial modes have the well known expression [81]

$$A_{mn}(r) = B_{mn} J_m(k_{mn} r), \tag{3.14}$$

where B_{mn} are the mode amplitudes, J_m the Bessel functions of order m and k_{mn} the nth solutions of the equations

$$J'_m(k_{mn}a) = 0, \tag{3.15}$$

that is the mathematical formulation of the impermeability boundary condition on the cylinder's walls.

For complex duct geometries the radial modes $A_{mn}(r)$ do not take a closed mathematical form and the eigenvalues k_{mn} vary axially. Therefore, there are cut-on

modes propagating in some regions of the duct and cut-off modes decaying in other ones.

When a uniform translating flow is running at M_∞ inside the cylinder, the axial wave number is modified as [82]

$$k_{x_{mn}} = \frac{-kM_\infty \pm \sqrt{k^2 - (1 - M_\infty^2)k_{mn}^2}}{1 - M_\infty^2}. \tag{3.16}$$

The mode is cut on for $k^2 > (1 - M_\infty^2)k_{mn}^2$ and cut off for $k^2 < (1 - M_\infty^2)k_{mn}^2$. Therefore, the effect of the mean translating uniform flow is to enhance the mode propagation in the duct.

For complex mean flows, as swirling flows, the scenario is not so clearly defined. Analytical solutions are not available and the analysis has to be carried out numerically. Furthermore, the normal mode analysis is not sufficient to completely describe the flow properties, because the modes do not form a complete set, and an initial-value analysis is required [63, 64]. Generally, the presence of the swirl can cut on or cut off modes depending on the sense of rotation with respect to the mean swirl. Modes cut on in absence of mean swirl, but co-rotating with the swirl, are cut off by the swirl effect, whereas modes cut off in absence of mean swirl, but counter-rotating with the swirl, are cut on by the swirl effect [69].

3.1.3 Spinning rotor source models

In linear acoustics the acoustic velocity potential, $\hat{\phi}$, due to the scattering of a tonal source of frequency ω, is given by adding the scattered, ϕ^S, to the incident, ϕ^I, field:

$$\hat{\phi} = \phi^I + \phi^S. \tag{3.17}$$

It is well known that a harmonic force applied to a fluid generates an acoustic dipole field ([81], Chap. 4). Whereas a monopole source radiates equally in all directions, a dipole source is highly directional, thus the monopole strength is represented by a scalar, but the dipole strength is represented by a vector. The loads resulting by the rotor blade aerodynamics are the thrust, directed along the duct axis x, and the drag, directed along the azimuth ψ. The blade thickness itself is also a source of sound and this noise can be modelled as a monopole source. In total, three components are associated to the rotor sound field: a monopole, a thrust dipole and a drag dipole.

Let us consider the incident potential ϕ^I evaluated at the point (x, r, ψ) due to a point source (x_s, r_s, ψ_s). If the source spins around the azimuth ψ_s, the generic tonal source strength Q is decomposed into the azimuthal components

$$Q = \sum_m Q_m(x_s, r_s) e^{-im\psi_s}, \tag{3.18}$$

where the azimuthal order m is a multiple of the number of rotor blades B. Defining the distance between the points (x, r, ψ) and (x_s, r_s, ψ_s) as
$R = [r^2 + r_s^2 - 2rr_s cos(\psi - \psi_s) + (x - x_s)^2]^{1/2}$, and the source strength modules of the monopole, thrust and drag dipoles as q, f_x and f_ψ, respectively, the resulting incident fields for each component m, are given by

$$\phi^I = \frac{-q_m}{4\pi R} e^{-i(kR+m\psi_s)}, \tag{3.19a}$$

$$\phi^I = \frac{-f_{xm}}{4\pi R^2}\left(ik + \frac{1}{R}\right) e^{-i(kR+m\psi_s)}(x - x_s), \tag{3.19b}$$

$$\phi^I = \frac{-f_{\psi m}}{4\pi R^2}\left(ik + \frac{1}{R}\right) e^{-i(kR+m\psi_s)} sin(\psi - \psi_s) r. \tag{3.19c}$$

Equations (3.19a), (3.19b), and (3.19c) are referred to the monopole, thrust, and drag dipole components, respectively.

If the sources are distributed over the rotor disc of radius b (*rotor disc model*), the incident fields of (3.19) are integrated over the rotor disc as

$$\phi^I = \int_0^b \int_0^{2\pi} \frac{-q_m(r_s)}{4\pi R} e^{-i(kR+m\psi_s)} d\psi_s r_s dr_s, \tag{3.20a}$$

$$\phi^I = (x - x_s) \int_0^b \int_0^{2\pi} \frac{-f_{xm}(r_s)}{4\pi R^2}\left(ik + \frac{1}{R}\right) e^{-i(kR+m\psi_s)} d\psi_s r_s dr_s, \tag{3.20b}$$

$$\phi^I = r \int_0^b \int_0^{2\pi} \frac{-f_{\psi m}(r_s)}{4\pi R^2}\left(ik + \frac{1}{R}\right) e^{-i(kR+m\psi_s)} sin(\psi - \psi_s) d\psi_s r_s dr_s \tag{3.20c}$$

Alternatively, if one concentrates the blade loads on an annular ring (*rotor ring model*), the rotor can be modelled as a ring. The source models are modified in

$$\phi^I = \int_0^{2\pi} \frac{-q_m}{4\pi R} e^{-i(kR+m\psi_s)} d\psi_s, \tag{3.21a}$$

$$\phi^I = (x - x_s) \int_0^{2\pi} \frac{-f_{xm}}{4\pi R^2}\left(ik + \frac{1}{R}\right) e^{-i(kR+m\psi_s)} d\psi_s, \tag{3.21b}$$

$$\phi^I = r \int_0^{2\pi} \frac{-f_{\psi m}}{4\pi R^2}\left(ik + \frac{1}{R}\right) e^{-i(kR+m\psi_s)} sin(\psi - \psi_s) d\psi_s. \tag{3.21c}$$

Using the variable $\psi_1 = \psi_s - \psi$, the azimuthal mode decomposition can be introduced

$$\phi^I(x,r,\psi) = \sum_m \phi_m^I(x,r) e^{-im\psi}, \tag{3.22}$$

thus in the disc source models (3.20) the modes ϕ_m^I take the expressions

$$\phi_m^I = \int_0^b \int_0^{2\pi} \frac{-q_m(r_s)}{4\pi R}\, e^{-i(kR+m\psi_1)} d\psi_1 r_s dr_s, \tag{3.23a}$$

$$\phi_m^I = (x-x_s) \int_0^b \int_0^{2\pi} \frac{-f_{xm}(r_s)}{4\pi R^2} \left(ik + \frac{1}{R}\right) e^{-i(kR+m\psi_1)} d\psi_1 r_s dr_s, \tag{3.23b}$$

$$\phi_m^I = -r \int_0^b \int_0^{2\pi} \frac{-f_{\psi m}(r_s)}{4\pi R^2} \left(ik + \frac{1}{R}\right) e^{-i(kR+m\psi_1)} sin\psi_1 d\psi_1 r_s dr_s, \tag{3.23c}$$

and in the ring source models (3.21)

$$\phi_m^I = \int_0^{2\pi} \frac{-q_m}{4\pi R}\, e^{-i(kR+m\psi_1)} d\psi_1, \tag{3.24a}$$

$$\phi_m^I = (x-x_s) \int_0^{2\pi} \frac{-f_{xm}}{4\pi R^2} \left(ik + \frac{1}{R}\right) e^{-i(kR+m\psi_1)} d\psi_1, \tag{3.24b}$$

$$\phi_m^I = -r \int_0^{2\pi} \frac{-f_{\psi m}}{4\pi R^2} \left(ik + \frac{1}{R}\right) e^{-i(kR+m\psi_1)} sin\psi_1 d\psi_1, \tag{3.24c}$$

where R is given by $R = [r^2 + r_s^2 - 2rr_s cos\,\psi_1 + (x-x_s)^2]^{1/2}$.

Integrating by parts the drag dipole source with respect to ψ_1, one can obtain the monopole source integrals multiplied by the factor $imf_{\psi m}/(q_m r_s)$. Therefore, the two integrals are equivalent, with a phase shift of 90 degrees, when r_s is constant (ring source model), and almost equivalent, after integration over r_s, if the point is not too close to the disc source (disc source model).

In the present study, the disc and ring models were compared with regard to the thrust and drag dipole sources. Furthermore, the source strength modules f_{xm} and $f_{\psi m}$ were assumed to be constant and equal to one on the disc.

Note that the above models were derived only by considering the acoustic field relating to concentrated point sources, but the results are similar to the simplified "thickness" and "loading" noise models derived in [79, 83].

3.2 Boundary element method

In this section the BEM formulations employed for the analysis of the duct propagation are presented. Consider a rigid body $\mathscr{B}$ placed inside the fluid volume. At

first, the body is supposed to be at rest and the boundary integral equation (BIE) is derived from the classical linear wave equation (3.6) in the undisturbed air frame of reference. Then, the body is supposed to be moving and the BIE is rewritten in a frame of reference rigidly connected with the body. The latter is applied for the swirling-translating mean flow case. Both formulations are derived in the time domain, but then translated into the frequency domain for scattering problems. Furthermore, the spinning source rotor models modified by the swirling-translating flow convection are presented.

The section also discusses the numerical implementation of the collocation method; the outline of the CHIEF method to overcame the spurious root problem; and some details on the numerical implementation of the element integrals and the MPI parallel version of the code.

3.2.1 Boundary integral equation for a stationary body

The classical linear wave equation (3.6) is rewritten in an integral form by introducing the Green's function G, that satisfies the equation

$$\nabla^2 G - \frac{1}{c^2}\frac{\partial^2 G}{\partial t^2} = \delta(\mathbf{x}-\mathbf{x}_\star)\delta(t-t_\star), \tag{3.25}$$

being $\mathbf{x}$ the emission point and $\mathbf{x}_\star$ the point where the equation is evaluated, subject to the boundary and time conditions

$$\begin{cases} G = 0 & \text{as} \quad \|\mathbf{x}\| \to \infty \\ G = \dot{G} = 0 & \text{as} \quad t \to \infty. \end{cases} \tag{3.26}$$

Here δ is the Dirac's function δ, i.e. a generalized function such that, for whatever function of position $A(\mathbf{x})$ defined in the volume V,

$$\int_V A(\mathbf{x})\delta(\mathbf{x}-\mathbf{x}_\star)dV = A(\mathbf{x}_\star). \tag{3.27}$$

The Green's function, G, in three dimensions is given by

$$G(\mathbf{x}-\mathbf{x}_\star, t-t_\star) = \frac{-1}{4\pi R}\delta(t-t_\star+\theta) = G_0\,\delta(t-t_\star+\theta), \tag{3.28}$$

where $R = \|\mathbf{x}-\mathbf{x}_\star\|$, $G_0 = -1/4\pi R$, the free space Green's function of the Laplace operator), and $\theta(\mathbf{x},\mathbf{x}_\star) = R/c$, the phase lag due to the compressibility, i.e. the time required for a signal to propagate from the source point $\mathbf{x}$ to the reception point $\mathbf{x}_\star$.

The boundary integral representation for the potential outside of the body surface S_B is obtained by

- multiplying Eq. (3.6) by G and Eq. (3.25) by ϕ, subtracting them,
- integrating over the volume V of the acoustic field,
- applying the Green's theorem, i.e.

$$\int_V [A\nabla^2 B - B\nabla^2 A]dV = \int_{S_B} \mathbf{n} \cdot (A\nabla B - B\nabla A)dS \tag{3.29}$$

  ($\mathbf{n}$ is the outward unit normal to the surface, A and B are scalar functions of position), and the property of the Dirac's function delta (3.27),

- integrating with respect to time, using the initial conditions on ϕ and G.

The resulting integral equation is

$$E(\mathbf{x}_\star)\phi(\mathbf{x}_\star, t_\star) = \int_{S_B} \left[G_0 \frac{\partial \phi}{\partial n}(\mathbf{x}, t) - \frac{\partial G_0}{\partial n}\phi(\mathbf{x}, t) + G_0 \frac{\partial \theta}{\partial n}\frac{\partial \phi}{\partial t}(\mathbf{x}, t) \right]^\theta dS, \tag{3.30}$$

with the quantities in $[\dots]^\theta$ evaluated at the retarded time $t = t_\star - \theta$. The quantity E depends on the position of $\mathbf{x}_\star$ point. If $\mathbf{x}_\star$ is in V (exterior problem) or inside the surface S_B (interior problem), Eq. (3.30) is an integral representation (BIR) for $\phi(\mathbf{x}_\star, t_\star)$ in terms of ϕ, $\partial\phi/\partial n$ and $\partial\phi/\partial t$ on S_B, $E = 1$ (exterior problem) or $E = 0$ (interior problem). On the other hand, if $\mathbf{x}_\star$ tends to S_B, Eq. (3.30) has to be modified to take into account that

$$\int_{S_B} A(\mathbf{x})\delta(\mathbf{x} - \mathbf{x}_\star)dS = \frac{1}{2}A(\mathbf{x}_\star) \quad \text{as} \quad \mathbf{x}_\star \to S_B. \tag{3.31}$$

so that Eq. (3.30) yields a compatibility condition among ϕ, $\partial\phi/\partial n$ and $\partial\phi/\partial t$ on S_B (BIE) with $E = 1/2$ for any ϕ satisfying Eq. (3.6).

The normal velocity $\partial\phi/\partial n = \mathbf{v} \cdot \mathbf{n}$ is known from the boundary condition for a rigid stationary body, which states that the normal component of the velocity must vanish at the surface. Therefore, at the surface

$$\frac{\partial \phi}{\partial n} = 0. \tag{3.32}$$

That compatibility equation yields a BIE, which may be used to evaluate ϕ on the body as a function of the boundary condition $\partial\phi/\partial n$.

The linearized Bernoulli's theorem, derived from Eq. (3.3), relates the acoustic pressure $\bar{p}$ to the acoustic velocity potential ϕ as

$$\frac{\partial \phi}{\partial t} + \frac{\bar{p}}{\rho_\infty} = 0. \tag{3.33}$$

Hence, $\bar{p}$ can be directly obtained by (3.33), once the ϕ is known from Eq. (3.30), subject to the boundary condition (3.32).

In the frequency domain, upon substitution of $\phi(\mathbf{x}, t) = \hat{\phi}(\mathbf{x})e^{i\omega t}$, Eq. (3.30) becomes

$$E(\mathbf{x}_\star)\hat{\phi}(\mathbf{x}_\star) = \int_{S_B} e^{-i\omega\theta} \left(G_0 \frac{\partial \hat{\phi}}{\partial n}(\mathbf{x}) - \frac{\partial G_0}{\partial n}\hat{\phi}(\mathbf{x}) + G_0 i\omega \frac{\partial \theta}{\partial n}\hat{\phi}(\mathbf{x}) \right) dS. \tag{3.34}$$

Applying the decomposition $\hat{\phi} = \phi^I + \phi^S$, because the incident potential is a particular solution of the wave equation (3.6), Eq. (3.34) holds for the scattered potential ϕ^S and the boundary condition at the surface (3.32) translates into

$$\frac{\partial \phi^S}{\partial n} = -\frac{\partial \phi^I}{\partial n}. \tag{3.35}$$

The Bernouilli's theorem (3.33) for the scattered pressure p^S in the frequency domain ($\bar{p} = \hat{p}\ e^{i\omega t}$ and $\hat{p} = p^S + p^I$) translates into

$$p^S = -i\omega\rho_\infty \phi^S. \tag{3.36}$$

In the case of lifting bodies, Kelvin's theorem is not applicable to the points in contact with the surface of the body, which then form a surface of discontinuity for the velocity potential, called the wake. Therefore, the application of the Green's theorem to transform a volume integral into a surface integral yields to another term in the BIE (3.30). The wake is modelled using an evolution equation for the velocity potential discontinuity $\Delta\phi$, which states that $\Delta\phi$ remains constant following the wake point and equal to the value it had when it left the trailing edge. The Kutta-Joukowsky hypothesis, that the vorticity at the trailing edge is zero, implies that $\Delta\phi$ on the wake and the body are equal there. This gives the boundary condition on the wake. However, in the present analysis only non-lifting bodies are considered and the effect of the shear layer is neglected.

3.2.2 Boundary integral equation for a translating body

The integral formulation of the linear wave equation (3.6) can be modified to take into account the effect of the body translation [84]. Let us assume that the body

moves with uniform subsonic velocity $\mathbf{v_0}$. The fundamental solution G is obtained by solving the differential equation

$$\nabla^2 G - \frac{1}{c^2}\left(\frac{\partial}{\partial t} - \mathbf{v_0}\cdot\nabla\right)^2 G = \delta(\mathbf{x}-\mathbf{x}_\star)\delta(t-t_\star), \tag{3.37}$$

with the boundary and initial conditions (3.26). In the air frame of reference the fundamental solution is

$$G(\boldsymbol{\xi}-\boldsymbol{\xi}_\star, \tau-\tau_\star) = \frac{-1}{4\pi\varrho}\delta\left(\tau-\tau_\star+\frac{\varrho}{c}\right), \tag{3.38}$$

being $\boldsymbol{\xi} = \mathbf{x} + \mathbf{v_0}t$, $\tau = t$ the transformation between the two frames of reference, and ϱ the distance $\varrho = \|\boldsymbol{\xi}-\boldsymbol{\xi}_\star\|$.

Using the property of the delta function δ, if $f(t)$ is an arbitrary time function and $g(t)$ the argument of the δ function, then

$$\int_{-\infty}^{+\infty} f(t)\delta[g(t)]dt = \sum_i \left[\frac{f}{|\dot{g}|}\right]_{t=t_i}, \tag{3.39}$$

this implies that

$$\delta[g(t)] = \sum_i \frac{\delta(t-t_i)}{|\dot{g}|}, \tag{3.40}$$

for t_i the roots of $g(t)=0$.

In our case $g(\mathbf{x},\mathbf{x}_\star,t,t_\star) = t - t_\star + \varrho/c$, therefore equation $g(t)=0$ leads to equation

$$\beta^2\theta^2 + 2\mathbf{R}\cdot\mathbf{v_0}\theta/c^2 - R^2/c^2 = 0, \tag{3.41}$$

defining $\theta = t_\star - t = \varrho/c$, $\beta = \sqrt{1-M_0^2}$, $\mathbf{M_0} = \mathbf{v_0}/c$, and $\mathbf{R} = \mathbf{x}-\mathbf{x}_\star$. In the hypothesis of subsonic flow, the only positive root of this equation is

$$\theta(\mathbf{x},\mathbf{x}_\star) = \frac{R_\beta - \mathbf{R}\cdot\mathbf{M_0}}{c\beta^2}, \tag{3.42}$$

where

$$R_\beta = \sqrt{\beta^2R^2 + (\mathbf{R}\cdot\mathbf{M_0})^2}. \tag{3.43}$$

Furthermore,

$$\frac{\partial g}{\partial t} = 1 + \frac{\mathbf{v_0}\cdot(\mathbf{R}-\mathbf{v_0}\theta)}{c\varrho}, \tag{3.44}$$

which is the aeroacoustic convecting factor $(1+M_r)$, for M_r the flow Mach number vector projected along the distance vector. Then

$$R_\beta(\mathbf{x},\mathbf{x}_\star) = \varrho\left|\frac{\partial g}{\partial t}\right| = \varrho\ |1+M_r|, \tag{3.45}$$

the distance between the source and reception points increased by the convecting factor. Finally, combining Eq. (3.44) and Eq. (3.38), the fundamental solution in the body frame is

$$G(\mathbf{x}-\mathbf{x}_\star, t-t_\star) = \frac{-1}{4\pi R_\beta}\delta(t-t_\star+\theta). \tag{3.46}$$

Following the standard procedure to obtain the BIE, as explained in the previous section, one obtains

$$\begin{aligned}
&\int_0^\infty \int_V \nabla\cdot(G\nabla\phi - \phi\nabla g)dV\,dt \\
&-\frac{1}{c^2}\int_0^\infty \int_V \left(\frac{\partial}{\partial t} - \mathbf{v_0}\cdot\nabla\right)\left[G\left(\frac{\partial\phi}{\partial t} - \mathbf{v_0}\cdot\nabla\phi\right) - \phi\left(\frac{\partial G}{\partial t} - \mathbf{v_0}\cdot\nabla G\right)\right] dV\,dt \\
&= -\int_0^\infty \int_V \delta(\mathbf{x}-\mathbf{x}_\star)\delta(t-t_\star)\phi\; dV\,dt
\end{aligned} \tag{3.47}$$

Applying the Gauss's theorem and using the boundary conditions at infinity and the initial conditions on the potential and the fundamental solution G, the BIE is written as

$$\begin{aligned}
E(\mathbf{x}_\star)\phi(\mathbf{x}_\star, t_\star) &= \int_0^\infty \int_{S_B}\left(G\frac{\partial\phi}{\partial t} - \phi\frac{\partial G}{\partial n}\right) dS\,dt \\
&+\frac{1}{c^2}\int_0^\infty \int_{S_B}\left[G\left(\frac{\partial\phi}{\partial t} - \mathbf{v_0}\cdot\nabla\phi\right) - \phi\left(\frac{\partial G}{\partial t} - \mathbf{v_0}\cdot\nabla G\right)\right]\mathbf{v_0}\cdot\mathbf{n}\; dS\,dt.
\end{aligned} \tag{3.48}$$

Evaluating $\nabla G = \nabla G_0\delta(t-t_\star+\theta) + G_0\dot{\delta}(t-t_\star+\theta)\nabla\theta$, for $G_0 = -1/(4\pi R_\beta)$, and $\partial G/\partial t = G_0\dot{\delta}(t-t_\star+\theta)$, and using the property of the delta function, finally in the time domain the BIE for a translating mean flow is

$$E(\mathbf{x}_\star)\phi(\mathbf{x}_\star, t_\star) = \int_{S_B}\left[G_0\frac{\partial\phi}{\partial\tilde{n}} - \phi\frac{\partial G_0}{\partial\tilde{n}} + G_0\frac{\partial\phi}{\partial t}\frac{\partial\tilde{\theta}}{\partial\tilde{n}}\right]^\theta dS, \tag{3.49}$$

where

$$\frac{\partial}{\partial\tilde{n}} = (\mathbf{n} - \mathbf{M_0}\cdot\mathbf{n}\;\mathbf{M_0})\cdot\nabla, \tag{3.50}$$

and

$$\tilde{\theta}(\mathbf{x}, \mathbf{x}_\star) = \frac{R_\beta + \mathbf{M_0}\cdot\mathbf{R}}{c\beta^2}. \tag{3.51}$$

The boundary condition on the body surface S_B is written as

$$\frac{\partial\phi}{\partial n} = \mathbf{v_0}\cdot\mathbf{n}. \tag{3.52}$$

The BIE for a scattering problem, translated into the frequency domain, results as

$$E(\mathbf{x}_\star)\hat{\phi}(\mathbf{x}_\star) = \int_{S_B} e^{-i\omega\theta}\left(G_0\frac{\partial\hat{\phi}}{\partial\tilde{n}} - \hat{\phi}\frac{\partial G_0}{\partial\tilde{n}} + G_0 i\omega\frac{\partial\tilde{\theta}}{\partial\tilde{n}}\hat{\phi}\right) dS. \tag{3.53}$$

In terms of scattered potential, it is associated with the boundary condition on the body surface S_B (3.35).

In order to apply the boundary element method, it is common to use the Prandtl-Glauert transformation. Let us assume that the x-axis is aligned with $\mathbf{v_0}$, the dimensionless variables

$$\breve{x} = \frac{x}{\beta}, \quad \breve{y} = y, \quad \breve{z} = z, \tag{3.54}$$

are introduced.

Therefore, $G_0 = -1/(4\pi\breve{R})$, for $\breve{\mathbf{R}} = \breve{\mathbf{x}} - \breve{\mathbf{x}}_\star$, the distance vector in the Prandtl-Glauert coordinates, and $\partial/\partial\tilde{n} = \partial/\partial\breve{n}$, for $\breve{\mathbf{n}}$ the normal vector to the body surface $\breve{S}_B$ in the Prandtl-Glauert space. Defining

$$\breve{\theta} = \frac{\breve{R} - M_0(\breve{x} - \breve{x}_\star)}{c\beta}, \tag{3.55a}$$

$$\breve{\tilde{\theta}} = \frac{\breve{R} + M_0(\breve{x} - \breve{x}_\star)}{c\beta}, \tag{3.55b}$$

Eq. (3.53) rewritten in the Prandtl-Glauert coordinates is

$$E(\breve{\mathbf{x}}_\star)\hat{\phi}(\breve{\mathbf{x}}_\star) = \int_{\breve{S}_B} e^{-i\omega\breve{\theta}} \left(\frac{-1}{4\pi\breve{R}} \frac{\partial\hat{\phi}}{\partial\breve{n}} - \hat{\phi}\frac{\partial}{\partial\breve{n}}\left(\frac{-1}{4\pi\breve{R}}\right) + \frac{-1}{4\pi\breve{R}} i\omega \frac{\partial\breve{\tilde{\theta}}}{\partial\breve{n}}\hat{\phi} \right) d\breve{S}. \tag{3.56}$$

Equation (3.56) formally recalls the BIE in the absence of flow (3.34), plus an extra term due to the difference in the last integral term.

3.2.3 Boundary integral equation for a moving rigid body

Let us consider a body $\mathscr{B}$ moving in arbitrarily prescribed subsonic rigid-body motion, defined as a translation of velocity $\mathbf{v_0}$ plus a rigid-body rotation, $\mathbf{U}(t)$. Define the frame of reference $(\mathbf{x}, t)$ rigidly connected with the body and the frame of reference $(\boldsymbol{\xi}, \tau)$ connected with the undisturbed air. The transformation between the two is

$$\begin{cases} \boldsymbol{\xi}(\mathbf{x}, t) = \mathbf{U}(t)\mathbf{x} + \mathbf{v_0}\ t, \\ \tau = t. \end{cases} \tag{3.57}$$

Following the same procedure as for a translating mean flow [84], Eq. (3.25), defining the Green's function G, can be written in terms of the air variable $(\boldsymbol{\xi}, \tau)$ as

$$\nabla^2 G - \frac{1}{c^2}\frac{\partial^2 G}{\partial\tau^2} = \delta(\boldsymbol{\xi} - \boldsymbol{\xi}_\star)\delta(\tau - \tau_\star), \tag{3.58}$$

subject to the boundary and time conditions

$$\begin{cases} G = 0 & \text{as} \quad \|\boldsymbol{\xi}\| \to \infty \\ G = \dot{G} = 0 & \text{as} \quad \tau \to \infty. \end{cases} \tag{3.59}$$

Equivalently, the fundamental solution G is given by

$$G(\boldsymbol{\xi} - \boldsymbol{\xi}_\star, \tau - \tau_\star) = \frac{-1}{4\pi\varrho}\delta(\tau - \tau_\star + \frac{\varrho}{c}), \tag{3.60}$$

where $\varrho = \|\boldsymbol{\varrho}\|$ and $\boldsymbol{\varrho} = \boldsymbol{\xi}\ (\mathbf{x}, t) - \boldsymbol{\xi}\ (\mathbf{x}_\star, t_\star)$. Using then Eq.(3.40) and the transformation (3.57), for $g(\mathbf{x}, \mathbf{x}_\star, t, t_\star) = t - t_\star + \|\boldsymbol{\xi}\ (\mathbf{x}, t) - \boldsymbol{\xi}\ (\mathbf{x}_\star, t_\star)\|/c$, hence

$$\frac{\partial g}{\partial t} = 1 + \frac{\boldsymbol{\varrho} \cdot \mathbf{U}(t)\mathbf{M}}{\varrho}, \tag{3.61}$$

defining

$$\mathbf{M} = \frac{\mathbf{v}}{c} = \frac{\mathbf{v_0} + \boldsymbol{\Omega}(t)\mathbf{x}}{c}, \tag{3.62}$$

the Mach vector of the point $\mathbf{x}$ as seen by an observer in the body frame of reference, for $\boldsymbol{\Omega}(t)$ the body-space rotation, such that $d\mathbf{U}/dt = \mathbf{U}\boldsymbol{\Omega}$.

For subsonic flow it exists only one root of equation $g(t) = 0$, $t = t_\star - \theta$, where θ is given by

$$\theta = \frac{1}{c}\|\boldsymbol{\xi}\ (\mathbf{x}, t_\star - \theta) - \boldsymbol{\xi}\ (\mathbf{x}_\star, t_\star)\| \tag{3.63}$$

Therefore, the fundamental solution of the wave equation G in the body frame of reference is

$$G(\mathbf{x} - \mathbf{x}_\star, t - t_\star) = \frac{-1}{4\pi\breve{\varrho}}\delta(t - t_\star + \theta), \tag{3.64}$$

where the quantity $\breve{\varrho}$ is defined as

$$\breve{\varrho} = \left[\varrho\left|\frac{\partial g}{\partial t}\right|\right]^\theta = \left[\varrho\left|1 + \frac{\boldsymbol{\varrho} \cdot \mathbf{U}(t)\mathbf{M}}{\varrho}\right|\right]^\theta, \tag{3.65}$$

being $\mathbf{U}(t)\mathbf{M}$ the Mach vector of the point $\mathbf{x}$ as seen by an observer in the space frame. Therefore, equivalently to the translating mean flow case, $\breve{\varrho}$ is the distance between the source and the evaluation points increased by the convecting factor $(1 + M_r)$.

The standard procedure to obtain the BIE yields to the equation

$$\begin{aligned} E(\mathbf{x}_\star)\phi(\mathbf{x}_\star, t_\star) &= -\int_0^\infty \int_V \nabla \cdot (G\nabla\phi - \phi\nabla G) dV dt \\ &+ \frac{1}{c^2}\int_0^\infty \int_V \frac{d}{dt}\left(G\frac{d\phi}{dt} - \phi\frac{dG}{dt}\right) dV dt, \end{aligned} \tag{3.66}$$

where d/dt is the time derivative in the body space following a fixed point in the air space, i.e.

$$\frac{d}{dt} = \frac{\partial}{\partial t} - \mathbf{v}\cdot\nabla, \tag{3.67}$$

for ∇ the gradient with respect to the point $\mathbf{x}$ on the body. Using this expression of the time derivative, Eq. (3.66) becomes

$$\begin{aligned} E(\mathbf{x}_\star)\phi(\mathbf{x}_\star,t_\star) &= -\int_0^\infty\int_V \nabla\cdot(G\nabla\phi-\phi\nabla G)\,dV\,dt \\ &- \frac{1}{c^2}\int_0^\infty\int_V \mathbf{v}\cdot\left(G\frac{d\phi}{dt}-\phi\frac{dG}{dt}\right)dV\,dt \\ &+ \frac{1}{c^2}\int_V\left(G\frac{d\phi}{dt}-\phi\frac{dG}{dt}\right)\Bigg|_{t=0}^{t=\infty} dV. \end{aligned} \tag{3.68}$$

Note that the last integral is equal to zero because of the initial conditions on the potential and the fundamental solution G. Since the body moves in a rigid-body motion, $\nabla\cdot\mathbf{v}=0$, then applying the Gauss's theorem, Eq. (3.68) is written as

$$\begin{aligned} E(\mathbf{x}_\star)\phi(\mathbf{x}_\star,t_\star) &= \int_0^\infty\int_{S_B}\left(G\frac{\partial\phi}{\partial n}-\phi\frac{\partial G}{\partial n}\right)dS\;dt \\ &+ \frac{1}{c^2}\int_0^\infty\int_{S_B}\left(G\frac{d\phi}{dt}-\phi\frac{dG}{dt}\right)\mathbf{v}\cdot\mathbf{n}\;dS\;dt, \end{aligned} \tag{3.69}$$

Expanding the fundamental solution G as previously obtained in Eq. (3.64), and defining $G_0=-1/(4\pi\breve{\varrho})$, the terms of Eq. (3.69) are

$$\int_0^\infty\int_{S_B}\left(G\frac{\partial\phi}{\partial n}-\phi\frac{\partial G}{\partial n}\right)dS\;dt = \int_{S_B}\left[G_0\frac{\partial\phi}{\partial n}-\phi\frac{\partial G_0}{\partial n}+G_0\frac{\partial\phi}{\partial t}\frac{\partial\theta}{\partial n}\right]^\theta dS$$

$$\frac{1}{c^2}\int_0^\infty\int_{S_B} G\left(\frac{\partial\phi}{\partial t}-\mathbf{v}\cdot\nabla\phi\right)\mathbf{v}\cdot\mathbf{n}\;dS\;dt = \frac{1}{c^2}\int_{S_B} G_0\left[\left(\frac{\partial\phi}{\partial t}-\mathbf{v}\cdot\nabla\phi\right)\mathbf{v}\cdot\mathbf{n}\right]^\theta dS$$

$$-\frac{1}{c^2}\int_0^\infty\int_{S_B}\phi\left(\frac{\partial G}{\partial t}-\mathbf{v}\cdot\nabla G\right)\mathbf{v}\cdot\mathbf{n}\;dS\;dt = \frac{1}{c^2}\int_{S_B} G_0\left[\frac{\partial\phi}{\partial t}\mathbf{v}\cdot\mathbf{n}+\phi\frac{\partial(\mathbf{v}\cdot\mathbf{n})}{\partial t}\right]^\theta dS$$

$$+\frac{1}{c^2}\int_{S_B}\left[\phi\;\mathbf{v}\cdot\mathbf{n}\;\mathbf{v}\cdot\nabla G_0 - G_0\frac{\partial\phi}{\partial t}\mathbf{v}\cdot\mathbf{n}\;\mathbf{v}\cdot\nabla\theta - G_0\phi\frac{\partial}{\partial t}\left(\mathbf{v}\cdot\mathbf{n}\;\mathbf{v}\cdot\nabla\theta\right)\right]^\theta dS.$$

Combining all the above terms, the solution in the body frame at point $\mathbf{x}_\star$ and time $t_\star$ is

$$\begin{aligned} E(\mathbf{x}_\star)\phi(\mathbf{x}_\star,t_\star) &= \int_{S_B}\left[\frac{-1}{4\pi\breve{\varrho}}\frac{\partial\phi}{\partial\tilde{n}}-\frac{\partial}{\partial\tilde{n}}\left(\frac{-1}{4\pi\breve{\varrho}}\right)\phi+\frac{-1}{4\pi\breve{\varrho}}\frac{\partial\phi}{\partial t}\left(\frac{\partial\theta}{\partial\tilde{n}}+2\frac{\mathbf{M}\cdot\mathbf{n}}{c}\right)\right]^\theta dS \\ &- \int_{S_B}\left[\frac{-1}{4\pi\breve{\varrho}}\phi\frac{\partial}{\partial t}\left(\mathbf{M}\cdot\mathbf{n}\;\mathbf{M}\cdot\nabla\theta-\frac{\mathbf{M}\cdot\mathbf{n}}{c}\right)\right]^\theta dS, \end{aligned} \tag{3.70}$$

where

$$\frac{\partial}{\partial \tilde{n}} = (\mathbf{n} - \mathbf{M} \cdot \mathbf{n}\ \mathbf{M}) \cdot \nabla. \tag{3.71}$$

The problem statement is completed by the boundary condition on the body surface S_B

$$\frac{\partial \phi}{\partial n} = \mathbf{v} \cdot \mathbf{n}, \tag{3.72}$$

where the velocity $\mathbf{v}$ is the velocity of the point on the body surface in the body frame.

This formulation was applied to the particular case of a stationary duct with mean flow, convecting an incident acoustic field due to a rotor tonal source of frequency ω. The flow moves in helicoidal motion, of uniform translating velocity $\mathbf{v}_\infty$, directed along the duct axis x, and uniform angular velocity Ω_∞, swirling around x. The transformation (3.57) translates into

$$\boldsymbol{\xi}(\mathbf{x}, t) = \mathbf{U}_\infty(t)\mathbf{x} - \mathbf{v}_\infty t, \tag{3.73}$$

being $\mathbf{U}_\infty(t)$ the rigid-body rotation matrix

$$\mathbf{U}_\infty(t) = \begin{bmatrix} 1 & 0 & 0 \\ 0 & \cos\,\Omega_\infty t & \sin\,\Omega_\infty t \\ 0 & -\sin\,\Omega_\infty t & \cos\,\Omega_\infty t \end{bmatrix}. \tag{3.74}$$

This is a scattering problem, therefore the formulation has to be translated into the frequency domain. Equation (3.70) becomes

$$E(\mathbf{x}_\star)\hat{\phi}(\mathbf{x}_\star) = \int_{S_B} e^{-i\omega\theta} \left(\frac{-1}{4\pi\breve{\varrho}} \frac{\partial \hat{\phi}}{\partial \tilde{n}} - \frac{\partial}{\partial \tilde{n}} \left(\frac{-1}{4\pi\breve{\varrho}} \right) \hat{\phi} + i\omega\hat{\phi} \frac{-1}{4\pi\breve{\varrho}} \left(\frac{\partial \theta}{\partial \tilde{n}} + 2\frac{\mathbf{M} \cdot \mathbf{n}}{c} \right) \right) dS, \tag{3.75}$$

being the Mach vector $\mathbf{M} = -\mathbf{M}_\infty + (\boldsymbol{\Omega}_\infty \mathbf{x})/c$, for $\mathbf{M}_\infty = \mathbf{v}_\infty/c$, and $\boldsymbol{\Omega}_\infty$ the antisymmetric matrix

$$\boldsymbol{\Omega}_\infty = \begin{bmatrix} 0 & 0 & 0 \\ 0 & 0 & \Omega_\infty \\ 0 & -\Omega_\infty & 0 \end{bmatrix}. \tag{3.76}$$

Following [85], in this specific case the variables in Eq. (3.75) are

$$\breve{\varrho} = \left| (1 - M_\infty^2) c\ \theta + \frac{1}{c}\ \mathbf{x} \cdot (\boldsymbol{\Omega}_\infty \mathbf{U}_\infty(\theta)\mathbf{x}_\star) - \mathbf{M}_\infty \cdot \mathbf{R} \right|, \tag{3.77}$$

θ is the unique positive root of the equation

$$(1-M_\infty^2)\theta^2+\frac{2}{c^2}\,\mathbf{x}\cdot((\mathbf{U}_\infty(\theta)-\mathbf{I})\mathbf{x}_\star)-\frac{2}{c}\,\mathbf{R}\cdot\mathbf{M}_\infty\theta-\frac{R^2}{c^2}=0, \tag{3.78}$$

and $\mathbf{R}$ is defined as $\mathbf{R}=\mathbf{x}-\mathbf{x}_\star$.

By expanding the terms of the BIE (3.75), decomposing $\nabla\hat{\phi}=\partial\hat{\phi}/\partial n\ \mathbf{n}+\nabla_{S_B}\hat{\phi}$, being $\nabla_{S_B}\hat{\phi}$ the gradient over the body surface S_B, and defining $M_n=\mathbf{M}\cdot\mathbf{n}$, Eq. (3.75) becomes

$$\begin{aligned}E(\mathbf{x}_\star)\hat{\phi}(\mathbf{x}_\star) &= \int_{S_B}\frac{-1}{4\pi\breve{\varrho}}(1-M_n^2)\frac{\partial\hat{\phi}}{\partial n}e^{-i\omega\theta}dS-\int_{S_B}\frac{-1}{4\pi\breve{\varrho}}M_n\mathbf{M}\cdot\nabla_{S_B}\hat{\phi}\ e^{-i\omega\theta}dS\\ &+ \int_{S_B}\nabla\left(\frac{-1}{4\pi\breve{\varrho}}\right)\cdot(M_n\mathbf{M}-\mathbf{n})\hat{\phi}\ e^{-i\omega\theta}dS\\ &+ i\omega\left[\int_{S_B}\frac{-1}{4\pi\breve{\varrho}}\nabla\theta\cdot(\mathbf{n}-M_n\mathbf{M})\hat{\phi}\ e^{-i\omega\theta}dS+2\int_{S_B}\frac{-1}{4\pi\breve{\varrho}}\frac{M_n}{c}\hat{\phi}\ e^{-i\omega\theta}dS\right].\end{aligned} \tag{3.79}$$

In order to evaluate the integral terms, the gradients of the source term, $-1/(4\pi\breve{\varrho})$, i.e. the doublet term, and the delay, θ, have to be defined. The former is function of $\nabla\breve{\varrho}$. The gradients of $\breve{\varrho}$ and θ are obtained by deriving Eqs. (3.77) and (3.78), respectively, as

$$\nabla\breve{\varrho} = \begin{cases} f & \text{if } \partial g/\partial t\geq 0,\\ -f & \text{if } \partial g/\partial t<0,\end{cases} \tag{3.80a}$$

$$f = \left((1-M_\infty^2)c+\frac{1}{c}\mathbf{x}\cdot(\mathbf{\Omega}_\infty\mathbf{U}'_\infty(\theta)\mathbf{x}_\star)\right)\nabla\theta+\frac{1}{c}\mathbf{\Omega}_\infty\mathbf{U}_\infty(\theta)\mathbf{x}_\star-\mathbf{M}_\infty, \tag{3.80b}$$

for $\mathbf{U}'_\infty$ the derivative of $\mathbf{U}_\infty$ with respect to θ;

$$\nabla\theta=\frac{c\mathbf{M}_\infty\theta+\mathbf{R}-(\mathbf{U}_\infty(\theta)-\mathbf{I})\mathbf{x}_\star}{c\breve{\varrho}}. \tag{3.81}$$

As mentioned in the previous section, the decomposition $\hat{\phi}=\phi^I+\phi^S$ is applied. Thus, Eq. (3.79) translates in terms of the scattered potential and the boundary condition (3.35) is also valid in the frequency domain.

The linearized Bernouilli's theorem (3.33) is modified as

$$\frac{\partial\phi}{\partial t}+\frac{\bar{p}}{\rho_\infty}+\mathbf{v}\cdot\nabla\phi=0, \tag{3.82}$$

which translates in the frequency domain in terms of the scattered pressure p^S into

$$p^S = -i\omega\rho_\infty\phi^S - \rho_\infty \mathbf{v}\cdot\nabla\phi^S. \tag{3.83}$$

This formulation has the advantage of being suitable to model a wide range of scattering problems in presence of flow. It consists of a suitable model for a wide range of scattering problems in the presence of flow. In fact, for a complex geometry (3.79) can be written for each part of the body in the appropriate frame of reference, if the flow can be modelled as a translation plus a rotation, and the solution is then obtained by a linear superposition.

3.2.4 Spinning rotor source models convected by a swirling-translating uniform flow

In section 3.1.3 a model for the incident spinning rotor source is presented. The model was obtained for the no-flow case, but can be extended to the swirling-translating flow case, using the modified monopole and dipole solution of the wave equation written in the body frame.

Equation (3.19), describing the incident fields evaluated in point $\mathbf{x}$ (x, r, ψ) for each azimuthal component m of point source $\mathbf{x_s}$ (x_s, r_s, ψ_s), is modified into

$$\phi^I = \frac{-q_m}{4\pi\breve{\varrho}} e^{-i(\omega\theta+m\psi_s)}, \tag{3.84a}$$

$$\phi^I = \frac{f_{xm}}{4\pi\breve{\varrho}}\left(\frac{1}{\breve{\varrho}}\frac{\partial\breve{\varrho}}{\partial x_s} + i\omega\frac{\partial\theta}{\partial x_s}\right) e^{-i(\omega\theta+m\psi_s)}, \tag{3.84b}$$

$$\phi^I = \frac{f_{\psi m}}{4\pi\breve{\varrho}}\,\frac{1}{r_s}\left(\frac{1}{\breve{\varrho}}\frac{\partial\breve{\varrho}}{\partial\psi_s} + i\omega\frac{\partial\theta}{\partial\psi_s}\right) e^{-i(\omega\theta+m\psi_s)}. \tag{3.84c}$$

Here $\breve{\varrho}$ is defined as

$$\breve{\varrho} = \left|(1-M_\infty^2)c\;\theta + \frac{1}{c}\;\mathbf{x_s}\cdot(\mathbf{\Omega}_\infty\mathbf{U}_\infty(\theta)\mathbf{x}) - \mathbf{M}_\infty\cdot\mathbf{R}\right|, \tag{3.85}$$

θ is the unique positive root of the equation

$$(1-M_\infty^2)\theta^2 + \frac{2}{c^2}\;\mathbf{x_s}\cdot((\mathbf{U}_\infty(\theta)-\mathbf{I})\mathbf{x}) - \frac{2}{c}\;\mathbf{R}\cdot\mathbf{M}_\infty\theta - \frac{R^2}{c^2} = 0, \tag{3.86}$$

for $\mathbf{R} = \mathbf{x_s} - \mathbf{x}$. Therefore, the derivatives are evaluated by deriving Eqs. (3.85)

and (3.86), as

$$\frac{\partial\theta}{\partial x_s} = \frac{cM_{\infty_x}\theta + (x_s - x)}{\breve{\varrho}c}, \tag{3.87a}$$

$$\frac{\partial\breve{\varrho}}{\partial x_s} = \begin{cases} ((1-M_\infty^2)c + 1/c\ \mathbf{x_s}\cdot(\mathbf{\Omega}_\infty \mathbf{U}'_\infty(\theta)\mathbf{x}))\,\partial\theta/\partial x_s - M_{\infty_x} & \text{if } \partial g/\partial t \geq 0, \\ -((1-M_\infty^2)c + 1/c\ \mathbf{x_s}\cdot(\mathbf{\Omega}_\infty \mathbf{U}'_\infty(\theta)\mathbf{x}))\,\partial\theta/\partial x_s + M_{\infty_x} & \text{if } \partial g/\partial t < 0, \end{cases} \tag{3.87b}$$

$$\frac{\partial\theta}{\partial\psi_s} = \frac{-\Omega_\infty\theta + cM_{\infty_\psi}\theta + (\psi_s - \psi)}{\breve{\varrho}c}, \tag{3.87c}$$

$$\frac{\partial\breve{\varrho}}{\partial\psi_s} = \begin{cases} ((1-M_\infty^2)c + 1/c\ \mathbf{x_s}\cdot(\mathbf{\Omega}_\infty \mathbf{U}'_\infty(\theta)\mathbf{x}))\,\partial\theta/\partial\psi_s - M_{\infty_\psi} & \text{if } \partial g/\partial t \geq 0, \\ -((1-M_\infty^2)c + 1/c\ \mathbf{x_s}\cdot(\mathbf{\Omega}_\infty \mathbf{U}'_\infty(\theta)\mathbf{x}))\,\partial\theta/\partial\psi_s + M_{\infty_\psi} & \text{if } \partial g/\partial t < 0, \end{cases} \tag{3.87d}$$

for M_{∞_x} and M_{∞_ψ} the components of $\mathbf{M}_\infty$ in the axial and azimuthal directions, respectively.

Equivalently, the disc and ring source models (Eqs. (3.20) and (3.21)) modify, respectively, as

$$\phi^I = \int_0^b\int_0^{2\pi} \frac{-q_m(r_s)}{4\pi\breve{\varrho}} e^{-i(\omega\theta + m\psi_s)} d\psi_s r_s dr_s, \tag{3.88a}$$

$$\phi^I = \int_0^b\int_0^{2\pi} \frac{f_{xm}(r_s)}{4\pi\breve{\varrho}} \left(\frac{1}{\breve{\varrho}}\frac{\partial\breve{\varrho}}{\partial x_s} + i\omega\frac{\partial\theta}{\partial x_s}\right) e^{-i(\omega\theta + m\psi_s)} d\psi_s r_s dr_s, \tag{3.88b}$$

$$\phi^I = \int_0^b\int_0^{2\pi} \frac{f_{\psi m}(r_s)}{4\pi\breve{\varrho}} \left(\frac{1}{\breve{\varrho}}\frac{\partial\breve{\varrho}}{\partial\psi_s} + i\omega\frac{\partial\theta}{\partial\psi_s}\right) e^{-i(\omega\theta + m\psi_s)} d\psi_s dr_s, \tag{3.88c}$$

and

$$\phi^I = \int_0^{2\pi} \frac{-q_m}{4\pi\breve{\varrho}} e^{-i(\omega\theta + m\psi_s)} d\psi_s, \tag{3.89a}$$

$$\phi^I = \int_0^{2\pi} \frac{f_{xm}}{4\pi\breve{\varrho}} \left(\frac{1}{\breve{\varrho}}\frac{\partial\breve{\varrho}}{\partial x_s} + i\omega\frac{\partial\theta}{\partial x_s}\right) e^{-i(\omega\theta + m\psi_s)} d\psi_s, \tag{3.89b}$$

$$\phi^I = \int_0^{2\pi} \frac{f_{\psi m}}{4\pi\breve{\varrho}}\ \frac{1}{r_s} \left(\frac{1}{\breve{\varrho}}\frac{\partial\breve{\varrho}}{\partial\psi_s} + i\omega\frac{\partial\theta}{\partial\psi_s}\right) e^{-i(\omega\theta + m\psi_s)} d\psi_s. \tag{3.89c}$$

Introducing the variable $\psi_1 = \psi_s - \psi$ and the azimuthal mode decomposition (3.22), the modes ϕ_m^I take the expressions

$$\phi_m^I = \int_0^b\int_0^{2\pi} \frac{-q_m(r_s)}{4\pi\breve{\varrho}} e^{-i(\omega\theta + m\psi_1)} d\psi_1 r_s dr_s, \tag{3.90a}$$

$$\phi_m^I = \int_0^b\int_0^{2\pi} \frac{f_{xm}(r_s)}{4\pi\breve{\varrho}} \left(\frac{1}{\breve{\varrho}}\frac{\partial\breve{\varrho}}{\partial x_s} + i\omega\frac{\partial\theta}{\partial x_s}\right) e^{-i(\omega\theta + m\psi_1)} d\psi_1 r_s dr_s, \tag{3.90b}$$

$$\phi_m^I = \int_0^b\int_0^{2\pi} \frac{f_{\psi m}(r_s)}{4\pi\breve{\varrho}} \left(\frac{1}{\breve{\varrho}}\frac{\partial\breve{\varrho}}{\partial\psi_s} + i\omega\frac{\partial\theta}{\partial\psi_s}\right) e^{-i(\omega\theta + m\psi_1)} d\psi_1 dr_s, \tag{3.90c}$$

for the disc source model, and

$$\phi_m^I = \int_0^{2\pi} \frac{-q_m}{4\pi\breve{\varrho}} e^{-i(\omega\theta+m\psi_1)} d\psi_1, \tag{3.91a}$$

$$\phi_m^I = \int_0^{2\pi} \frac{f_{xm}}{4\pi\breve{\varrho}} \left(\frac{1}{\breve{\varrho}} \frac{\partial\breve{\varrho}}{\partial x_s} + i\omega \frac{\partial\theta}{\partial x_s} \right) e^{-i(\omega\theta+m\psi_1)} d\psi_1, \tag{3.91b}$$

$$\phi_m^I = \int_0^{2\pi} \frac{f_{\psi m}}{4\pi\breve{\varrho}} \frac{1}{r_s} \left(\frac{1}{\breve{\varrho}} \frac{\partial\breve{\varrho}}{\partial \psi_s} + i\omega \frac{\partial\theta}{\partial \psi_s} \right) e^{-i(\omega\theta+m\psi_1)} d\psi_1, \tag{3.91c}$$

for the ring source model.

3.2.5 Collocation method

The numerical implementation of the BIEs (3.34), (3.53), and (3.79) is subject to a collocation method. In order to solve it computationally, the integral equation is replaced by a linear system of algebric equations. The process by which the linear system of equations is formed is called the boundary element method (BEM). In this section the BEM is presented for both the no-flow and mean flow conditions.

The surface S_B is discretized in N quadrilateral panels, $S_j, j = 1, 2, \ldots, N$, and the variables ϕ^S and $\chi^I := \partial\phi^I/\partial n$ are assumed to be constant on each element surface (zeroth order method). Furthermore, also the quantities M_n and $e^{-i\omega\theta}$ are supposed to be constant on the panel. A collocation point $\mathbf{x}_\star = \mathbf{x}_k$ is placed at the center of each panel and each quantity constant on the panel is evaluated at that point.

The BIEs (3.34), (3.53), and (3.79) must be satisfied at each collocation point, therefore at a given $\mathbf{x}_k$ the following equation, formally the same for all the mean flow conditions, must be satisfied

$$\frac{1}{2}\phi_k^S = \sum_{j=1}^{N} e^{-i\omega\theta_{kj}} \left[-B_{kj}\chi_j^I + H_{kj}\phi_j^S + C_{kj}\phi_j^S + i\omega D_{kj}\phi_j^S \right]. \tag{3.92}$$

Here the quantities are defined differently according to the proper BIE in presence or absence of mean flow.

In the no-flow case, BIE (3.34), the integral coefficients are

$$B_{kj} = \int_{S_j} \frac{-1}{4\pi R_k} dS, \tag{3.93a}$$

$$C_{kj} = \int_{S_j} \frac{\mathbf{R_k} \cdot \mathbf{n}}{4\pi R_k^3} dS, \tag{3.93b}$$

$$D_{kj} = -\frac{1}{c} \int_{S_j} \frac{\mathbf{R_k} \cdot \mathbf{n}}{4\pi R_k^2} dS, \tag{3.93c}$$

$$H_{kj} = 0, \tag{3.93d}$$

and the time delay

$$\theta_{kj} = \frac{R_{kj}}{c}, \quad R_{kj} = \|\mathbf{x}_j - \mathbf{x}_k\|, \tag{3.94}$$

where $\mathbf{x}_j$ is the collocation point of panel S_j, and $\mathbf{R_k}$ is evaluated as $\mathbf{R_k} = \mathbf{x} - \mathbf{x_k}$ for $\mathbf{x} \in S_j$. When the surface is discretized using hyperboloidal panels, the above integrals can be integrated analytically.

In the translating mean flow case, BIE (3.53), the integral coefficients B_{kj} and C_{kj} are formally the same, but defined in the Prandtl-Glauert space, as $\breve{B}_{kj}$ and $\breve{C}_{kj}$. Furthermore, the quantity θ_{kj} is replaced by the quantity $\breve{\theta}_{kj}$ and the last integral term D_{kj} is modified to take into account the modified quantity $\breve{\breve{\theta}}$.

In summary, the integral coefficients are

$$\breve{B}_{kj} = \int_{\breve{S}_j} \frac{-1}{4\pi \breve{R}_k} d\breve{S}, \tag{3.95a}$$

$$\breve{C}_{kj} = \int_{\breve{S}_j} \frac{\breve{\mathbf{R}}_\mathbf{k} \cdot \breve{\mathbf{n}}}{4\pi \breve{R}_k^3} d\breve{S}, \tag{3.95b}$$

$$\breve{D}_{kj} = -\frac{1}{c} \left(\int_{\breve{S}_j} \frac{\breve{\mathbf{R}}_\mathbf{k} \cdot \mathbf{n}}{4\pi \breve{R}_k^2} d\breve{S} - M_0 \int_{\breve{S}_j} \frac{\breve{n}_x}{4\pi \breve{R}_k} d\breve{S} \right), \tag{3.95c}$$

and the time delay

$$\breve{\theta}_{kj} = \frac{\breve{R}_{kj} - M_0(\breve{x} - \breve{x}_\star)}{c}, \quad \breve{R}_{kj} = \|\breve{\mathbf{x}}_j - \breve{\mathbf{x}}_k\|. \tag{3.96}$$

On the other hand, when the effect of the convecting mean swirling-translating flow

is taken into account, BIE (3.79), the integral coefficients are modified as

$$B_{kj} = (1 - M_{n_j}^2) \int_{S_j} \frac{-1}{4\pi \breve{\varrho}_k} dS, \tag{3.97a}$$

$$C_{kj} = (M_{n_j}\mathbf{M}_j - \mathbf{n}_j) \cdot \int_{S_j} \frac{\nabla \breve{\varrho}_k}{4\pi \breve{\varrho}_k^2} dS, \tag{3.97b}$$

$$D_{kj} = (\mathbf{n}_j - M_{n_j}\mathbf{M}_j) \cdot \int_{S_j} \frac{\nabla \theta_k}{4\pi \breve{\varrho}_k} dS + 2\frac{M_{n_j}}{c} \int_{S_j} \frac{-1}{4\pi \breve{\varrho}_k} dS, \tag{3.97c}$$

$$\begin{aligned} H_{kj} = \frac{M_{n_j}}{2}\mathbf{M}_j \cdot \Bigg(& \sum_{h=1}^{4} \int_{\partial S_{jh}} \frac{-1}{4\pi \breve{\varrho}_k} \mathbf{n}_{\partial S_{jh}} dl - \int_{\partial S_{j\alpha 3}} \frac{-1}{4\pi \breve{\varrho}_k} \mathbf{n}_{\partial S_{j\alpha 3}} dl \\ & - \int_{\partial S_{j\beta 4}} \frac{-1}{4\pi \breve{\varrho}_k} \mathbf{n}_{\partial S_{j\beta 4}} dl - \int_{\partial S_{j\gamma 1}} \frac{-1}{4\pi \breve{\varrho}_k} \mathbf{n}_{\partial S_{j\gamma 1}} dl - \int_{\partial S_{j\delta 2}} \frac{-1}{4\pi \breve{\varrho}_k} \mathbf{n}_{\partial S_{j\delta 2}} dl \Bigg), \end{aligned} \tag{3.97d}$$

and the time delay $\theta_{kj} \geq 0$, unique root of the equation

$$(1 - M_\infty^2)\theta_{kj}^2 + \frac{2}{c}\, \mathbf{x}_j \cdot [(\mathbf{U}_\infty(\theta_{kj}) - \mathbf{I})\mathbf{x}_k] - 2\, \mathbf{R}_{kj} \cdot \mathbf{M}_\infty \theta_{kj} - \frac{R_{kj}^2}{c^2} = 0. \tag{3.98}$$

Here the quantities in the integral coefficients are defined as

$$M_{n_j} = \mathbf{M}_j \cdot \mathbf{n}_j, \tag{3.99a}$$

$$\mathbf{M}_j = -\mathbf{M}_\infty + \frac{\mathbf{\Omega}_\infty \mathbf{x}_j}{c}, \tag{3.99b}$$

$$\mathbf{R}_{kj} = \mathbf{x}_j - \mathbf{x}_k. \tag{3.99c}$$

The variables $\breve{\varrho}_k$, $\nabla\breve{\varrho}_k$, and $\nabla\theta_k$ in the integral coefficients are evaluated by means of Eqs. (3.77), (3.78), (3.80), and (3.81), for $\mathbf{x} \in S_j$. Furthermore, the normal $\mathbf{n_j}$ is supposed to be constant on the panel and equal to the one at the center. In this case an analytical integration is not available and a numerical implementation of the integrals has to be used instead. Details on the implementation of the numerical integration are provided in Section 3.2.7.

The integral coefficient H_{kj} is derived from a model of the second term of Eq. (3.79), which is explained in details in the Appendix A. The surface integral is replaced by line integrals over the four edges of the boundary of panel S_j, and line integrals over the edges of the four adjacent panels, identified as $S_{j\alpha}$, $S_{j\beta}$, $S_{j\delta}$, and $S_{j\gamma}$. The vector $\mathbf{n}_{\partial S_{jh}}$ is the outward normal to the edge h of the panel S_j on the same plane of S_j. The other normal vectors $\mathbf{n}_{\partial S_{j\alpha 3}}$, $\mathbf{n}_{\partial S_{j\beta 4}}$, $\mathbf{n}_{\partial S_{j\gamma 1}}$, and $\mathbf{n}_{\partial S_{j\delta 2}}$ are defined equivalently.

It is important to note that the integral coefficients, as defined in Eqs. (3.93), (3.95), and (3.97), are frequency *independent*. This feature is very appealing from

a computational point of view, because, when one has to compute the acoustic response varying the source of the incident field, the integration on each panel only has to be performed once.

Finally, the BIEs (3.34), (3.53), and (3.79) are replaced by a $N \times N$ linear system of algebraic equations

$$\mathrm{Y}\underline{\phi}^S = -\mathrm{Z}\underline{\chi}^I, \tag{3.100}$$

where

$$\mathrm{Y} = \frac{1}{2}\,\mathrm{I} - e^{-i\omega\,\Theta}\,(\mathrm{H} + \mathrm{C} + i\omega\mathrm{D}) \tag{3.101a}$$

$$\mathrm{Z} = e^{-i\omega\,\Theta}\mathrm{B}. \tag{3.101b}$$

The matrix I is the identity matrix and H, C, D, B and Θ are the integral coefficient matrices, as defined in Eqs. (3.93), (3.95), and (3.97). The solution of the system (3.100) yields the unknown scattered velocity potential vector $\underline{\phi}^S$.

Once the scattered velocity potential on the body S_B is known, the same is evaluated in the volume field V (ϕ_V^S) by applying (3.34), (3.53), and (3.79) in the BIR form, i.e. for $E = 1$. The resulting numerical system is

$$\phi_V^S = \mathrm{Y}_V\underline{\phi}^S - \mathrm{Z}_V\underline{\chi}^I, \tag{3.102}$$

where

$$\mathrm{Y}_V = e^{-i\omega\,\Theta_V}\,(\mathrm{H}_V + \mathrm{C}_V + i\omega\mathrm{D}_V) \tag{3.103a}$$

$$\mathrm{Z}_V = e^{-i\omega\,\Theta_V}\mathrm{B}_V. \tag{3.103b}$$

The coefficients H_V, C_V, D_V, B_V and Θ_V are referred to point $\mathbf{x}_\star$ in the volume field.

The scattered pressure in the volume field p_V^S is then obtained by applying the linearized Bernoulli's theorem (3.33) and (3.83).

3.2.6 The spurious root problem and the CHIEF method

As mentioned in Chapter 2, the BEM applicability, especially at high frequency, is subject to the spurious or fictitious root problem [36, 37]. The BIE (3.75) breaks down in correspondence to an infinite set of wave numbers k, coinciding with the "resonant" wave numbers (or eigenvalues) of the associated interior problem, i.e. the

same BIE coupled with the boundary condition on S_B, $\hat{\phi} = 0$. It can be shown [39] that the fictitious frequencies are sparsely distributed when k is small, but, as k increases, they become progressively denser. Asymptotically (as $k \to \infty$) their number is proportional to k^3. From a computational point of view, ill-conditioning is likely to occur for wave numbers k in the immediate vicinity of a critical wave number. The ill-conditioning is consequently more severe when k is large.

The CHIEF method [40] was implemented in this study for addressing the spurious root problem. When one considers the set of linear equations (3.100) at a frequency corresponding to one of the fictitious frequencies, the set is not linearly independent. In application, this means that the resulting coefficient matrix for the discretized exterior problem is singular or ill-conditioned. In order to determine a unique solution, additional constraints for the system are required and these can be found by applying the BIE to the interior problem.

Schenck suggested a numerical procedure to obtain an approximation to the common solution of the exterior and interior problem. When only the exterior problem is considered, the resulting system of equations is $N \times N$ (for N surface elements). If the wave number does not coincide with a fictitious wave number, the system can be solved through a regular numerical technique (e.g. the LU factorization). When the system is ill-conditioned, due to the fictitious wave number problem, Schenck suggested that one add $\tilde{N}$ more equations that satisfy the interior equation at $\tilde{N}$ interior points. He also suggested choosing $\tilde{N} << N(k)$ points (the number $\tilde{N}$ is generally frequency dependent) in the interior domain, $\mathbf{x_i}$. The additional equations take the form

$$0 = \tilde{\mathrm{Y}}\underline{\phi}^S - \tilde{\mathrm{Z}}\underline{\chi}^I, \tag{3.104}$$

where

$$\tilde{\mathrm{Y}} = e^{-i\omega\,\tilde{\Theta}}\left(\tilde{\mathrm{H}} + \tilde{\mathrm{C}} + i\omega\tilde{\mathrm{D}}\right) \tag{3.105a}$$

$$\tilde{\mathrm{Z}} = e^{-i\omega\,\tilde{\Theta}}\tilde{\mathrm{B}}. \tag{3.105b}$$

with the integral coefficients, $\tilde{\mathrm{H}}$, $\tilde{\mathrm{C}}$, $\tilde{\mathrm{D}}$, $\tilde{\mathrm{B}}$ and the acoustic delay $\tilde{\Theta}$ related to the interior points, i.e. $\mathbf{x}_\star = \mathbf{x_i}$.

Coupling the exterior with the interior problem, i.e. system (3.100) with system (3.104), results in a $(N + \tilde{N}) \times N$ overdetermined linear system of equations which can be solved in a least square sense. Schenck also proved that the solution resulting from the exterior plus interior problems is theoretically unique for appropriately

chosen $\mathbf{x_i}$. The resulting linear system is

$$\mathrm{Y^C}\underline{\phi}^S = \mathrm{Z^C}\underline{\chi}^I, \tag{3.106}$$

for

$$\begin{aligned} \mathrm{Y^C} &= \begin{bmatrix} \frac{1}{2}\,\mathrm{I} - e^{-i\omega\,\Theta}\,(\mathrm{H}+\mathrm{C}+i\omega\mathrm{D}) \\ -e^{-i\omega\,\tilde{\Theta}}\left(\mathrm{H}+\tilde{\mathrm{C}}+i\omega\tilde{\mathrm{D}}\right) \end{bmatrix}, \\ \mathrm{Z^C} &= \begin{bmatrix} -e^{-i\omega\,\Theta}\mathrm{B} \\ -e^{-i\omega\,\tilde{\Theta}}\tilde{\mathrm{B}} \end{bmatrix}. \end{aligned} \tag{3.107}$$

Schenck proved that the resulting solution of the exterior plus interior problems is theoretically unique for appropriately chosen $\mathbf{x_i}$.

The CHIEF method is easy to implement, but its efficiency is strongly dependent on the choice of the interior collocation points $\mathbf{x_i}$. Unfortunately the only rule for choosing an optimal set of internal points $\mathbf{x_i}$ is that the points should not be placed at interior nodal coordinates, because the resulting equations at these nodes will not add an effective constraint to the system of equations. However, for a general geometry, these nodal coordinates are not known *a priori*. Furthermore, the problem becomes worse at high frequency, because more additional constraints are required. In this range, the solution is strongly affected by a more or less "efficient" interior point set. A method for creating an optimal set of interior collocation points remains a research topic for future high frequency applications of the BEM.

3.2.7 Numerical integration

In the no-flow case the integral coefficients and the acoustic delay can be computated analytically. In this case, the exact solution of the source and doublet surface integrals over the four-edge-panel and the explicit solution of the acoustic delay are available. However, this is not true in general, thus, a numerical integration of the coefficients (3.97) and an iterative numerical procedure to solve Eq. (3.78) is necessary to take into account the effect of a convecting swirling-translating mean flow.

For multidimensional integration the C package CUBA [86] was used. Specifically, the double integral over the four-edge-panel was calculated by means of the deter-

ministic algorithm Cuhre [87], which uses one of several cubature rules of polynomial degree in a globally adaptive subdivision scheme [87].

In order to calculate the acoustic delay, the Newton-Raphson method was applied. This is a root-finding algorithm that uses the first few terms of the Taylor series of the function in the neighborhood of a first-attempted root. The method converges very fast when the initial choice of the root's position is good enough. In this application the first choice used was the root of Eq. (3.78) obtained by expanding the rotation matrix $\mathbf{U}_\infty(\theta)$ up to the second order, i.e. $\mathbf{U}_\infty(\theta) = \mathbf{I} + \mathbf{\Omega}_\infty\theta + \mathbf{\Omega}_\infty^2\theta^2/2$, was used. The resulting equation is a second order polynomial in θ, which can be solved explicitly.

Another numerical issue arises to impose the boundary condition (3.35), for the analysis of the rotor acoustic source models. Following the analytical derivation of (3.23b), (3.23c), (3.24b), and (3.24c), the resulting integrals were evaluated through numerical integration. The one-dimensional integration over the rotor ring was performed through the standard FORTRAN package QUADPACK [88], while the double integral over the rotor disc was performed through the above mentioned Cuhre algorithm.

3.2.8 Parallel implementation

The analysis of the rotor source models propagating through the duct to the external field was carried out by varying the blade tip Mach number M_t and the azimuthal order m of the incident field. In the no-flow case, four tip Mach numbers $M_t = 0.8$, 1, 1.2, 1.4 and four orders $m = 4$, 8, 12, 16 were considered. These values were chosen to simulate a wide range of frequencies and flow cases in a transonic rotor regime. Defining the reference length a as the duct radius at the rotor disc, the two quantities m and M_t relate to the non-dimensional frequency ka through the equation $ka = mM_t$. Therefore, the scattered field was computed at a wide range of incident source frequencies, i.e. $3 < ka < 22$.

In the flow case, the analysis was carried out for $M_\infty = 0$, 0.2, 0.4, 0.6 and the non-dimensional $\Omega_\infty = 0$, 0.2, 0.4, 0.6, being the duct radius a the length scale and a/c the time scale. The rotor source analysis was, however, limited to $m = 4$, 8, 12, for some numerical instability occuring at high azimuthal orders. In terms of frequency,

only taking into account the compressibility factor due to the translating mean flow, $\sqrt{1-M_\infty^2}$, this translates into a frequency range equal to $3 < (ka)/\sqrt{1-M_\infty^2} < 21$, approximately the same as the no-flow case.

Convergence analysis has shown that at the highest frequency $ka = 22$ at least 8,000 panels must discretize the duct surface. In fact, this discretization assures that at least 4 panels per wave length cover the surface in order to capture correctly the wave at the highest frequency. Therefore, to solve the BEM linear system (3.100) a full 8,000 $\times$ 8,000 matrix must be computed, stored, and inverted. In order to overcome this difficulty, a parallel implementation of the method was developed in Fortran 90. The aim of using a parallel solver is to decrease both run time and allocated memory by dividing the calculation among parallel processors. Each processor is responsible for the calculation on some subset of the data. Every portion of array is directly defined and allocated as local to the single processor, which only works on this portion of the solution. Then, the global solution is recomposed using the appropriate library. Details of the implementation are reported in Appendix C, enclosing details on the specific software organization.

This parallel implementation was developed using the Scalable Linear Algebra PACKage (ScaLAPACK) [89] as parallel solver. ScaLAPACK is a library of linear algebra routines for distribuited-memory message-passing computers. It is a continuation of the LAPACK [90] project based on the Parallel Basic Linear Algebra Subprograms (PBLAS) [91] and the Basic Linear Algebra Communication Subprograms (BLACS) [92]. The former is the distributed memory version of the BLAS [93]. The latter is a collection of routines used to manage matrices for distribuited-memory message-passing computers, either based on Message Passing Interface MPI [94] or Parallel Virtual Machine PVM [95], implemented to provide a communication support for the ScaLAPACK library and to make linear algebra applications more portable.

Among the versions of the implemented BEM parallel code, two were compared to evaluate the parallel software performance: the first based on the BIE (3.30) for the no mean flow case; the second based on the BIE (3.79) for the swirling-translating mean flow case. The specific test case is not of interest, because the only difference on the results is due to the size of the problem. Figure (3.1) shows the performance per node of the two codes for the calculation of both the integral coefficients (Eq. (3.97) for the flow case) and the linear system (Eq. (3.100) for the flow case), considering a

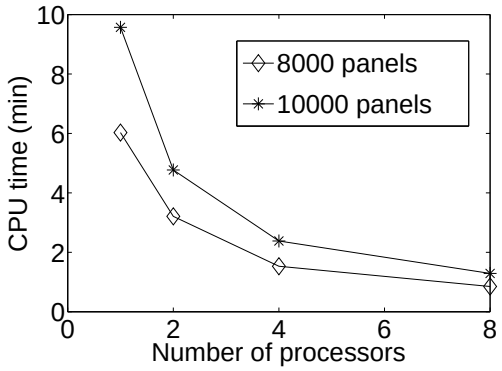

a) Time required to calculate the BEM integral coefficients. No-flow case.

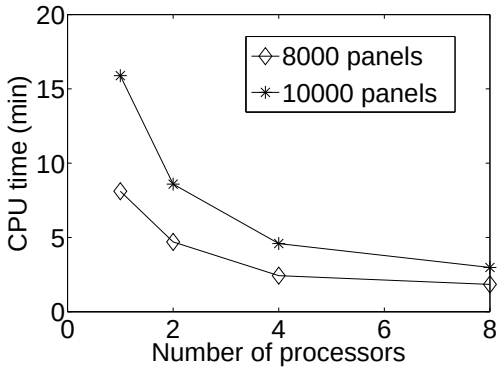

b) Time required to solve the BEM linear system. No-flow case.

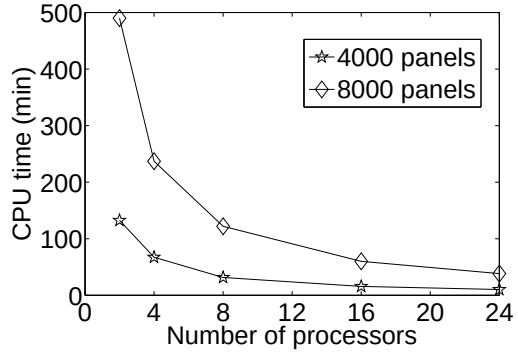

c) Time required to calculate the BEM integral coefficients. Swirling-translating flow case.

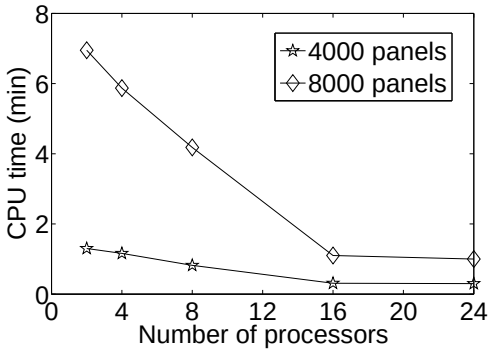

d) Time required to solve the BEM linear system. Swirling-translating flow case.

Figure 3.1: CPU time necessary for the two parallel BEM codes per computer node, increasing the number of processors.

couple of surface discretizations. An IBM eServer326m, dual-core, 2.2GHz computer cluster with 1Gb of RAM per core was used for the computations. For example, using 8 nodes, the computation of a 8,000 $\times$ 8,000 integral coefficient matrix requires approximately 2 hours, while the solver requires 4 minutes. The allocated memory per node is 64Mb. Increasing the number of processors, the computational time is highly reduced. Generally, doubling the number of processors corresponds to half the computational time, but the time for the solver is constant for more than 16 nodes, because this time is very low and the gain for using more processors is decreased by the loss in the communication among the nodes. From the CPU performance it can also be noted that the computation of the integral coefficients in the no flow case is highly less expensive than the flow case. This is mainly due to the numerical integration, required in the flow case, compared with the analytical integration, used for the no flow case. In fact, the two solver times are comparable and very low, while the time necessary to evaluate the integral coefficients is one hundred times higher. Furthermore, the size of the discretization has an important effect on the computational time. In the flow case, doubling the number of panels results in increasing the time for the integral coefficients of almost four times and the time for the solver of about five times.

Chapter 4

Analysis of the Spinning Rotor Source Models

In this chapter the analysis of the spinning rotor as acoustic source propagating through a duct to the external field is presented. The analysis is focused on the comparison between two different source models under the hypothesis of absence of mean flow, by applying the BEM formulation presented in Section 3.2.1. For the comparison, the disc and ring source models of the thrust and drag dipole components presented in Section 3.1.3 were employed. The aim is to verify if the disc model contains features which cannot be modelled through a ring model, as suggested by Carley [73], in terms of the far field directivity patterns.

4.1 Validation of the model: comparison with experiments

The parallel code based on the BEM formulation for scattering of a stationary body, i.e. BIE (3.34), was validated against experimental data for the pressure scattered by a cylinder of radius a in the far field [96]. The incident field was generated by an array of acoustic drivers placed inside the cylinder and selected in such a way that only one specific mode propagated in the duct. The pressure radiation patterns were measured by varying the frequency, the azimuthal order m and the distance at which the pressure was evaluated in the external acoustic field.

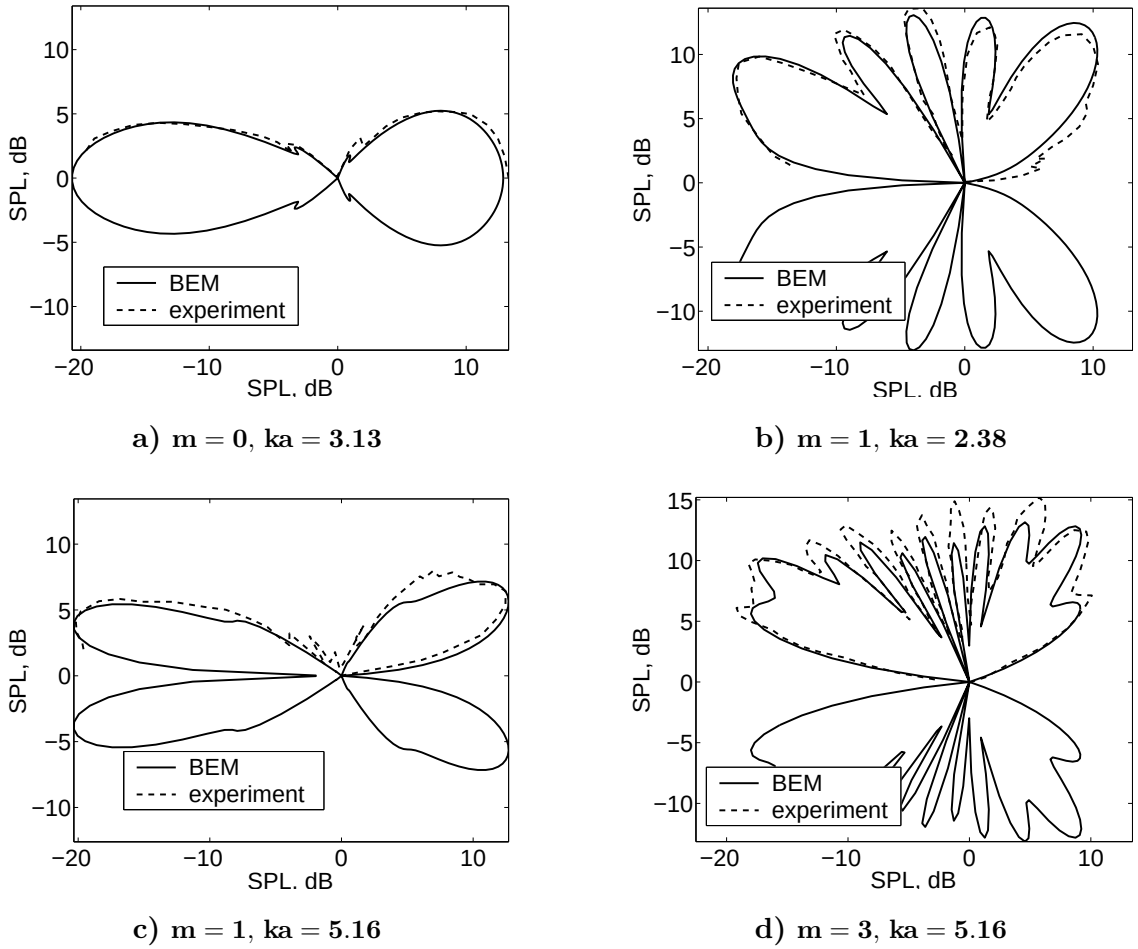

a) $\mathbf{m = 0}$, $\mathbf{ka = 3.13}$ **b)** $\mathbf{m = 1}$, $\mathbf{ka = 2.38}$

c) $\mathbf{m = 1}$, $\mathbf{ka = 5.16}$ **d)** $\mathbf{m = 3}$, $\mathbf{ka = 5.16}$

Figure 4.1: Directivity pattern for the sound pressure level (SPL) generated by the cylinder modes propagating in a stationary cylindrical duct to the far field.

Figure 4.1 compares the experimental and the numerical sound pressure level (SPL) radiation patterns. The SPL is reported in dB and scaled in such a way that the maximum level is 20 dB in each plot. Three spinning modes of azimuthal order $m = 0, 1, 3$ and radial order $n = 0$; three frequencies corresponding to $ka = 2.38, 3.13,$ and 5.16; and a distance for evaluating the pressure in the external field equal to $10a$ were chosen for the comparison. The BEM solution was found to be in agreement with the experimental data. Every mode is well predicted in both the number of lobes and their relative values. The major difference is for the highest frequency and order, where an average error of about 15% can be estimate on the experimental data.

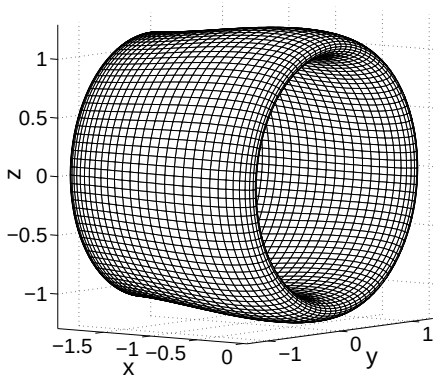

Figure 4.2: Discretized duct geometry.

4.2 Spinning rotor source model results

The BEM parallel code was applied to analyze the characteristics of the radiation patterns generated by two different rotor source models, (3.23b), (3.23c), (3.24b), and (3.24c), in conjunction with an axisymmetric duct geometry. Figure 4.2 shows a discretized version of the duct geometry, which was generated by the complete rotation of a Joukowsky profile. The rotor disc of radius b is placed at one quarter of the duct length, where the duct radius is equal to the reference length a, used as scale length. The duct maximum radius at the exhaust is equal to 1.125 and the duct length is 2. The frame of reference is centred at the duct inlet disc as shown in Fig. 4.2.

Table 4.1: Non-dimensional frequencies ka chosen for the computation.

m/M_t	**0.8**	**1.0**	**1.2**	**1.4**
4	3.2	4.0	4.8	5.6
8	6.4	8.0	9.6	11.2
12	9.6	12.0	14.4	16.8
16	12.8	16.0	19.2	22.4

As mentioned in Section 3.2.7, this analysis was carried out varying the blade tip Mach number M_t from 0.8 to 1.4 and the azimuthal order m from 4 to 16. The resulting non-dimensional frequencies $ka = M_t m$ are reported in Table 4.1.

The pressure values of the incident and scattered fields were evaluated over a circle of radius D. In order to compare the directivity patterns, the absolute pressure

Table 4.2: Maximum and minimum resonance ka at the minimum and maximum radii, respectively.

	a		**1.125a**	
m/n	**1**	**2**	**1**	**2**
4	5.32	9.28	4.73	8.25
8	9.65	14.12	8.57	12.55
12	13.88	18.75	12.34	16.66
16	18.06	23.26	16.06	20.68

Table 4.3: Number of cylinder cut-on modes at the rotor disc and exhaust.

	@ rotor disc				**@ exhaust**			
m/M_t	**0.8**	**1.0**	**1.2**	**1.4**	**0.8**	**1.0**	**1.2**	**1.4**
4	0	0	0	1	0	0	1	1
8	0	0	0	1	0	0	1	1
12	0	0	1	1	0	0	1	2
16	0	0	1	1	0	0	1	2

values were normalized with respect to their maximum. The maximum pressure values and the power levels were also plotted. The power level Π is a measure of the total power radiated from the duct. It is evaluated in dB as follows

$$\Pi = 10\log\left[\frac{\pi D^2/(\rho c)\int_0^{2\pi}|p_V|^2 \sin\alpha\, d\alpha}{P_{ref}}\right]. \tag{4.1}$$

Here $|p_V|$ is the absolute value of the pressure evaluated in the field, the integral is taken over a circle of radius D, and P_{ref} is the reference power, generally equal to $10^{-12} Watt$. Equation 4.1 is only valid for plane or spherical waves, however, in the far field the waves propagating from the duct can be approximated as spherical and this definition was used as a measure of the total power radiated from the duct.

Once the duct radius is given, it is possible to evaluate the resonance frequencies for a cylindrical duct as reported in Section 3.1.2 (Eq. 3.15). Since in the present case the radius is not constant, Table 4.2 reports the maximum and minimum resonance frequencies ka, corresponding to the minimum and maximum duct radius, respectively, for the given azimuthal orders m and the two first radial orders n.

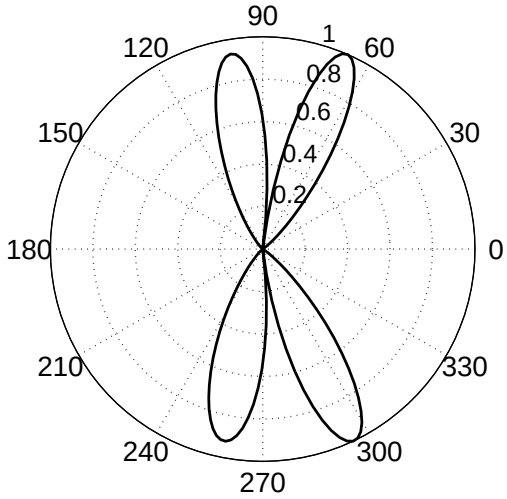

a) Incident field for $M_t = 1.0$, $m = 16$.

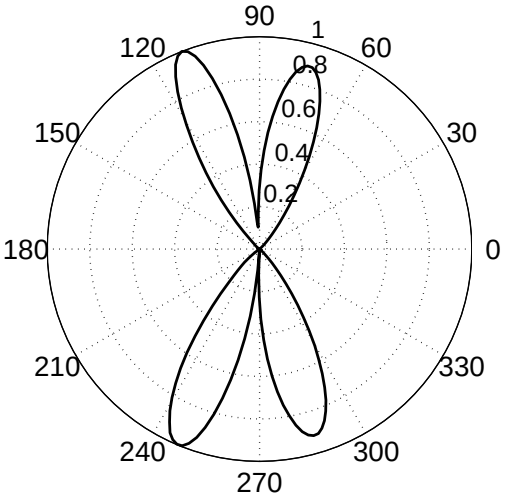

b) Scattered field for $M_t = 1.0$, $m = 16$.

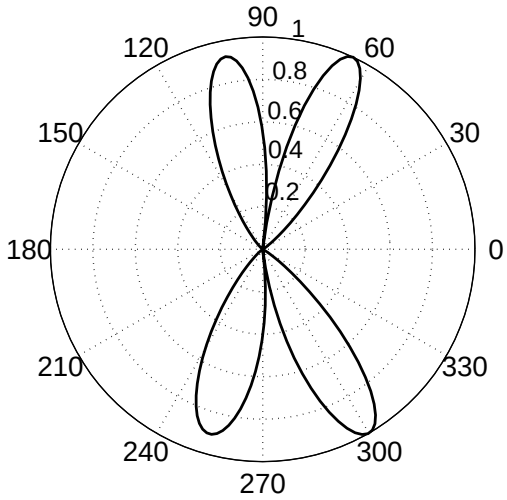

c) Incident field for $M_t = 1.2$, $m = 16$.

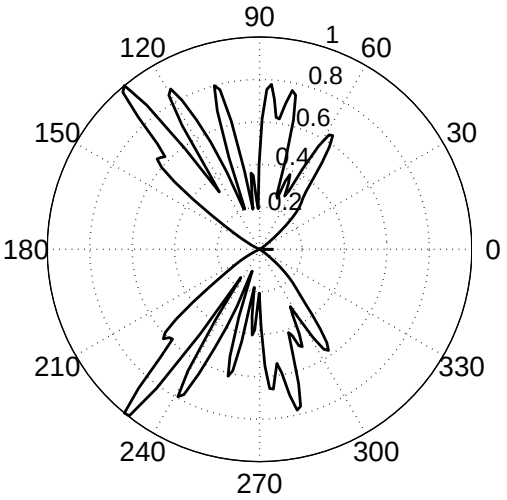

d) Scattered field for $M_t = 1.2$, $m = 16$.

Figure 4.3: Comparison of the incident and scattered fields for the directivity pattern of the normalized pressure for the thrust dipole source: ring model (upper side) and disc model (lower side).

Comparing the results of Table 4.2 and 4.1, it is shown that for $M_t = 0.8$ and $M_t = 1$ there are no cylinder cut-on modes. In fact, the frequency is lower than the first resonance frequency, whereas for $M_t = 1.2$ there is one cut-on mode (the frequency is higher than the first resonance frequency, but lower than the second) and for $M_t = 1.4$ two cut-on modes (the frequency is higher than the second resonance frequency). Table 4.3 summarizes the number of cylinder cut-on modes, depending on the two duct radii.

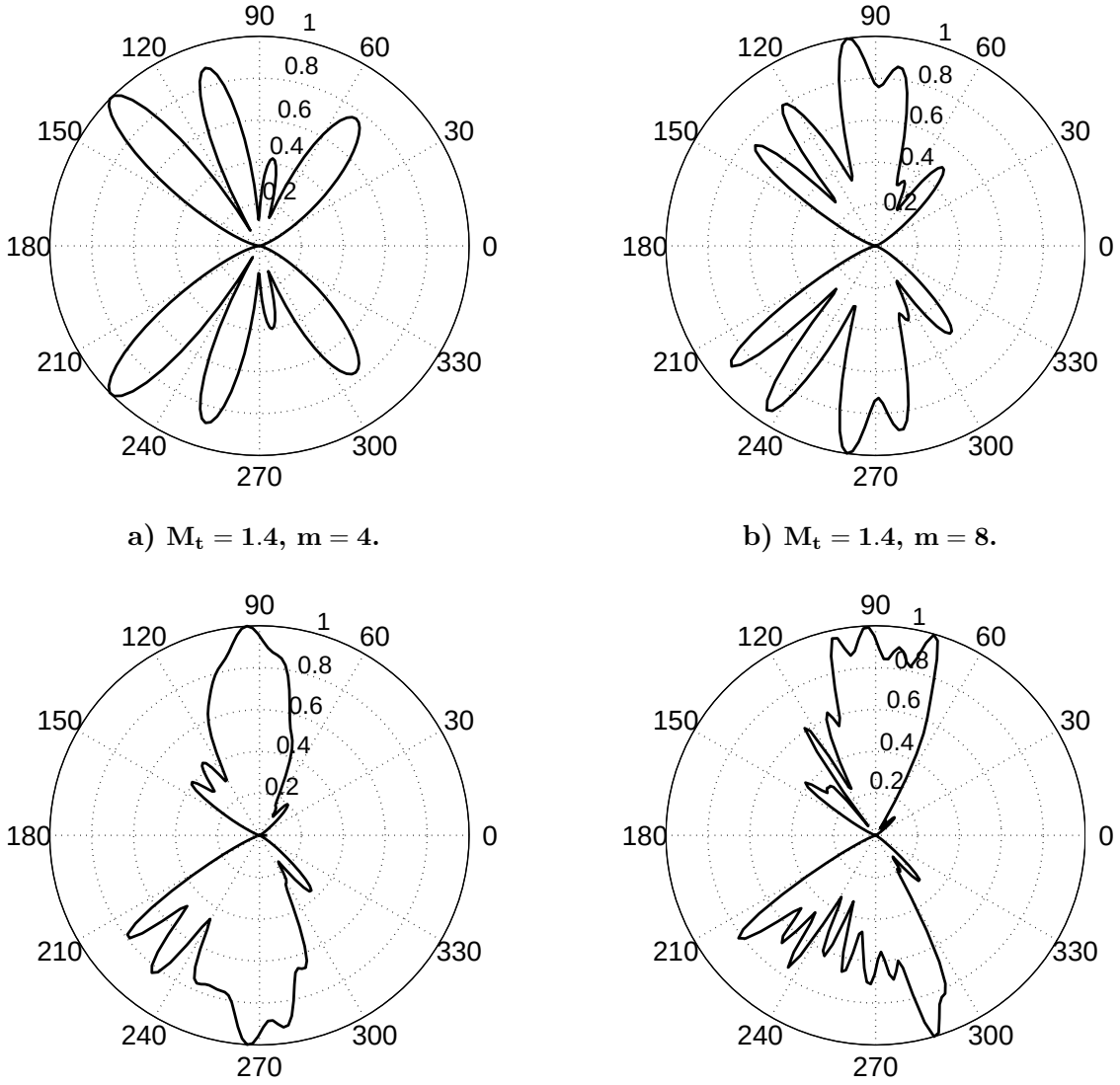

a) $\mathbf{M_t = 1.4,\ m = 4.}$ **b)** $\mathbf{M_t = 1.4,\ m = 8.}$

c) $\mathbf{M_t = 1.4,\ m = 12.}$ **d)** $\mathbf{M_t = 1.4,\ m = 16.}$

Figure 4.4: Comparison of the ring model (upper side) and the disc model (lower side) for the directivity pattern of the normalized scattered pressure for the drag dipole source (ring radius 0.75 and disc radius 1).

The modal propagation affects the directivity pattern of the scattered pressure and the overall power radiated from the duct. Figure 4.3 shows how the incident and scattered pressure directivity patterns at $D = 8$ differ, depending on the propagating modes. Note that the upper and lower sides of the plot refer to the ring and the disc model, respectively, If there are no cut-on modes, the scattered pressure pattern (Fig. 4.3(b)) is slightly different, as there is not actual sound excitation (Fig. 4.3(a)). However, if there is mode propagation, then the pattern is strongly modified; see comparison of Figs. 4.3(d) and 4.3(c).

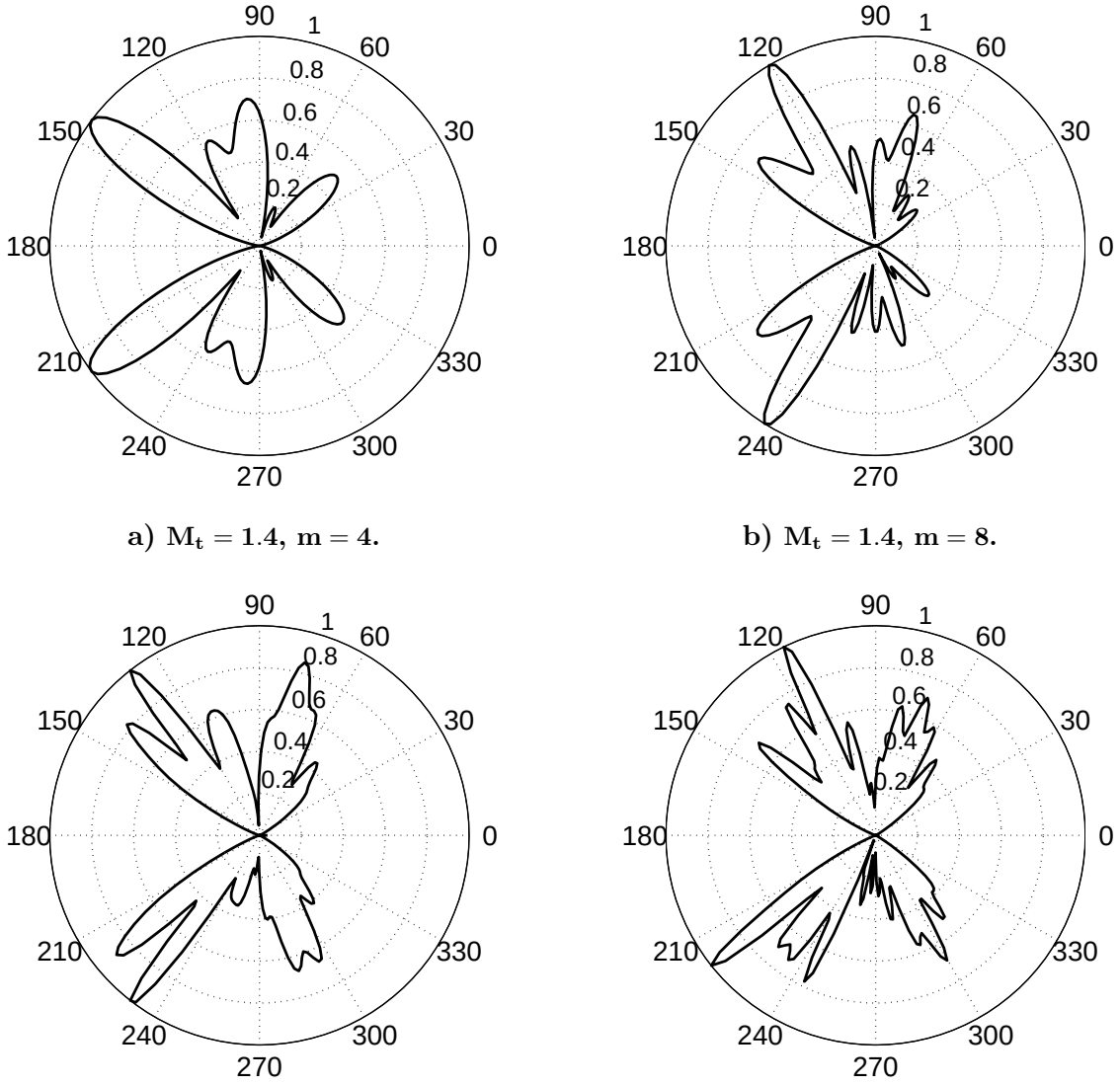

a) $\mathbf{M_t = 1.4,\ m = 4.}$ **b)** $\mathbf{M_t = 1.4,\ m = 8.}$

c) $\mathbf{M_t = 1.4,\ m = 12.}$ **d)** $\mathbf{M_t = 1.4,\ m = 16.}$

Figure 4.5: Comparison of the ring model (upper side) and the disc model (lower side) for the directivity pattern of the normalized scattered pressure for the thrust dipole source (ring radius 0.75 and disc radius 1).

Comparison of the ring and disc models for $M_t = 1.4$ and $D = 8$ is presented in Figs. 4.4 and 4.5. Assuming that the rotor disc covers the entire duct section, the disc radius used in the computations is 1 and the ring radius is 0.75 (three quarters of the blade chord). The differences between the patterns produced by the two models are remarkable, especially for $m = 12$, $m = 16$, and the drag dipole source. These differences could be due to the singularity occurring when the disc source approaches the duct boundary. This singularity arises when imposing the boundary condition at the duct panels intersecting the rotor disc. Here, the distance between the source

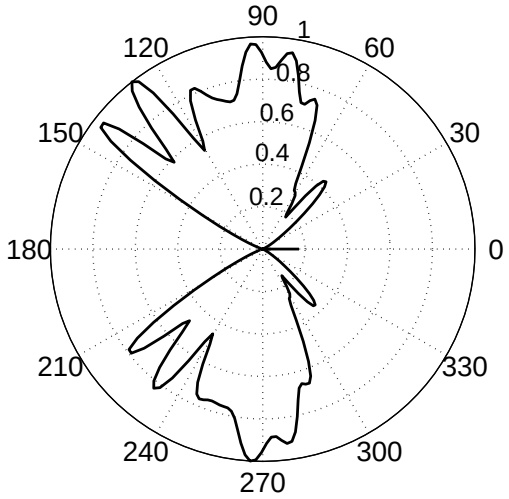

a) Drag dipole source for $M_t = 1.4$, $m = 12$.

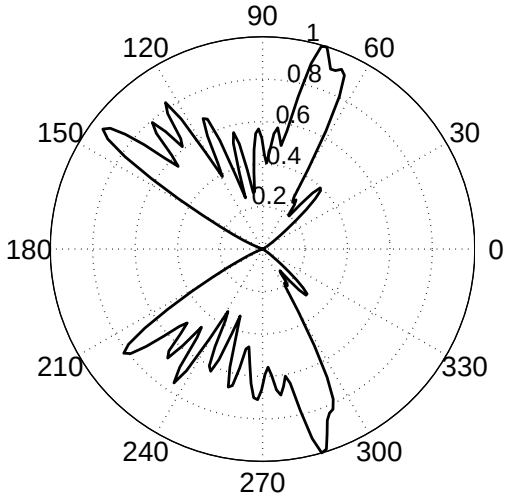

b) Drag dipole source for $M_t = 1.4$, $m = 16$.

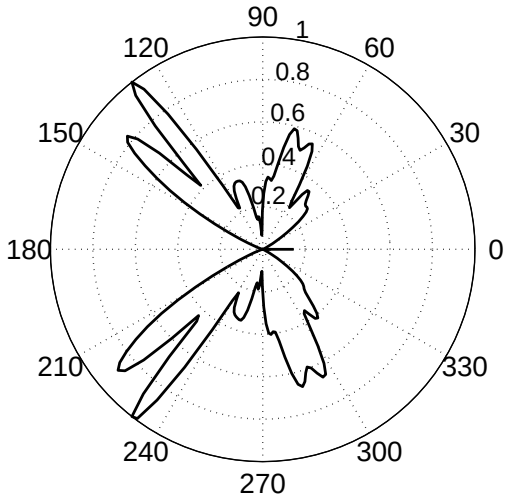

c) Thrust dipole source for $M_t = 1.4$, $m = 12$.

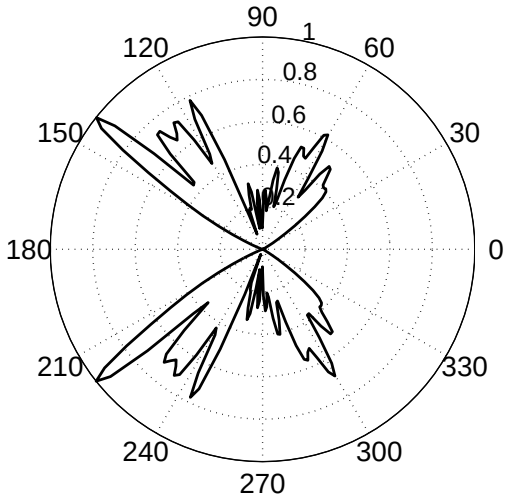

d) Thrust dipole source for $M_t = 1.4$, $m = 16$.

Figure 4.6: Comparison of the ring model (upper side) and the disc model (lower side) for the directivity pattern of the normalized scattered pressure (ring radius 0.9 and disc radius 1).

point and the panels tends to zero, so that the functions in the integrals (3.23b) and (3.23c), as well as in the corresponding normal derivatives, tend to infinity. Because a zeroth order method was employed, the collocation points were set up in the centre of each panel (centroids). By choosing the discretization carefully, it is possible to avoid positioning the centroids at the rotor disc boundary, thus avoiding the singularity. Therefore, the difference in the patterns depends on the ratio of the

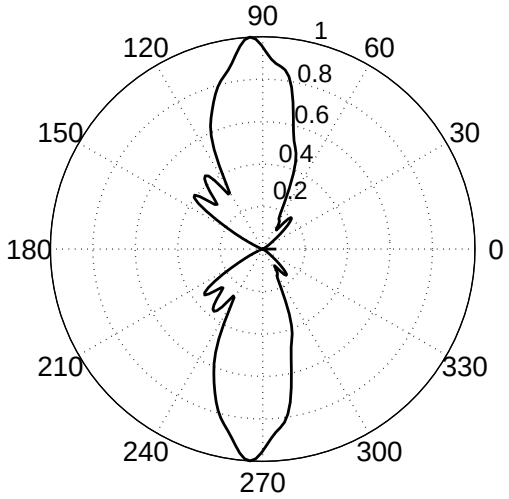

a) Drag dipole source for $M_t = 1.4$, $m = 12$.

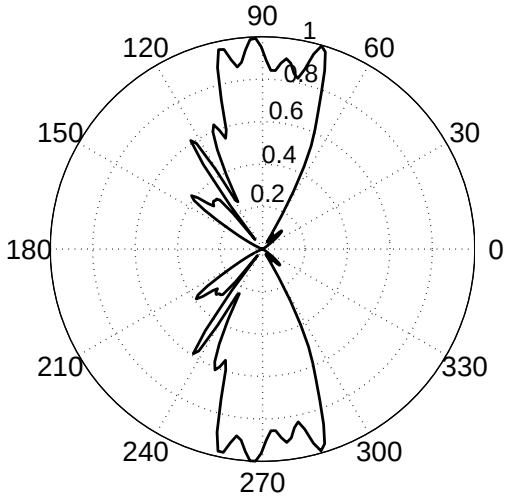

b) Drag dipole source for $M_t = 1.4$, $m = 16$.

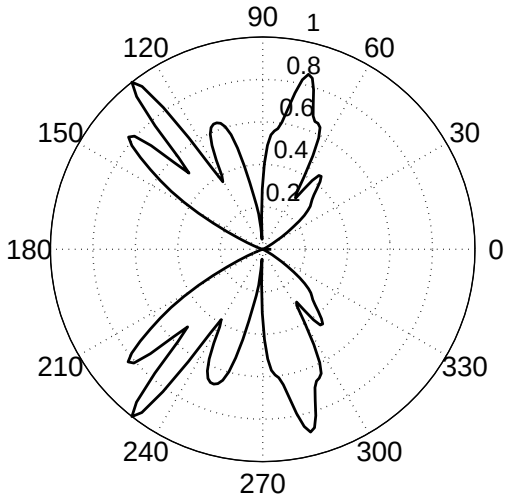

c) Thrust dipole source for $M_t = 1.4$, $m = 12$.

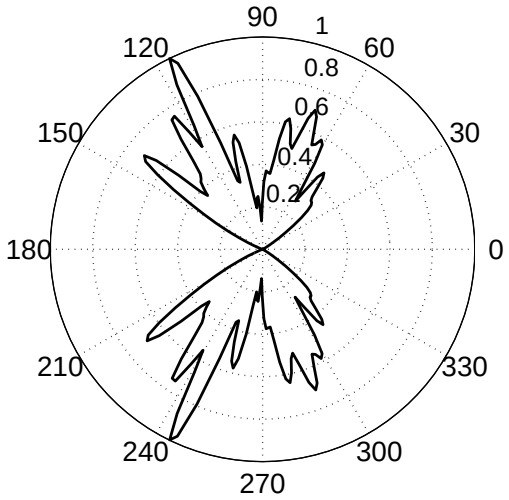

d) Thrust dipole source for $M_t = 1.4$, $m = 16$.

Figure 4.7: Comparison of the ring model (upper side) and the disc model (lower side) for the directivity pattern of the normalized scattered pressure (ring radius 0.75 and disc radius 0.8).

disc to ring radii. When increasing the ring radius to 0.9 (Fig. 4.6), the differences are highly reduced. This is also confirmed by Fig. 4.7, where the disc radius is reduced to 0.8 and the ring radius is 0.75. Therefore, from the scattered pressure directivity pattern point of view the two models are equivalent for a right choice of the radii, in spite of their different contents.

Figure 4.8 shows the variation of the scattered power levels between the two source

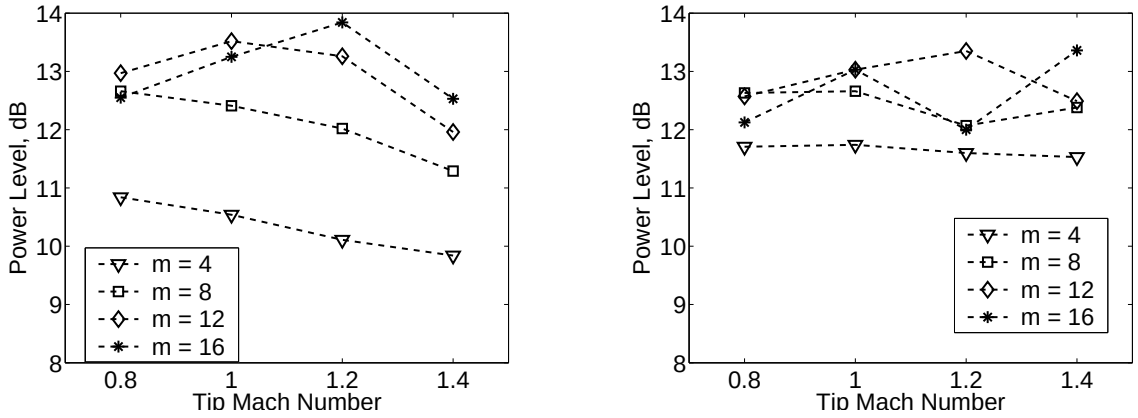

a) Drag dipole source. **b) Thrust dipole source.**

Figure 4.8: Variation of scattered power level between the ring and disc models for thrust and drag dipole sources.

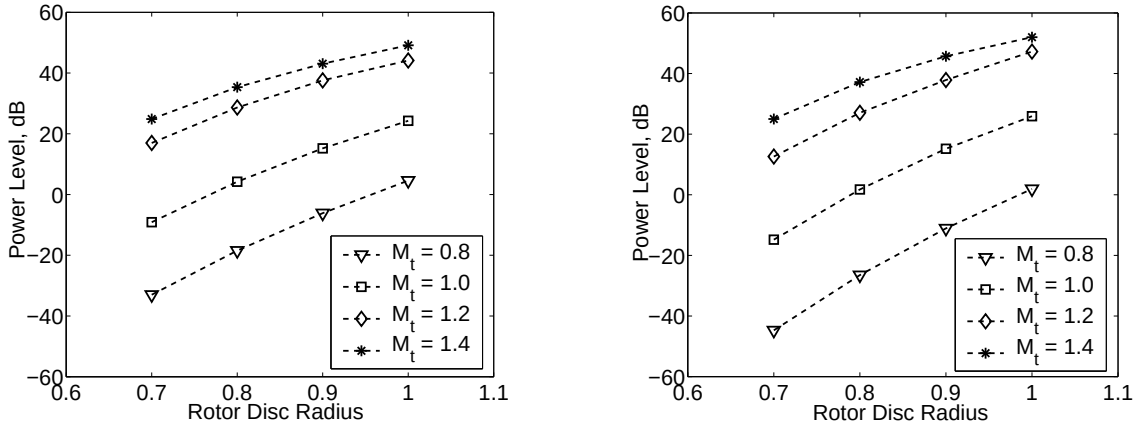

a) m = 12. **b) m = 16.**

Figure 4.9: Scattered power level as function of the rotor disc radius for the thrust dipole source and two different orders m.

models, $\Pi^S_{ring} - \Pi^S_{disc}$, as function of the tip Mach number M_t and the azimuthal order m. The results correspond to the case of disc radius 1 and ring radius 0.9. The ring source model predicts higher scattered power levels than the disc source model, on average between 10 and 14 dB. Generally, varying the tip Mach number and the azimuthal order has little effect on the variation of the scattered power level. The maximum difference of $\Pi^S_{ring} - \Pi^S_{disc}$ is less than 2 dB for the thrust dipole source and less than 4 dB for the drag dipole source. In particular, the main effect is due to the azimuthal order m. Fixing m, the maximum difference of $\Pi^S_{ring} - \Pi^S_{disc}$ is around 1 dB both for the thrust and the drag dipole source, having the minimum variation of the scattered power level for $m = 4$ and $m = 8$.

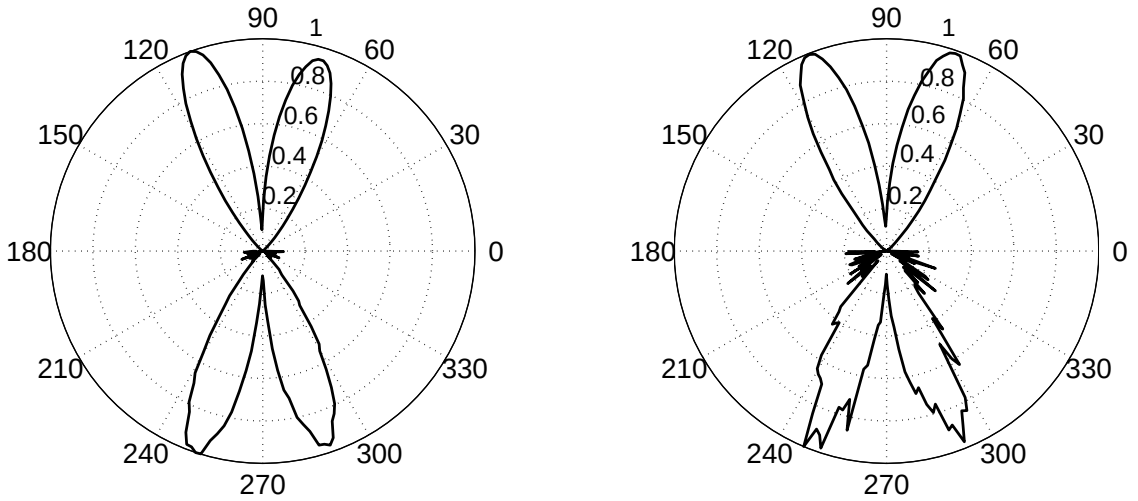

a) Ring model for $M_t = 1.0$, $m = 16$. **b) Disc model for $M_t = 1.0$, $m = 16$.**

Figure 4.10: Comparison of the ring and disc model varying the distance D for the directivity patterns of the normalized scattered pressure for the thrust dipole source: upper plot $D = 16$, lower plot $D = 64$.

In order to show the effect of the rotor disc radius on the radiated power, Fig. 4.9 reports the scattered power level versus the disc radius for a couple of orders m and the thrust dipole source as sample. In this specific case the levels are referred to $P_{ref} = 1$. The power decreases when a lower disc radius is used. This is consistent with the fact that when the disc radius decreases the source area decreases. The trend is not affected by the source model and the azimuthal order.

Another important parameter is the distance D at which the pressure is evaluated in the external acoustic field. In the above analysis, D was kept constant and equal to 8. Figure 4.10 shows a comparison of the ring and disc models in the very far field. Here, the upper and lower sides of the plot refer to the different distances. The ring model performs numerically better, because the pattern is slightly affected by the increased distance. Figure 4.11 shows the dependence of the directivity pattern on the distance D and the comparison between the two source models for $M_t = 1.4$ and $m = 12$. The agreement between the ring and disc source models is confirmed at different distances D. The pattern changes with D, but the global characteristics, i.e., the main lobes, remain the same, especially in the far field ($D > 4$). Furthermore, when varying D, the scattered power level does not change, thus energy is conserved in the model and this confirms that the expression of the power level (Eq. 4.1) is valid in the field of interest. On the other hand, the maximum scattered pressure decreases

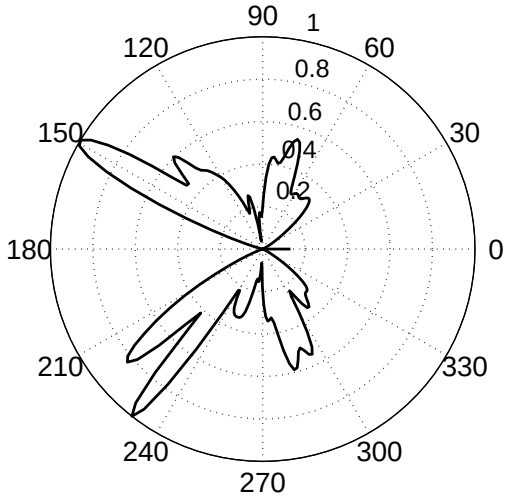

a) Ring model for $M_t = 1.4$, $m = 12$: upper plot $D = 4$, lower plot $D = 8$.

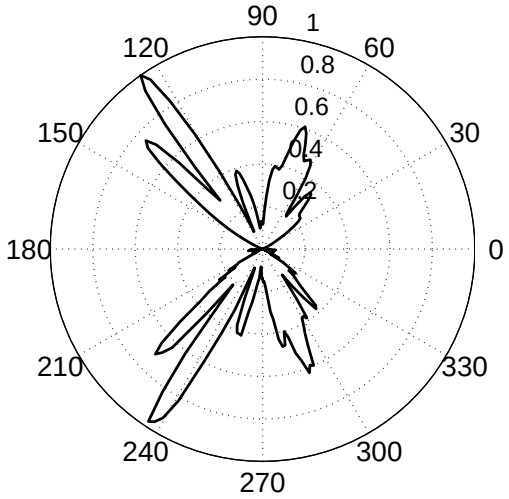

b) Ring model for $M_t = 1.4$, $m = 12$: upper plot $D = 16$, lower plot $D = 64$.

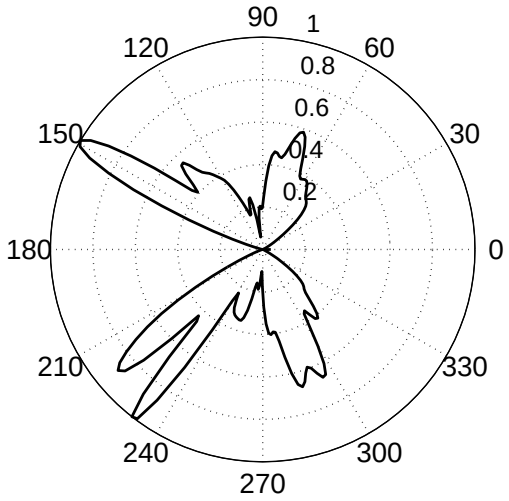

c) Disc model for $M_t = 1.4$, $m = 12$: upper plot $D = 4$, lower plot $D = 8$.

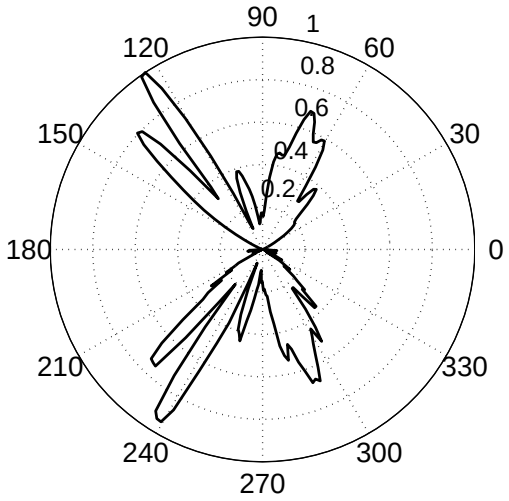

d) Disc model for $M_t = 1.4$, $m = 12$: upper plot $D = 16$, lower plot $D = 64$.

Figure 4.11: Comparison of the ring and disc model varying the distance D for the directivity patterns of the normalized scattered pressure for the thrust dipole source (ring radius 0.9 and disc radius 1).

linearly on a logarithmic scale (Fig. 4.12). This is a consequence of the fact that for constant power the product of the pressure and distance, D, has to be constant, so that half of the maximum pressure corresponds to a double distance.

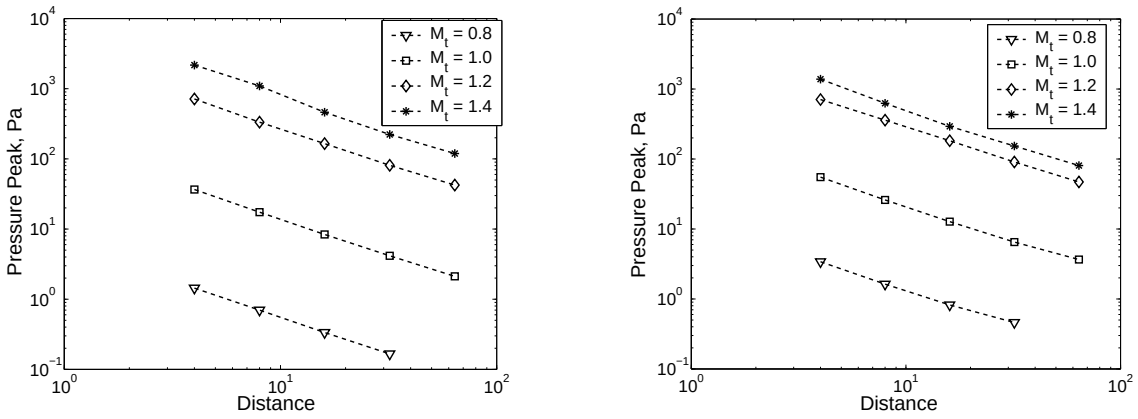

a) Ring model for m = 16. **b) Disc model for m = 16.**

Figure 4.12: Maximum scattered pressure versus distance D for the thrust dipole source.

Chapter 5

Effect of a Swirling-Translating Mean Flow. Far Field Propagation.

In this chapter the analysis of the spinning rotor source propagating through a duct is extended to take into account the effect of a swirling-translating mean flow. The BEM formulation and the source model presented in Section 3.2.3 is applied to investigate the effect of the mean flow on the far field propagation.

According to the results presented in the previous chapter, the pressure directivity patterns of the disc and ring source models are in total agreement for a ring to disc radius ratio equal to 0.9. Therefore, the analysis was limited to the ring source model, using a ring radius equal to 0.9. For simplicity, the only thrust dipole component, as presented in Section 3.2.4, was tested.

5.1 Model validation: comparison with the exact solution

The computational model was validated by means of the exact solution of a dipole point source

$$\phi = \frac{\partial}{\partial x_s}\left(\frac{e^{-i\omega\theta}}{4\pi\breve{\varrho}}\right), \tag{5.1}$$

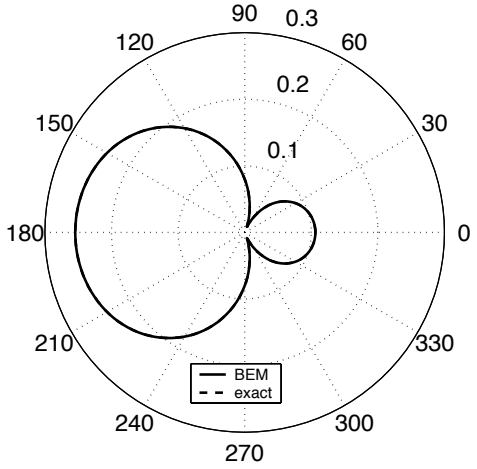

a) $\mathbf{M_\infty = 0.4}$, $\mathbf{\Omega_\infty = 0}$

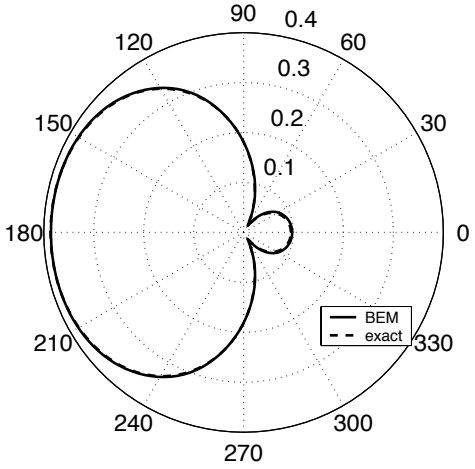

b) $\mathbf{M_\infty = 0.6}$, $\mathbf{\Omega_\infty = 0}$

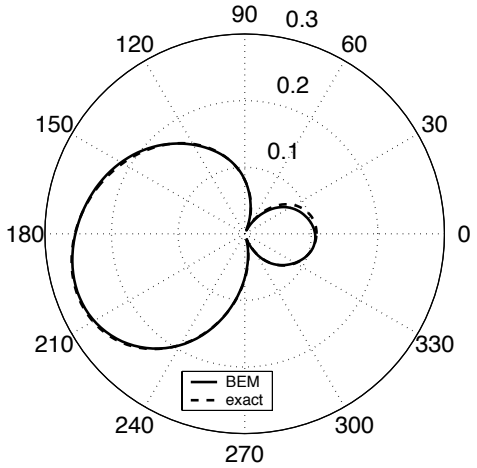

c) $\mathbf{M_\infty = 0.4}$, $\mathbf{\Omega_\infty = 0.4}$

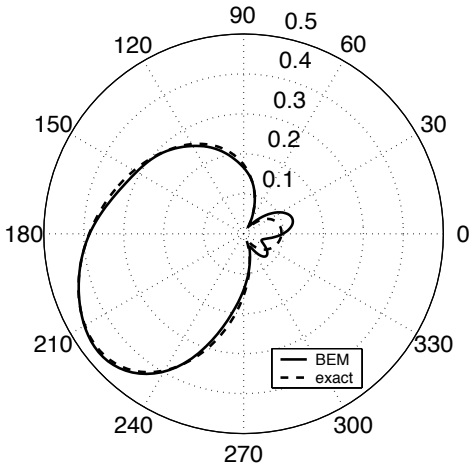

d) $\mathbf{M_\infty = 0.6}$, $\mathbf{\Omega_\infty = 0.4}$

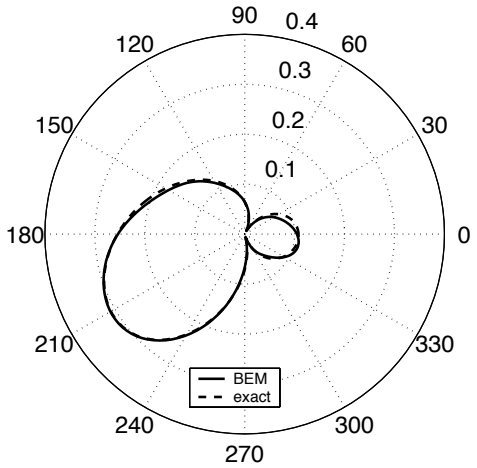

e) $\mathbf{M_\infty = 0.4}$, $\mathbf{\Omega_\infty = 0.6}$

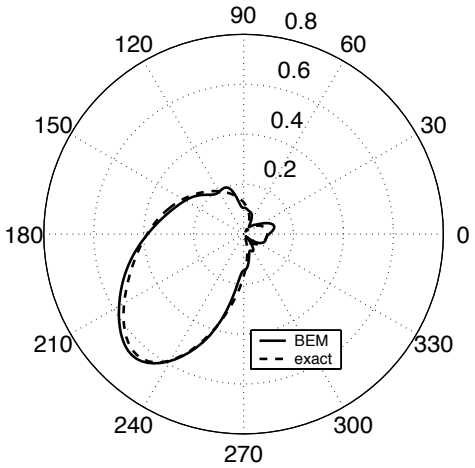

f) $\mathbf{M_\infty = 0.6}$, $\mathbf{\Omega_\infty = 0.6}$

Figure 5.1: Comparison of the directivity patterns of the velocity potential generated by a dipole ($ka = 4$) and the BEM solution scattered from a cylinder.

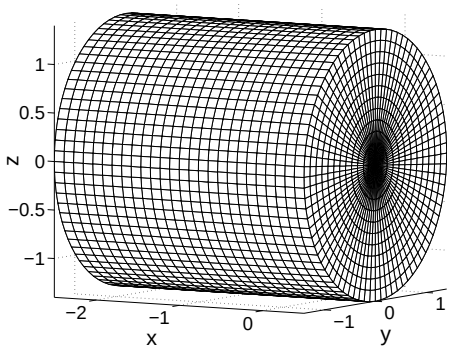

Figure 5.2: Discretized cylinder geometry surrounding the duct.

where quantities are defined as in Eq. (3.89)). The velocity potential due to the dipole was compared with the BEM velocity potential scattered from a cylinder with the same dipole providing the boundary condition for the incident field. The cylinder axis was placed in the x-direction and its center at the coordinate center. The cylinder radius a was used as the reference length; the length of the cylinder was 2. The dipole, directed along the x axis, was placed on the z axis at a distance 0.5 from the origin of the coordinates. The directivity patterns were evaluated on a circle of radius 2 on the xy plane.

Figure (5.1) shows the comparison for a dipole source oscillating at the non-dimensional frequency $ka = 4$. The case concerns with the superposition of a flow translating along the x axis and a swirling flow rotating around the same axis. The swirling mean flow angular velocity Ω_∞ was normalized using a/c as the time scale. The Ω_∞ values are 0, 0.4, 0.6. The exact and computed velocity potentials agree very well, especially for $M_\infty = 0.4$, while for $M_\infty = 0.6$ some distorsion can be noted in the directivity pattern. The latter is probably due to the effect of the approximation of the surface gradient integral coefficient, described in Appendix A, which is more effective for high Mach numbers.

5.2 Spinning rotor source results in the far field

The computational model was used to investigate the characteristics of the far field radiation patterns generated by the rotor ring incident field (Eq. (3.91b)) and convected by a swirling-translating mean flow.

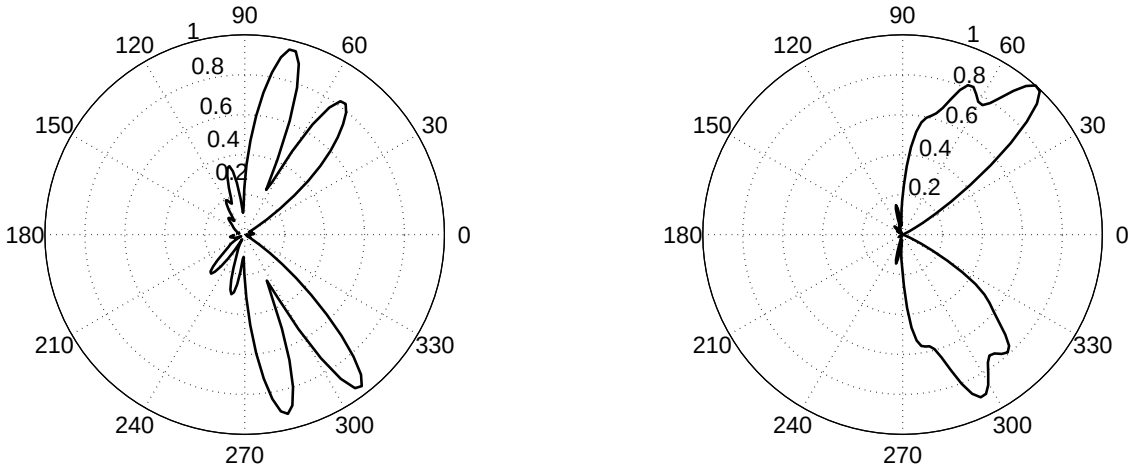

a) $\mathbf{M_t = 1.0}$, $\mathbf{m = 12}$ **b)** $\mathbf{M_t = 1.4}$, $\mathbf{m = 12}$

Figure 5.3: Effect of the length of the fictitious cylinder, shorter (upper side) and longer (lower side), for the directivity pattern of the normalized scattered pressure. $M_\infty = 0.4$, $\Omega_\infty = 0.4$

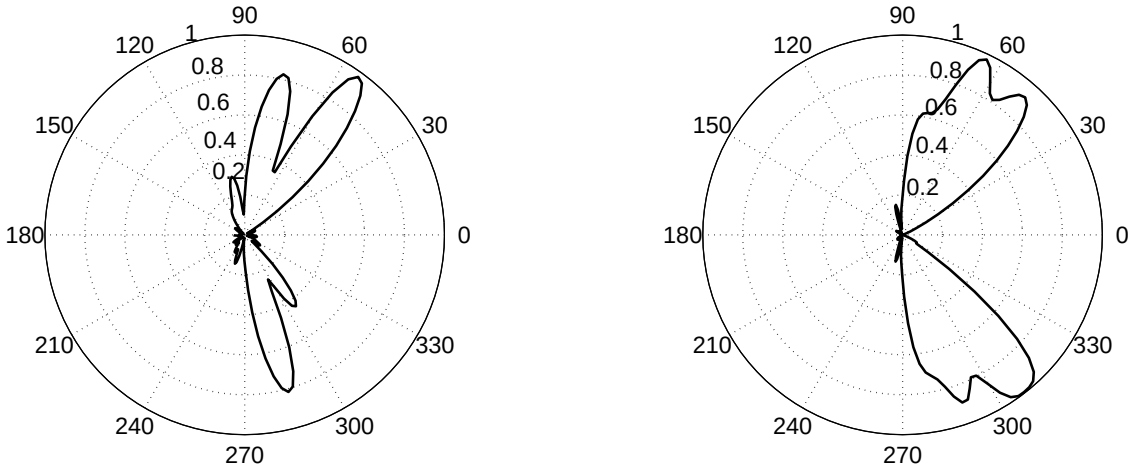

a) $\mathbf{M_t = 1.0}$, $\mathbf{m = 12}$ **b)** $\mathbf{M_t = 1.4}$, $\mathbf{m = 12}$

Figure 5.4: Effect of the width of the fictitious cylinder, reference (upper side) and wider (lower side), for the directivity pattern of the normalized scattered pressure. $M_\infty = 0.4$, $\Omega_\infty = 0.4$.

The duct geometry is the same used in the previous chapter (Fig. 4.2). In order to simulate a stationary nacelle embedded in still air with a mean flow passing through, the directivity pattern in the far field for a stationary observer was obtained as follows: (i) for the duct in a swirling-translating mean flow, the BIE (3.79) was used to calculate the scattered velocity potential on a fictitious cylinder surrounding the duct; (ii) then, for the propagation outside the duct, the BIR formulation in the

absence of flow was used to calculate the scattered pressure propagating from the fictitious cylinder to the far field.

A discretized version of the fictitious cylinder geometry is shown in Fig. 5.2. The dimensions were chosen so that the cylinder surface was very close to the duct surface, especially to the external lateral boundary of the duct: radius and length equal to 1.4 and 3, respectively. Figures 5.3 and 5.4 present the directivity pattern of the normalized scattered pressure evaluated over a circle of radius $D = 8$, varying the cylinder dimensions at $M_\infty = 0.4$ and $\Omega_\infty = 0.4$, for a couple of source frequencies. They show that a variation of the cylinder lenght, 0.5 longer and 0.3 shorter, does not significantly affect the far field solution, and a variation of the cylinder radius, 0.4 larger, slightly affects the solution. This confirms that the solution is not sensitive to the fictitious cylinder dimensions, therefore the results obtained using the chosen reference dimensions can lead to general conclusions.

The investigation was carried out for different spinning source blade tip Mach numbers M_t and azimuthal orders m, according to the study on the comparison between the rotor source models reported in the previous chapter. However, the order m was limited to 12, to avoid some numerical instability occurring at the highest m value. Furthermore, a negative value of m was also considered in order to investigate the effect of the opposite rotation of the spinning source. Refer to Table 4.1 for the M_t and m ranges and the corresponding non-dimensional frequencies ka. The Mach number M_∞ (opposite to the x-direction) and the rotation velocity Ω_∞ of the mean flow were chosen as $M_\infty = 0$, 0.2, 0.4, 0.6 and $\Omega_\infty = 0$, 0.2, 0.4, 0.6.

5.2.1 Translating mean flow effect: varying the Mach number

In order to show the translating flow effect, the directivity pattern of the normalized scattered pressure and the scattered power levels, evaluated at the distance $D = 8$, were plotted by varying M_∞ and keeping Ω_∞ constant. Figures 5.5, 5.6, 5.7, 5.8 show the directivity patterns for the azimuthal orders $m = 4$ and 12 and the angular velocities $\Omega_\infty = 0$ and 0.4. The upper and lower sides of the directivity patterns refer to the different Mach numbers, $M_\infty = 0, 0.2, 0.4, 0.6$. Figure 5.9 shows the variation of the scattered power level versus the translating flow Mach number, fixing the tip Mach number M_t and the order m. The difference of the levels were evaluated with

respect to the case where there is no mean flow.

The effect of the mean flow is clearly remarkable. As predicted by the modal analysis (Section 3.1.2), the modal content increases when the flow Mach number increases. In fact, the directivity pattern gets richer in peaks, i.e. more lobes corresponds to more cut-on modes [13], and the scattered power level increases. Furthermore, the main lobes of the directivity patterns tend to move downstream.

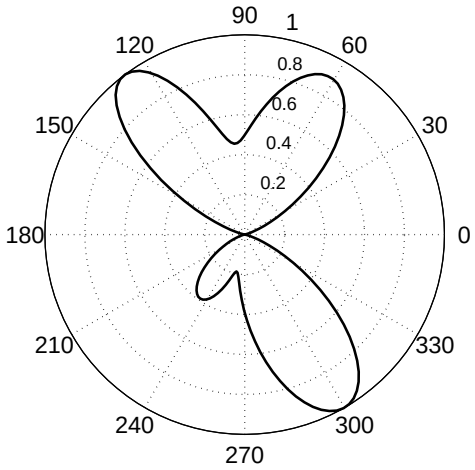

a) $\mathbf{M_t = 1.0}$, $\mathbf{M_\infty = 0}$ **(upper side),** $\mathbf{M_\infty = 0.2}$ **(lower side)**

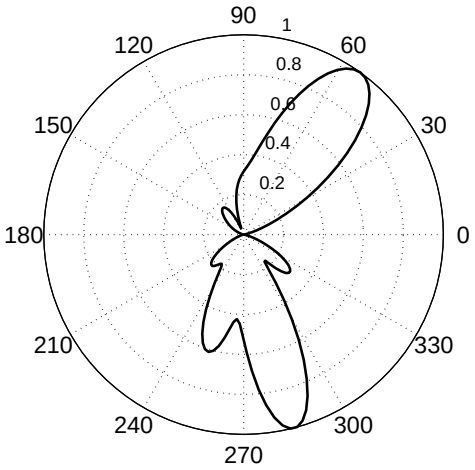

b) $\mathbf{M_t = 1.0}$, $\mathbf{M_\infty = 0.4}$ **(upper side),** $\mathbf{M_\infty = 0.6}$ **(lower side)**

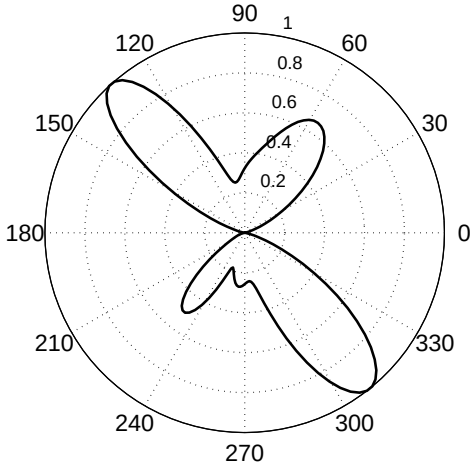

c) $\mathbf{M_t = 1.2}$, $\mathbf{M_\infty = 0}$ **(upper side),** $\mathbf{M_\infty = 0.2}$ **(lower side)**

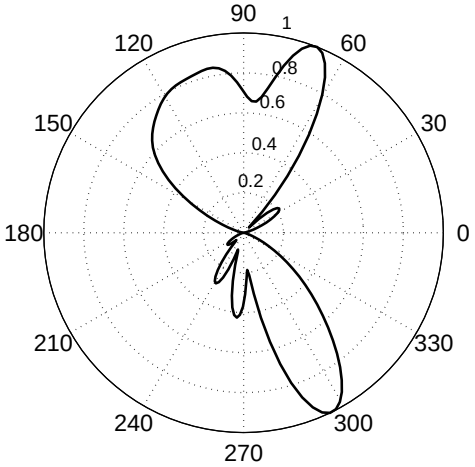

d) $\mathbf{M_t = 1.2}$, $\mathbf{M_\infty = 0.4}$ **(upper side),** $\mathbf{M_\infty = 0.6}$ **(lower side)**

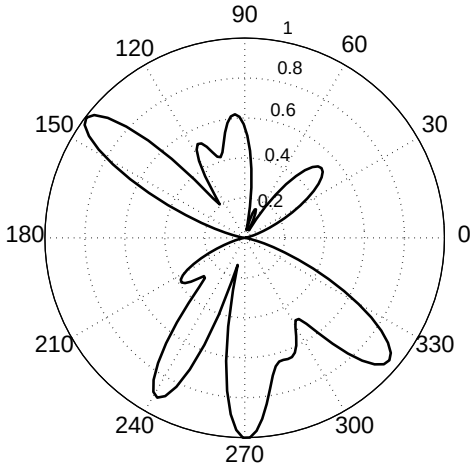

e) $\mathbf{M_t = 1.4}$, $\mathbf{M_\infty = 0}$ **(upper side),** $\mathbf{M_\infty = 0.2}$ **(lower side)**

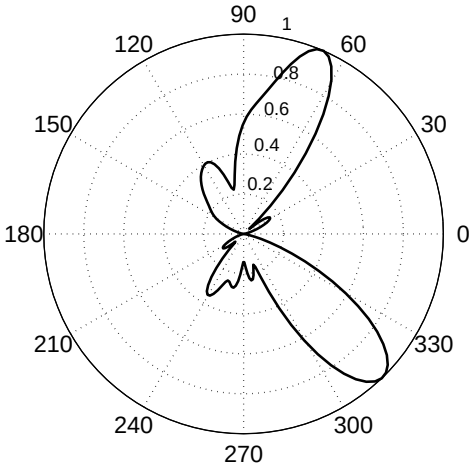

f) $\mathbf{M_t = 1.4, M_\infty = 0.4}$ **(upper side),** $\mathbf{M_\infty = 0.6}$ **(lower side)**

Figure 5.5: Directivity pattern of the normalized scattered pressure for varying M_∞; $m = 4$, $\Omega_\infty = 0$.

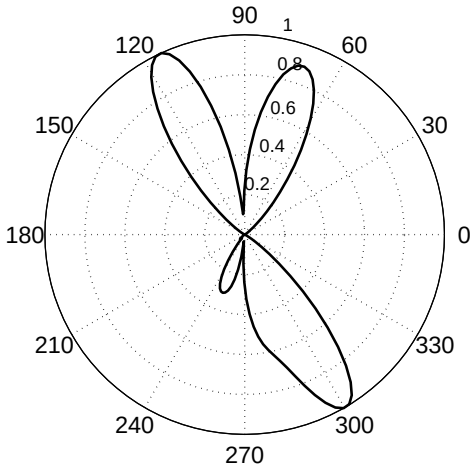

a) $\mathbf{M_t = 1.0}$, $\mathbf{M_\infty = 0}$ **(upper side),** $\mathbf{M_\infty = 0.2}$ **(lower side)**

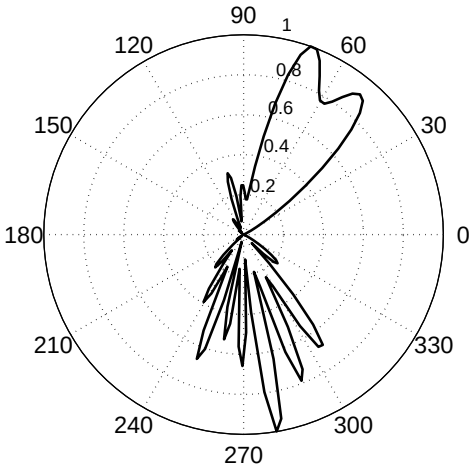

b) $\mathbf{M_t = 1.0}$, $\mathbf{M_\infty = 0.4}$ **(upper side),** $\mathbf{M_\infty = 0.6}$ **(lower side)**

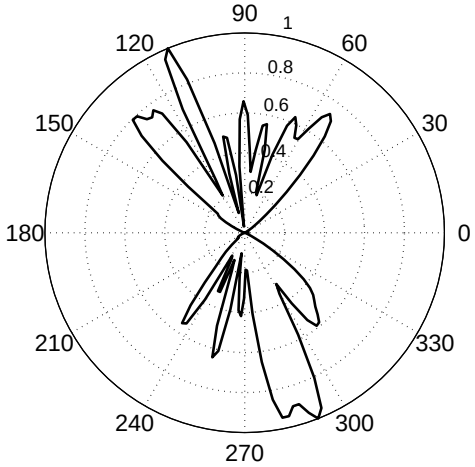

c) $\mathbf{M_t = 1.2}$, $\mathbf{M_\infty = 0}$ **(upper side),** $\mathbf{M_\infty = 0.2}$ **(lower side)**

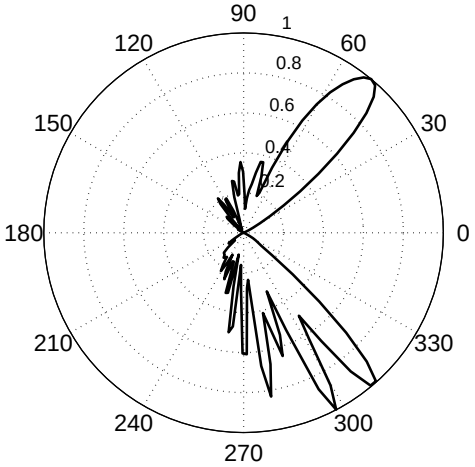

d) $\mathbf{M_t = 1.2}$, $\mathbf{M_\infty = 0.4}$ **(upper side),** $\mathbf{M_\infty = 0.6}$ **(lower side)**

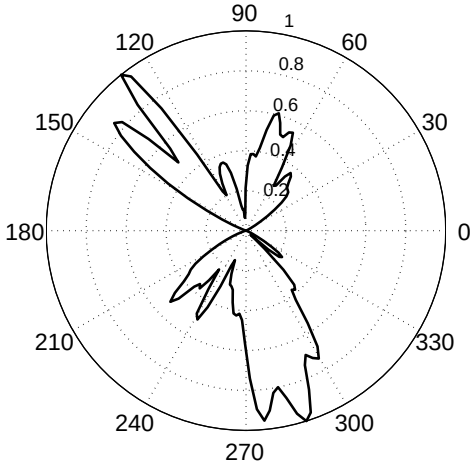

e) $\mathbf{M_t = 1.4}$, $\mathbf{M_\infty = 0}$ **(upper side),** $\mathbf{M_\infty = 0.2}$ **(lower side)**

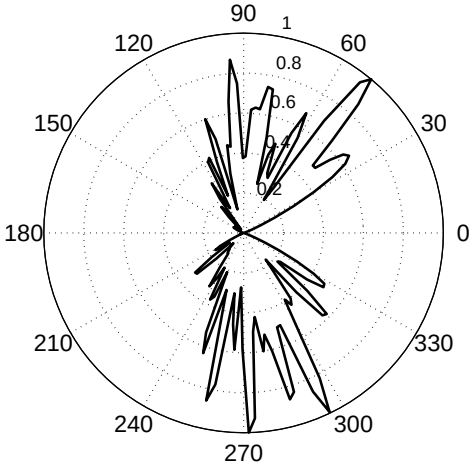

f) $\mathbf{M_t = 1.4, M_\infty = 0.4}$ **(upper side),** $\mathbf{M_\infty = 0.6}$ **(lower side)**

Figure 5.6: Directivity pattern of the normalized scattered pressure for varying M_∞; $m = 12$, $\Omega_\infty = 0$.

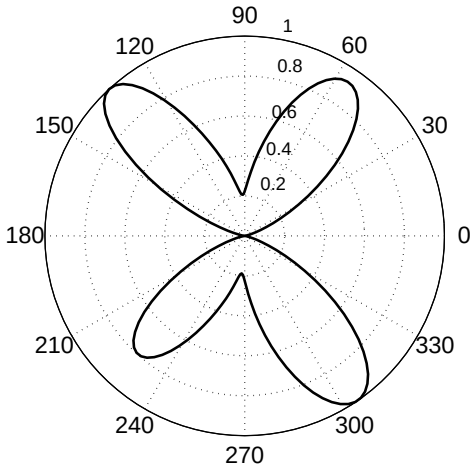

a) $\mathbf{M_t = 1.0}$, $\mathbf{M_\infty = 0}$ **(upper side),** $\mathbf{M_\infty = 0.2}$ **(lower side)**

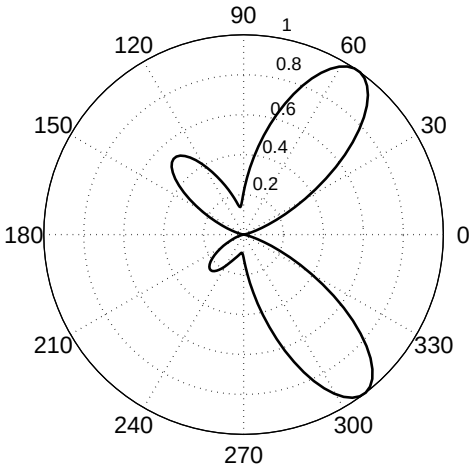

b) $\mathbf{M_t = 1.0}$, $\mathbf{M_\infty = 0.4}$ **(upper side),** $\mathbf{M_\infty = 0.6}$ **(lower side)**

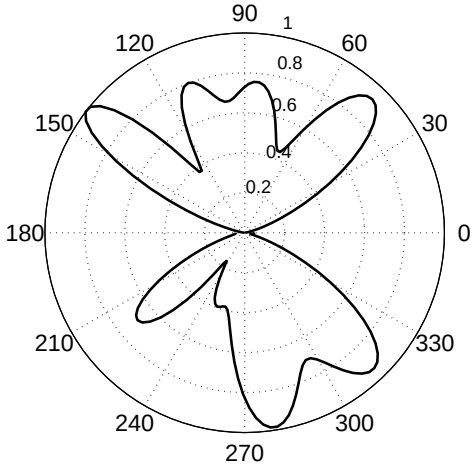

c) $\mathbf{M_t = 1.2}$, $\mathbf{M_\infty = 0}$ **(upper side),** $\mathbf{M_\infty = 0.2}$ **(lower side)**

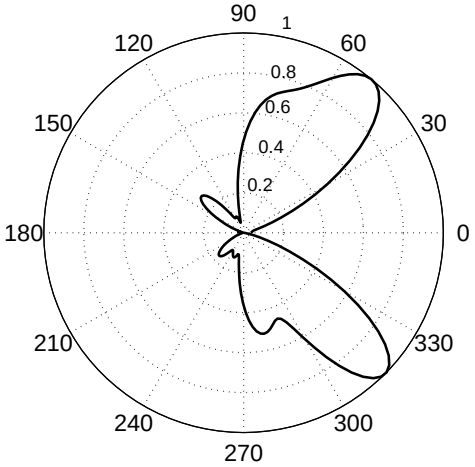

d) $\mathbf{M_t = 1.2}$, $\mathbf{M_\infty = 0.4}$ **(upper side),** $\mathbf{M_\infty = 0.6}$ **(lower side)**

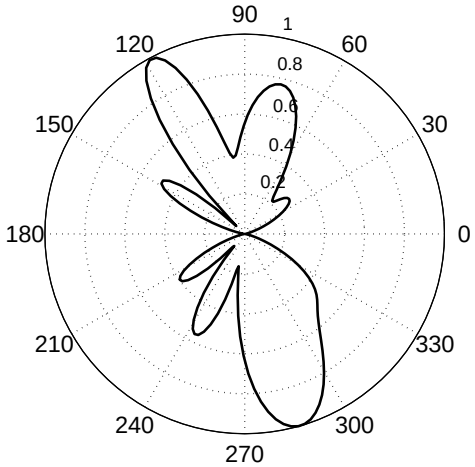

e) $\mathbf{M_t = 1.4}$, $\mathbf{M_\infty = 0}$ **(upper side),** $\mathbf{M_\infty = 0.2}$ **(lower side)**

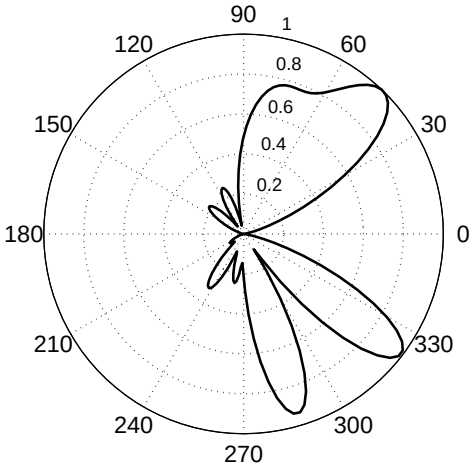

f) $\mathbf{M_t = 1.4, M_\infty = 0.4}$ **(upper side),** $\mathbf{M_\infty = 0.6}$ **(lower side)**

Figure 5.7: Directivity pattern of the normalized scattered pressure for varying M_∞. $m = 4$, $\Omega_\infty = 0.4$.

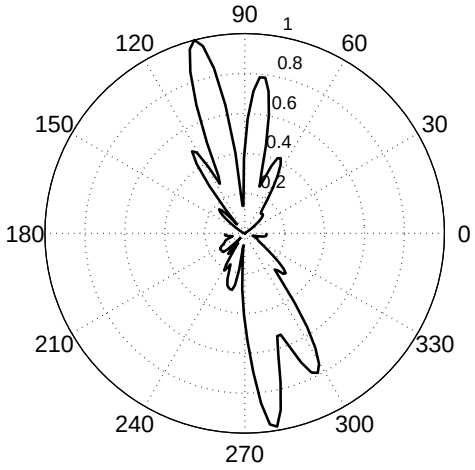

a) $\mathbf{M_t = 1.2}$, $\mathbf{M_\infty = 0}$ **(upper side),** $\mathbf{M_\infty = 0.2}$ **(lower side)**

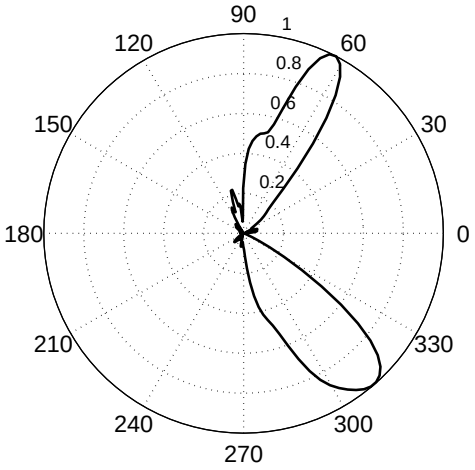

b) $\mathbf{M_t = 1.2}$, $\mathbf{M_\infty = 0.4}$ **(upper side),** $\mathbf{M_\infty = 0.6}$ **(lower side)**

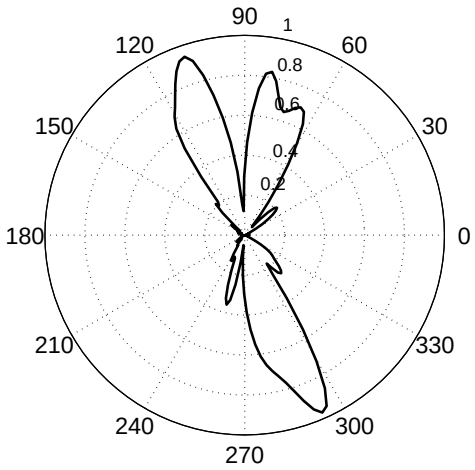

c) $\mathbf{M_t = 1.4}$, $\mathbf{M_\infty = 0}$ **(upper side),** $\mathbf{M_\infty = 0.2}$ **(lower side)**

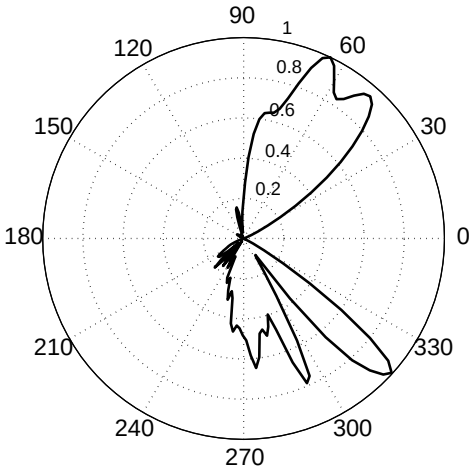

d) $\mathbf{M_t = 1.4}$, $\mathbf{M_\infty = 0.4}$ **(upper side),** $\mathbf{M_\infty = 0.6}$ **(lower side)**

Figure 5.8: Directivity pattern of the normalized scattered pressure for varying M_∞; $m = 12$, $\Omega_\infty = 0.4$.

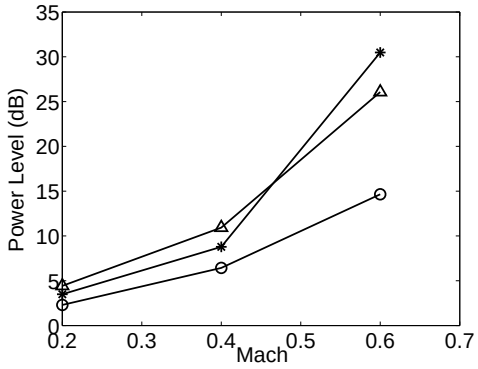

a) $\mathbf{M_t = 1.0}$, $\mathbf{\Omega_\infty = 0}$

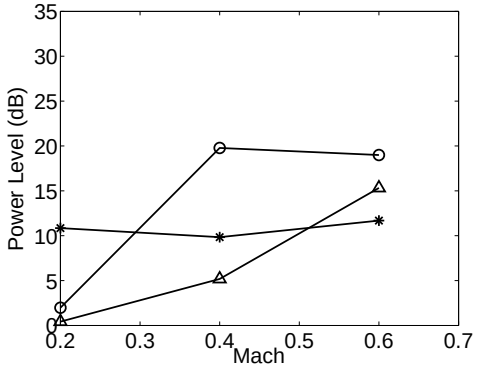

b) $\mathbf{M_t = 1.2}$, $\mathbf{\Omega_\infty = 0}$

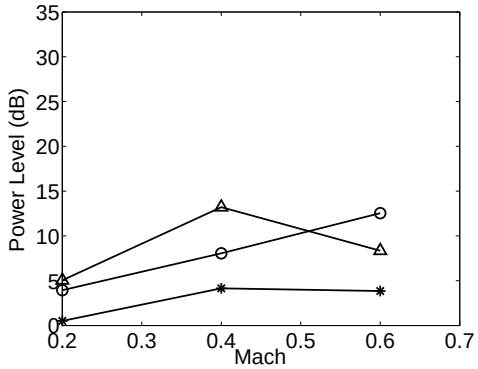

c) $\mathbf{M_t = 1.4}$, $\mathbf{\Omega_\infty = 0}$

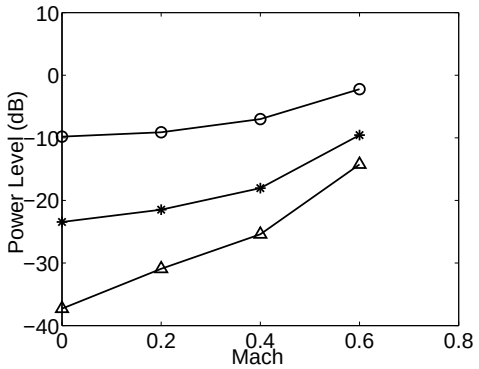

d) $\mathbf{M_t = 1.0}$, $\mathbf{\Omega_\infty = 0.4}$

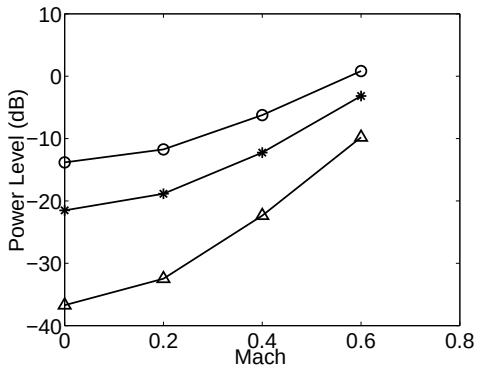

e) $\mathbf{M_t = 1.2}$, $\mathbf{\Omega_\infty = 0.4}$

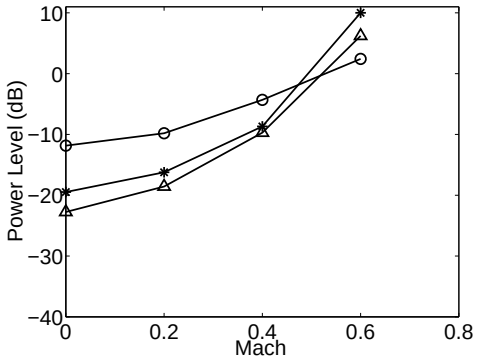

f) $\mathbf{M_t = 1.4}$, $\mathbf{\Omega_\infty = 0.4}$

Figure 5.9: Variation of the scattered power level versus M_∞, for constant m: lines $-\circ-$ $m = 4$, $-*-$ $m = 8$, $-\triangle-$ $m = 12$. The difference is calculated with respect to the case where there is no mean flow.

5.2.2 Swirling mean flow effect: varying the angular velocity

The swirling flow effect was investigated using the directivity pattern of the normalized scattered pressure and the scattered power levels; Ω_∞ was varied for constant M_∞. Figures 5.10, 5.11, 5.12, 5.13, 5.14 show the directivity patterns for the azimuthal orders $m = 4$, 8 and -8 and translating flow Mach numbers $M_\infty = 0.4$ and 0.6. The upper and lower sides of the directivity patterns refer to different $\Omega_\infty = 0$, 0.2, 0.4, 0.6. Figure 5.15 shows also the variation of the scattered power level versus the swirling flow angular velocity for constant M_t and m.

The swirling flow does have an effect on the directivity pattern, which is different depending on the case. Both the number and position of the lobes vary. In some cases the downstream lobe is completely shifted. This can be noted for the cases of $M_\infty = 0.6$, $m = 8$, and $M_\infty = 0.4$, $m = -8$ ($\Omega_\infty = 0.6$). In general, as predicted analytically [69], the swirling flow decreases the modal content when co-rotating with the spinning azimuthal order of the incident source, fewer lobes corresponds to fewer cut-on modes [13]. For positive m, the trend of the scattered power level is overall decreasing with Ω_∞, while for negative m the effect is opposite and less evident. On the other hand, the scattered pressure directivity pattern becomes wider when increasing Ω_∞.

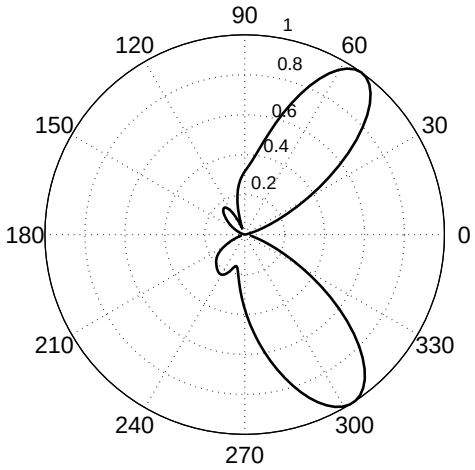

a) $\mathbf{M_t = 1.0,\ \Omega_\infty = 0}$ **(upper side),** $\mathbf{\Omega_\infty = 0.2}$ **(lower side)**

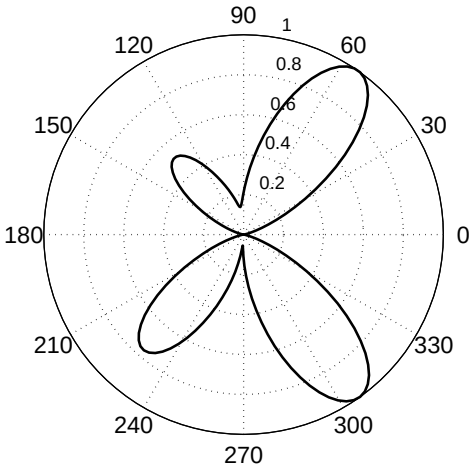

b) $\mathbf{M_t = 1.0, \Omega_\infty = 0.4}$ **(upper side),** $\mathbf{\Omega_\infty = 0.6}$ **(lower side)**

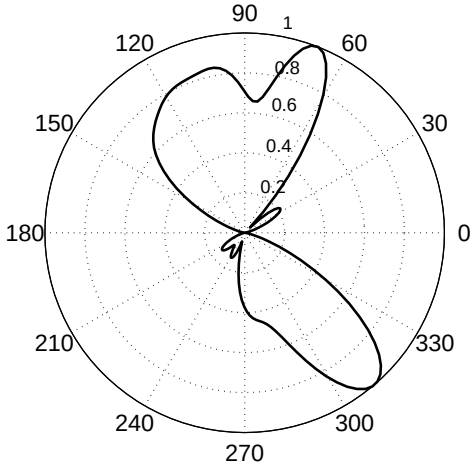

c) $\mathbf{M_t = 1.2,\ \Omega_\infty = 0}$ **(upper side),** $\mathbf{\Omega_\infty = 0.2}$ **(lower side)**

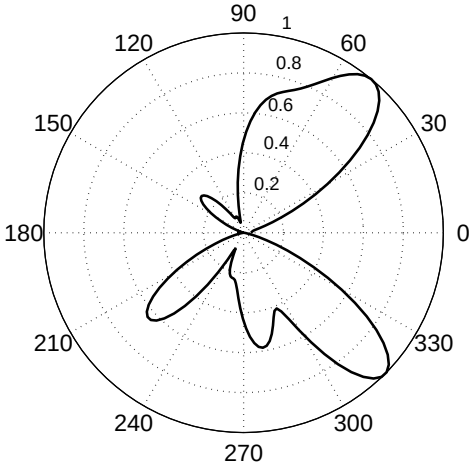

d) $\mathbf{M_t = 1.2, \Omega_\infty = 0.4}$ **(upper side),** $\mathbf{\Omega_\infty = 0.6}$ **(lower side)**

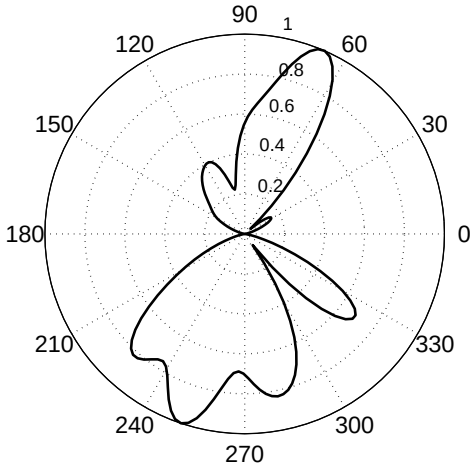

e) $\mathbf{M_t = 1.4,\ \Omega_\infty = 0}$ **(upper side),** $\mathbf{\Omega_\infty = 0.2}$ **(lower side)**

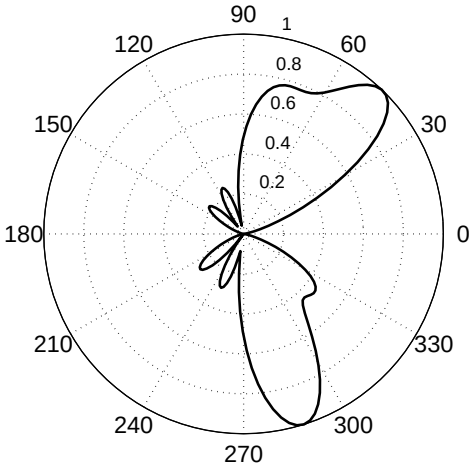

f) $\mathbf{M_t = 1.4, \Omega_\infty = 0.4}$ **(upper side),** $\mathbf{\Omega_\infty = 0.6}$ **(lower side)**

Figure 5.10: Directivity pattern of the normalized scattered pressure for varying Ω_∞; $m = 4$, $M_\infty = 0.4$.

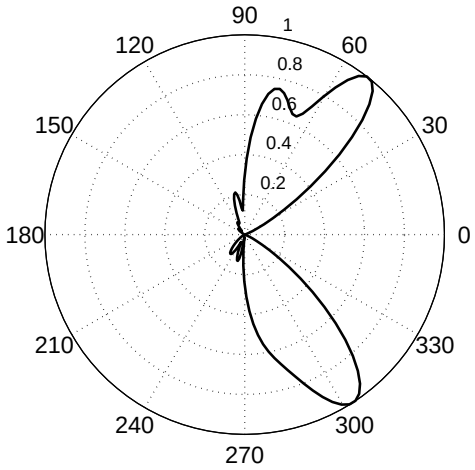

a) $\mathbf{M_t = 1.0,\ \Omega_\infty = 0}$ **(upper side),** $\mathbf{\Omega_\infty = 0.2}$ **(lower side)**

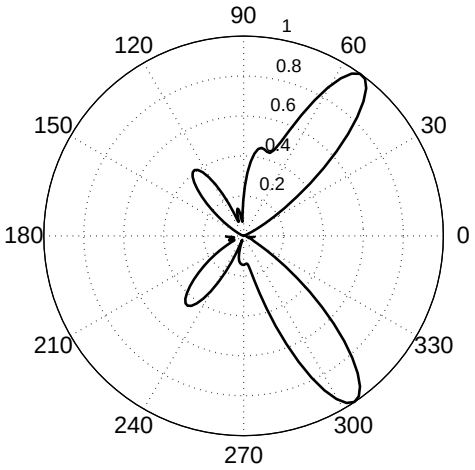

b) $\mathbf{M_t = 1.0, \Omega_\infty = 0.4}$ **(upper side),** $\mathbf{\Omega_\infty = 0.6}$ **(lower side)**

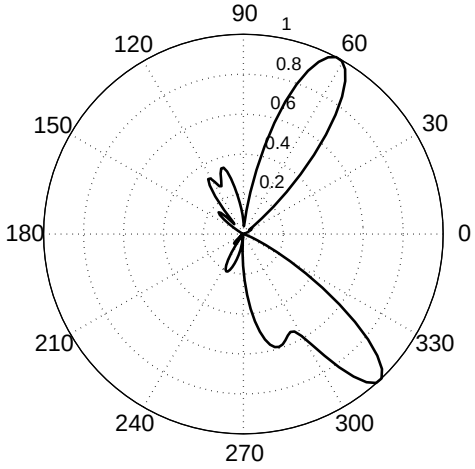

c) $\mathbf{M_t = 1.2,\ \Omega_\infty = 0}$ **(upper side),** $\mathbf{\Omega_\infty = 0.2}$ **(lower side)**

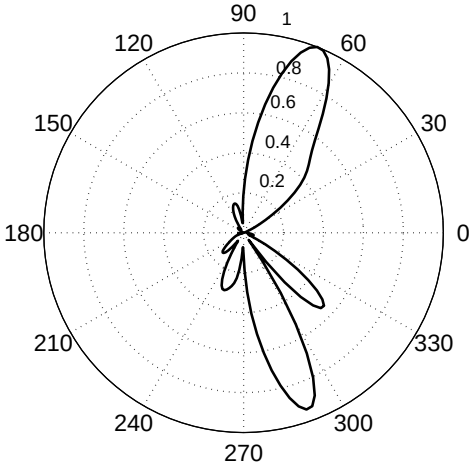

d) $\mathbf{M_t = 1.2, \Omega_\infty = 0.4}$ **(upper side),** $\mathbf{\Omega_\infty = 0.6}$ **(lower side)**

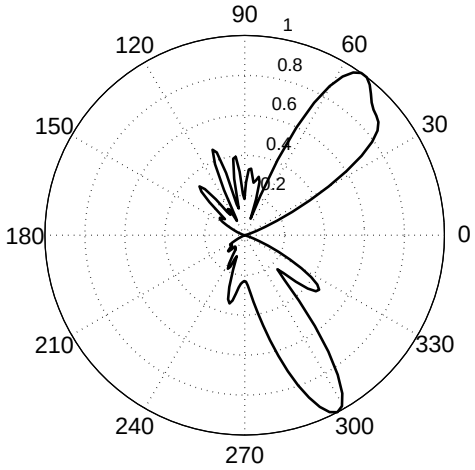

e) $\mathbf{M_t = 1.4,\ \Omega_\infty = 0}$ **(upper side),** $\mathbf{\Omega_\infty = 0.2}$ **(lower side)**

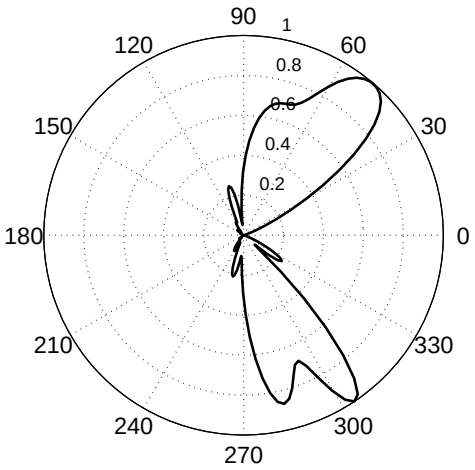

f) $\mathbf{M_t = 1.4, \Omega_\infty = 0.4}$ **(upper side),** $\mathbf{\Omega_\infty = 0.6}$ **(lower side)**

Figure 5.11: Directivity pattern of the normalized scattered pressure for varying Ω_∞; $m = 8$, $M_\infty = 0.4$.

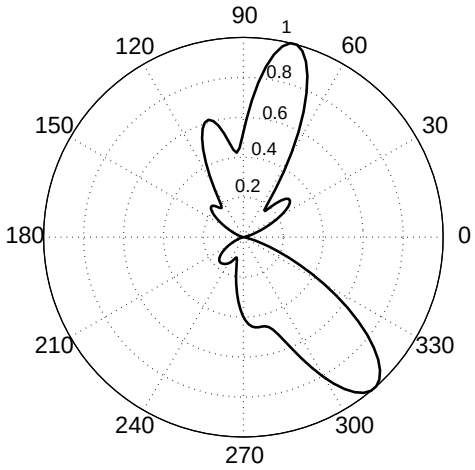

a) $\mathbf{M_t = 1.0,\ \Omega_\infty = 0}$ **(upper side),** $\mathbf{\Omega_\infty = 0.2}$ **(lower side)**

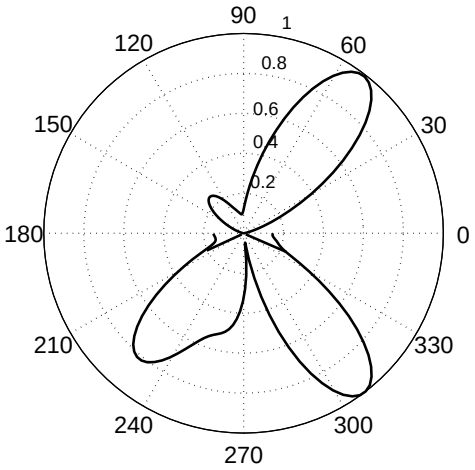

b) $\mathbf{M_t = 1.0, \Omega_\infty = 0.4}$ **(upper side),** $\mathbf{\Omega_\infty = 0.6}$ **(lower side)**

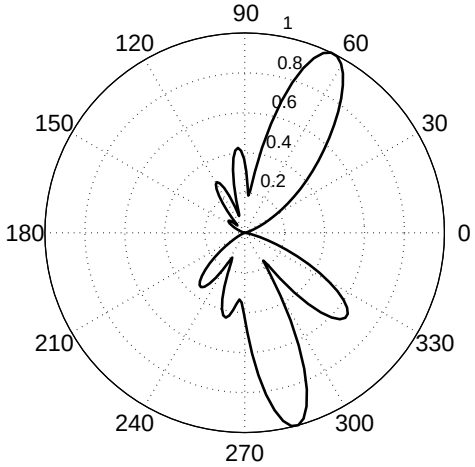

c) $\mathbf{M_t = 1.2,\ \Omega_\infty = 0}$ **(upper side),** $\mathbf{\Omega_\infty = 0.2}$ **(lower side)**

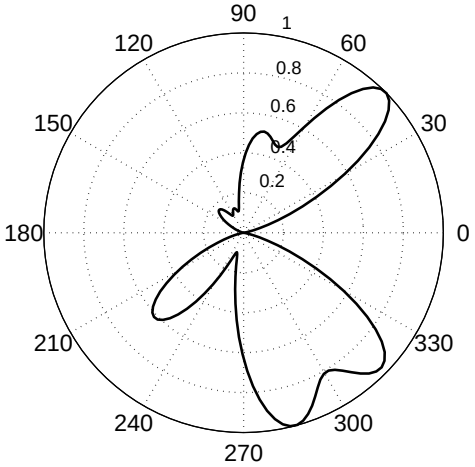

d) $\mathbf{M_t = 1.2, \Omega_\infty = 0.4}$ **(upper side),** $\mathbf{\Omega_\infty = 0.6}$ **(lower side)**

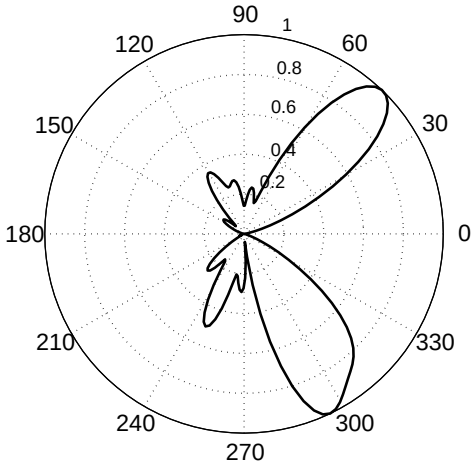

e) $\mathbf{M_t = 1.4,\ \Omega_\infty = 0}$ **(upper side),** $\mathbf{\Omega_\infty = 0.2}$ **(lower side)**

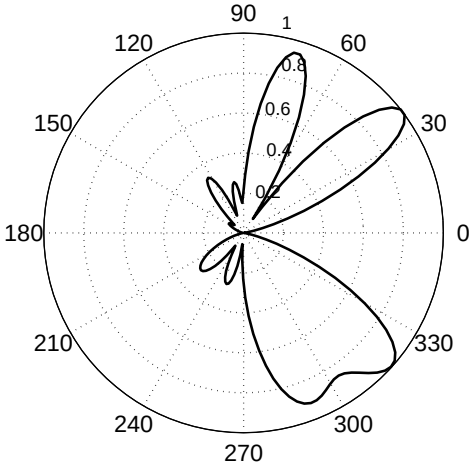

f) $\mathbf{M_t = 1.4, \Omega_\infty = 0.4}$ **(upper side),** $\mathbf{\Omega_\infty = 0.6}$ **(lower side)**

Figure 5.12: Directivity pattern of the normalized scattered pressure for varying Ω_∞; $m = 4$, $M_\infty = 0.6$.

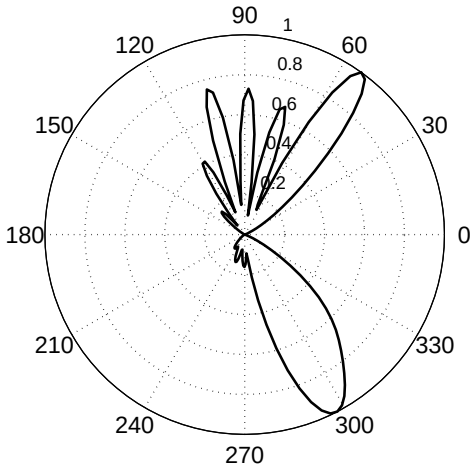

a) $\mathbf{M_t = 1.0,\ \Omega_\infty = 0}$ **(upper side),** $\mathbf{\Omega_\infty = 0.2}$ **(lower side)**

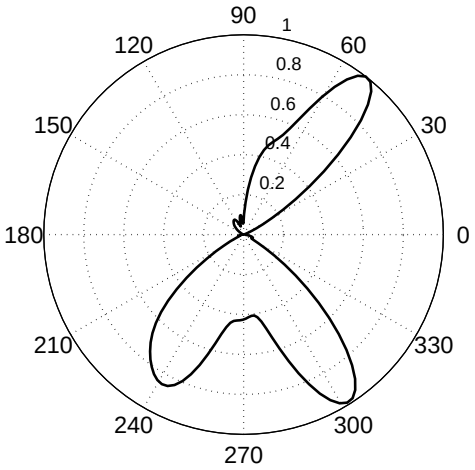

b) $\mathbf{M_t = 1.0, \Omega_\infty = 0.4}$ **(upper side),** $\mathbf{\Omega_\infty = 0.6}$ **(lower side)**

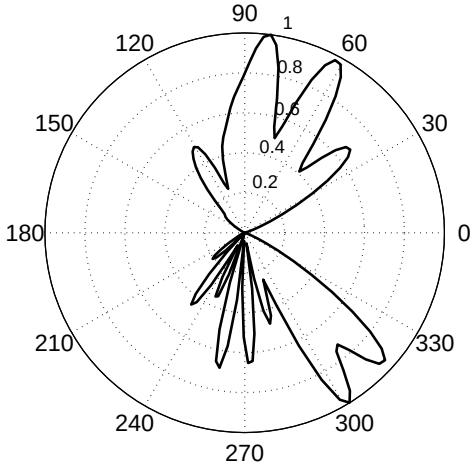

c) $\mathbf{M_t = 1.2,\ \Omega_\infty = 0}$ **(upper side),** $\mathbf{\Omega_\infty = 0.2}$ **(lower side)**

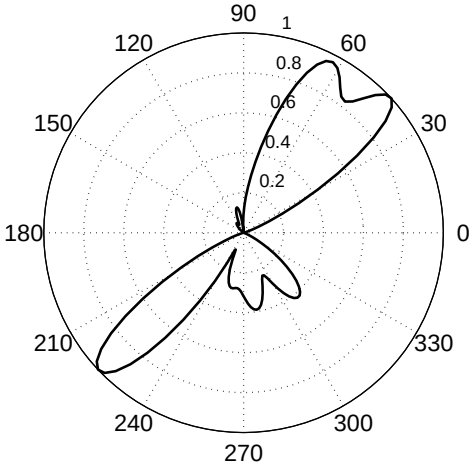

d) $\mathbf{M_t = 1.2, \Omega_\infty = 0.4}$ **(upper side),** $\mathbf{\Omega_\infty = 0.6}$ **(lower side)**

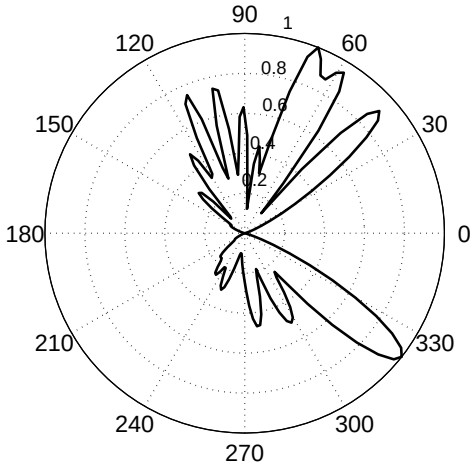

e) $\mathbf{M_t = 1.4,\ \Omega_\infty = 0}$ **(upper side),** $\mathbf{\Omega_\infty = 0.2}$ **(lower side)**

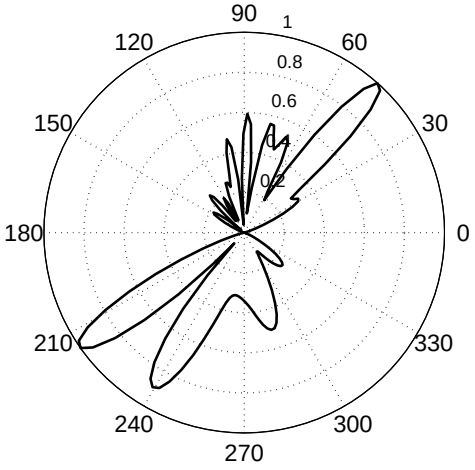

f) $\mathbf{M_t = 1.4, \Omega_\infty = 0.4}$ **(upper side),** $\mathbf{\Omega_\infty = 0.6}$ **(lower side)**

Figure 5.13: Directivity pattern of the normalized scattered pressure for varying Ω_∞; $m = 8$, $M_\infty = 0.6$.

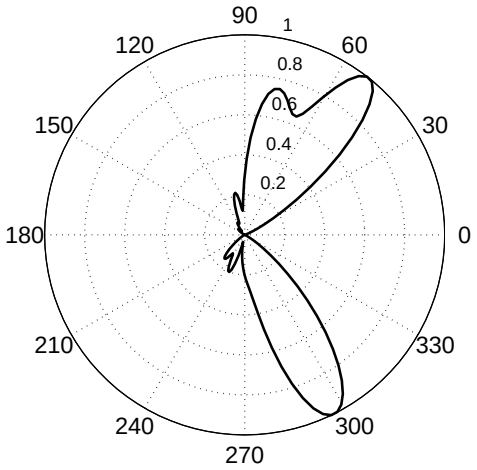

a) $\mathbf{M_t = 1.0,\ \Omega_\infty = 0}$ **(upper side),** $\mathbf{\Omega_\infty = 0.2}$ **(lower side)**

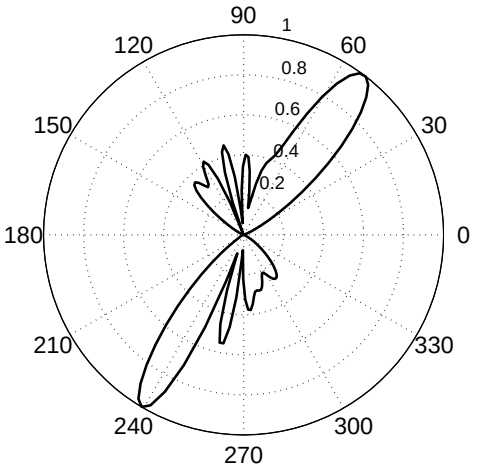

b) $\mathbf{M_t = 1.0, \Omega_\infty = 0.4}$ **(upper side),** $\mathbf{\Omega_\infty = 0.6}$ **(lower side)**

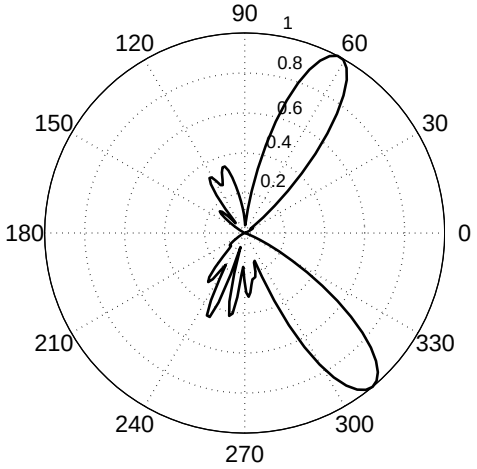

c) $\mathbf{M_t = 1.2,\ \Omega_\infty = 0}$ **(upper side),** $\mathbf{\Omega_\infty = 0.2}$ **(lower side)**

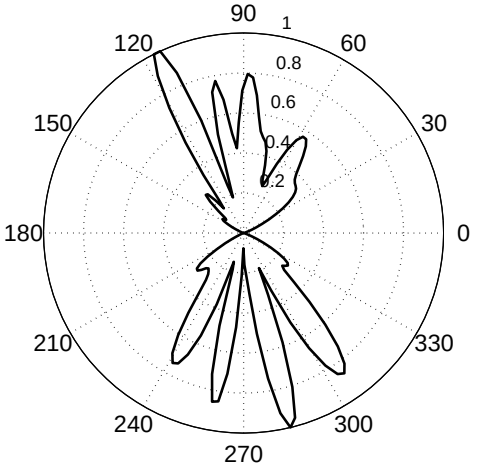

d) $\mathbf{M_t = 1.2, \Omega_\infty = 0.4}$ **(upper side),** $\mathbf{\Omega_\infty = 0.6}$ **(lower side)**

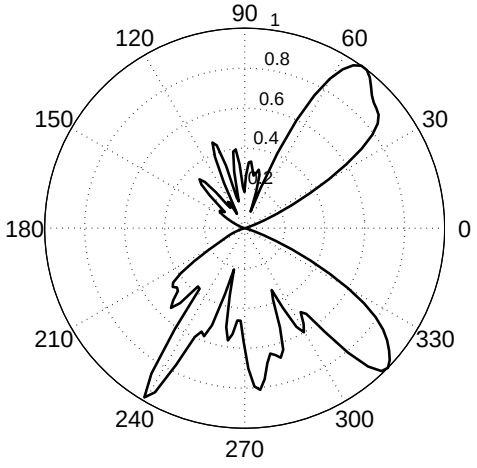

e) $\mathbf{M_t = 1.4,\ \Omega_\infty = 0}$ **(upper side),** $\mathbf{\Omega_\infty = 0.2}$ **(lower side)**

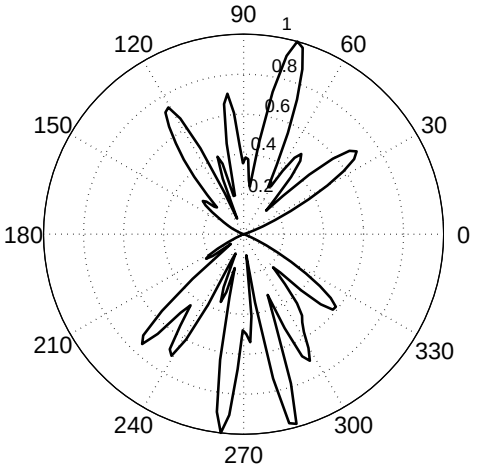

f) $\mathbf{M_t = 1.4, \Omega_\infty = 0.4}$ **(upper side),** $\mathbf{\Omega_\infty = 0.6}$ **(lower side)**

Figure 5.14: Directivity pattern of the normalized scattered pressure for varying Ω_∞; $m = -8$, $M_\infty = 0.4$.

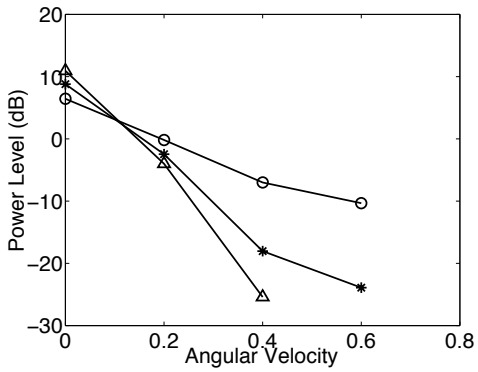

a) $\mathbf{M_t = 1.0}$, $\mathbf{M_\infty = 0.4}$

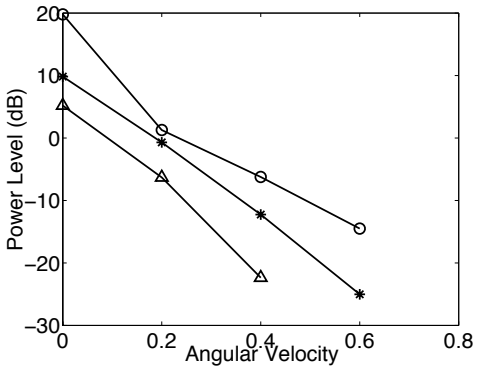

b) $\mathbf{M_t = 1.2}$, $\mathbf{M_\infty = 0.4}$

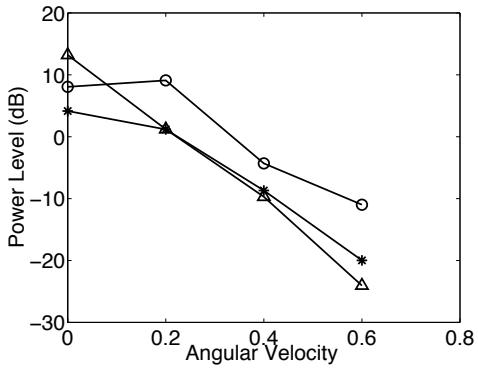

c) $\mathbf{M_t = 1.4}$, $\mathbf{M_\infty = 0.4}$

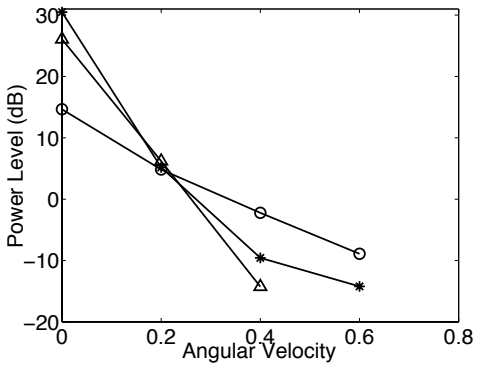

d) $\mathbf{M_t = 1.0}$, $\mathbf{M_\infty = 0.6}$

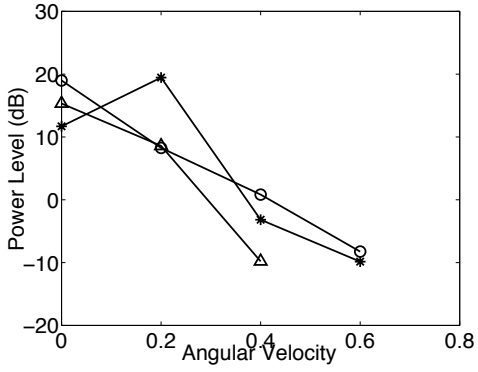

e) $\mathbf{M_t = 1.2}$, $\mathbf{M_\infty = 0.6}$

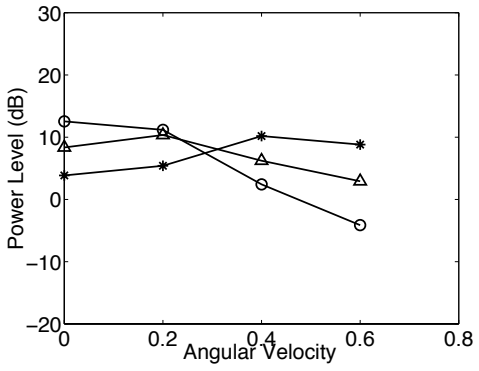

f) $\mathbf{M_t = 1.4}$, $\mathbf{M_\infty = 0.6}$

Figure 5.15: Variation of the scattered power level versus Ω_∞, for constant m: lines $-\circ-$ $m = 4$, $-*-$ $m = 8$, $-\triangle-$ $m = 12$. The difference is calculated with respect to the case where there is no mean flow.

Chapter 6

Effect of a Swirling-Translating Mean Flow. Near Field Propagation.

In this chapter the analysis presented in the previous chapter is extended to investigate the model performance in the near field. The purpose is to further validate the model, according to the modal analysis, and better investigate the modification of the duct propagation patterns due to the swirling-translating mean flow.

6.1 Spinning rotor source results in the near field

The investigation was performed using the spinning rotor source model (Eq. (3.91b)) and the duct geometry (Fig. 4.2) previously defined. Both the source and the mean flow parameters were varied according to the study of the far field propagation: spinning source azimuthal order $m = 4$, 8, 12 and blade tip Mach number $M_t = 0.8$, 1.0, 1.2, 1.4; mean flow Mach number $M_\infty = 0.2$, 0.4, 0.6 and rotation velocity $\Omega_\infty = 0.2$, 0.4, 0.6.

The scattered pressure field was evaluated on a plane longitudinal to the duct (the plane $z = 0$) considering two scenarios: (i) propagation in the mean flow inside the duct and its neighborhood; (ii) propagation in absence of mean flow in the field surrounding the fictitious cylinder (Fig. 5.2), which was previously defined to

evaluate the far field directivity patterns.

Firstly, the effects of the translation and rotation of the mean flow on the in-duct scattered pressure field were separately investigated. Then, the comparison between the scattered pressure fields, in-duct and around the cylinder, was performed to analyze the connections between the two.

6.1.1 Translating mean flow effect: varying the Mach number

The in-duct scattered pressure field was plotted on the plane bisecting the duct, by varying the mean flow M_∞ and keeping Ω_∞ constant. The plotting section of the plane extends in $-4 < x < 2$ and in $-2 < y < 2$. Figures 6.1 and 6.2 show the cut-away view of the resultant noise field for $\Omega_\infty = 0.4$, $M_t = 1.4$ and $m = 12$, -12, respectively. The scattered pressure was normalized using $0.5\rho_\infty c^2$ as the pressure scale.

As predicted by the modal analysis (Section 3.1.2) and confirmed by the far field results (Section 5.2.1), when increasing the flow Mach number, the propagation is enhanced, for both the spinning source azimuthal orders, co-rotating ($m = 12$) and counter-rotating ($m =$ -12) with the mean flow. However, the main direction of the propagation is shifted. This effect is opposite for the two opposite orders m. For $m = 12$, when $M_\infty = 0.2$, 0.4, the propagation is mainly downstream, through the intake, whereas, when $M_\infty = 0.6$, the propagation is wider, but manly upstream, through the exhaust. On the contrary, for $m =$ -12, when $M_\infty = 0.2$, 0.4, the propagation is mainly upstream, through the intake, while, when $M_\infty = 0.6$, the propagation is wider still, but mainly downstream, through the intake.

Furthermore, the overall value of the scattered pressure is much higher when the spinning source is counter-rotating with the mean flow. This is in agreement with the far field analysis and is due to the effect of the mean flow rotation, object of the next section.

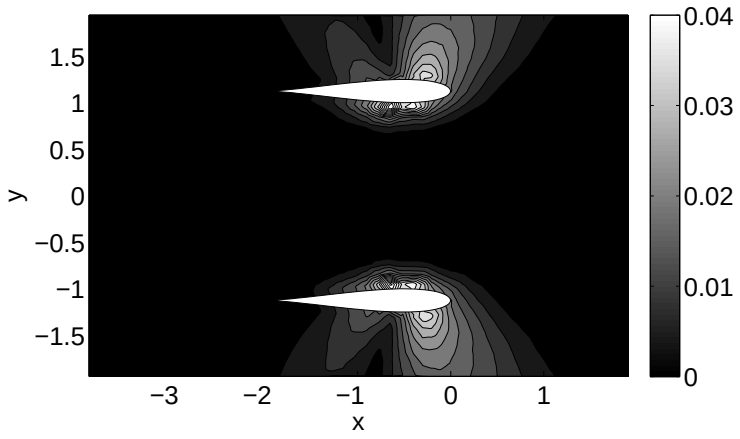

a) $\mathbf{M_\infty = 0.2}$

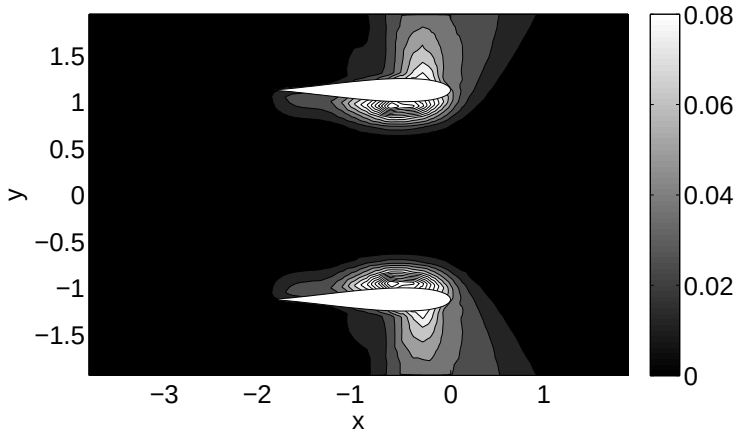

b) $\mathbf{M_\infty = 0.4}$

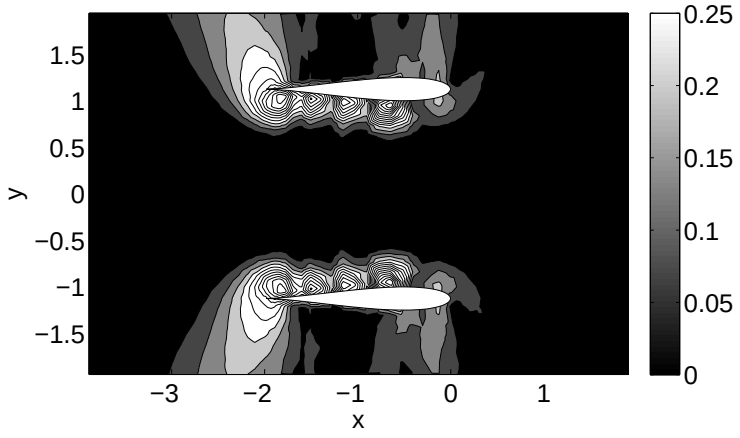

c) $\mathbf{M_\infty = 0.6}$

Figure 6.1: Scattered pressure field on a plane bisecting the duct for varying M_∞; $\Omega_\infty = 0.4$, $m = 12$, $M_t = 1.4$.

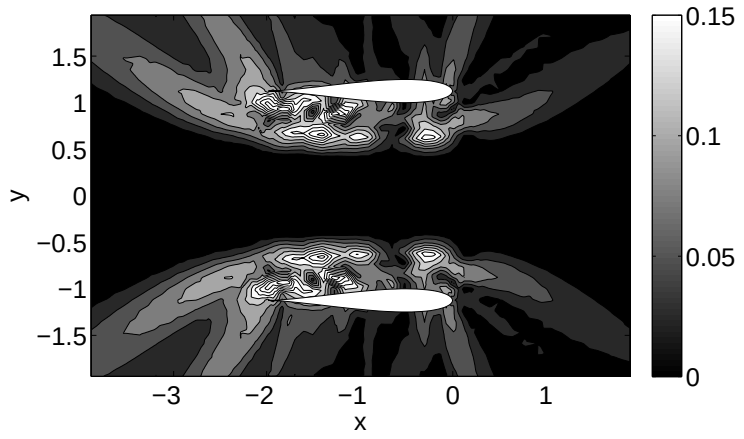

a) $\mathbf{M_\infty = 0.2}$

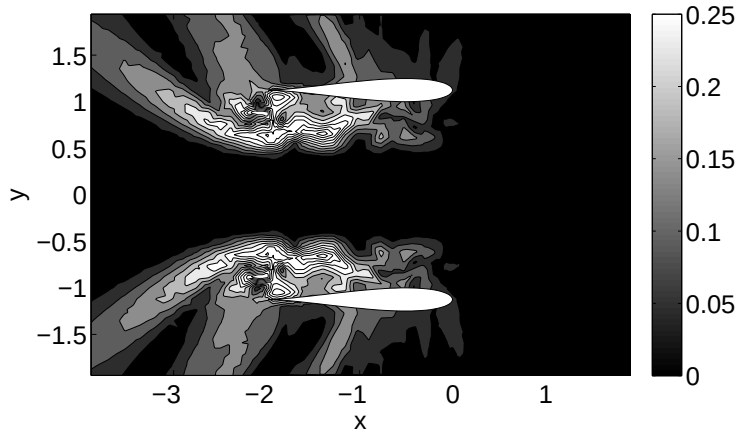

b) $\mathbf{M_\infty = 0.4}$

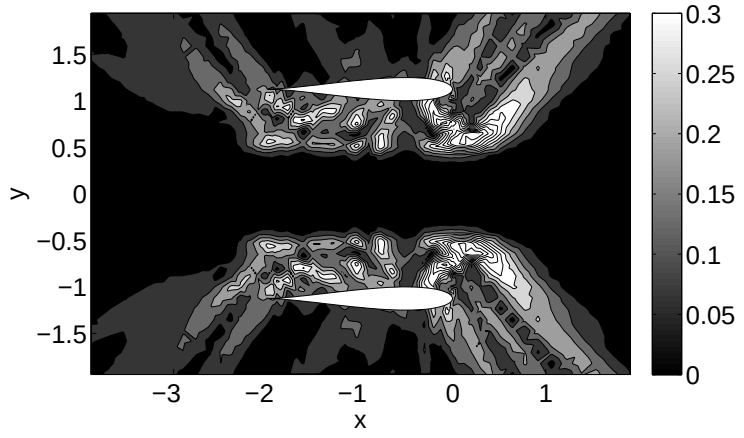

c) $\mathbf{M_\infty = 0.6}$

Figure 6.2: Scattered pressure field on a plane bisecting the duct for varying M_∞; $\Omega_\infty = 0.4$, $m = -12$, $M_t = 1.4$.

6.1.2 Swirling mean flow effect: varying the angular velocity

The in-duct scattered pressure field was plotted on the same section of the bisecting plane defined for the flow Mach number effect analysis, by varying the mean flow Ω_∞ and keeping M_∞ constant. Figures 6.3 and 6.4 show the resulting pattern for $M_\infty = 0.4$, $M_t = 1.4$, 1.0 and $m = 12$, -12, respectively.

In agreement with the modal analysis [69] and the far field results (Section 5.2.2), the effect of the mean flow rotation is opposite for the two opposite spinning source azimuthal orders. When increasing the flow angular velocity, for $m = 12$ (co-rotating), the propagation is reduced, whereas, for $m =$ -12 (counter-rotating), the propagation is highly enhanced. As obtained for the analysis of the mean translating flow effect, the main direction of the propagation is also modified. For $m = 12$, when $\Omega_\infty = 0.2$, 0.4, the noise propagates more downstream, through the intake, but, when $\Omega_\infty =$ 0.6, the scattered pressure field is more intense around the duct external boundaries and the propagation direction is not clearly defined. On the other hand, for $m =$ -12, when $\Omega_\infty = 0.2$, the propagation is very low through the intake, while, when $\Omega_\infty = 0.4$, 0.6, the noise propagates more upstream, through the exhaust, and the scattered pressure values are much higher.

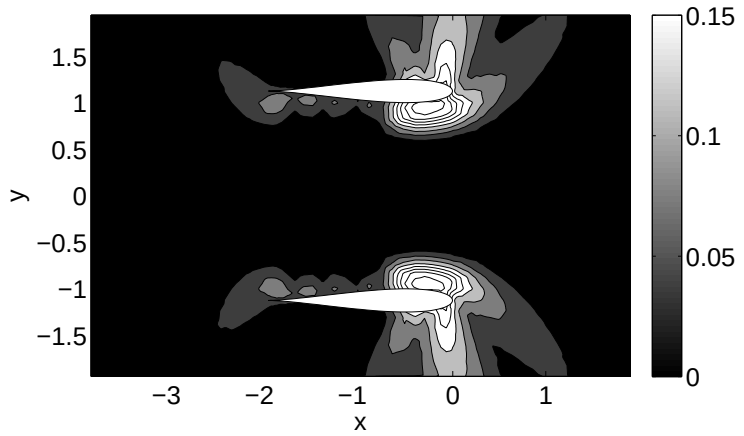

a) $\boldsymbol{\Omega_\infty = 0.2}$

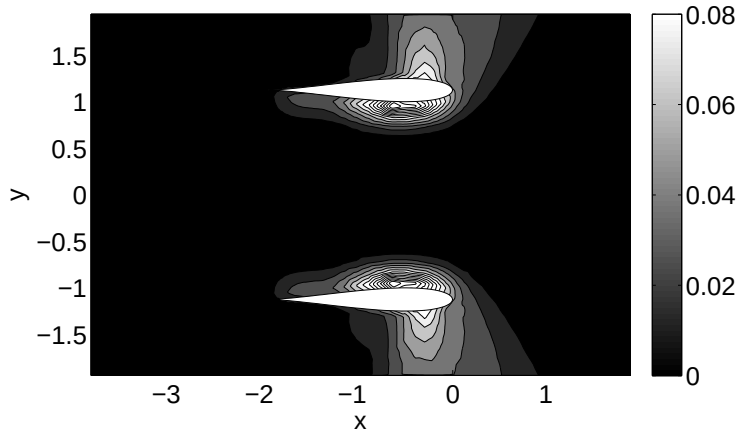

b) $\boldsymbol{\Omega_\infty = 0.4}$

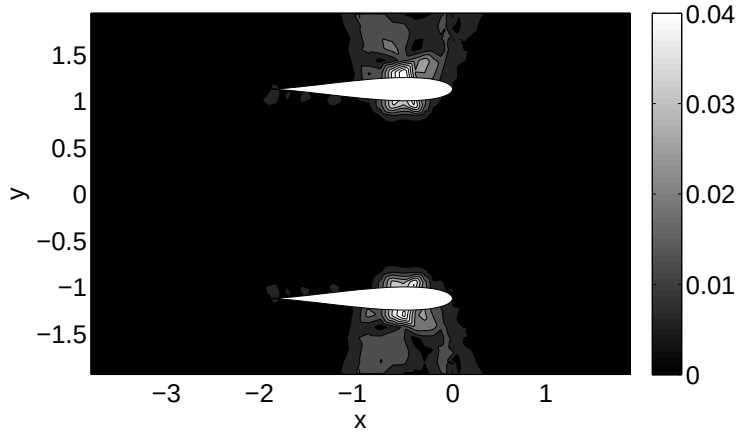

c) $\boldsymbol{\Omega_\infty = 0.6}$

Figure 6.3: Scattered pressure field on a plane bisecting the duct for varying Ω_∞; $M_\infty = 0.4$, $m = 12$, $M_t = 1.4$.

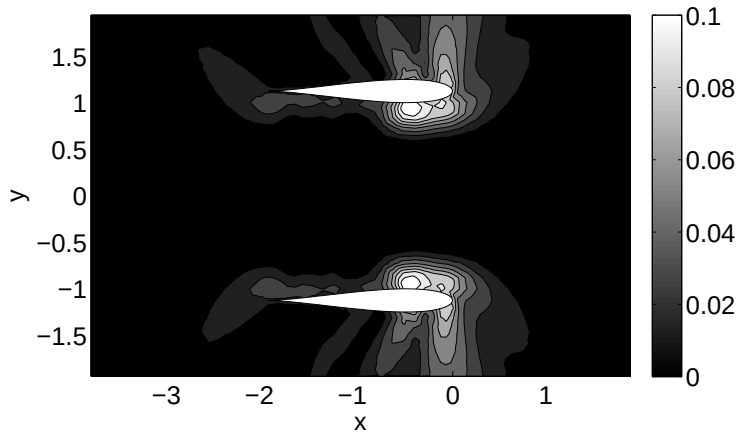

a) $\mathbf{\Omega_\infty = 0.2}$

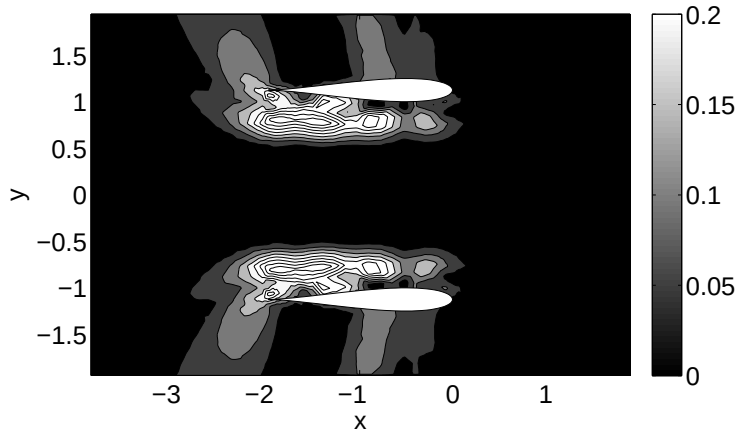

b) $\mathbf{\Omega_\infty = 0.4}$

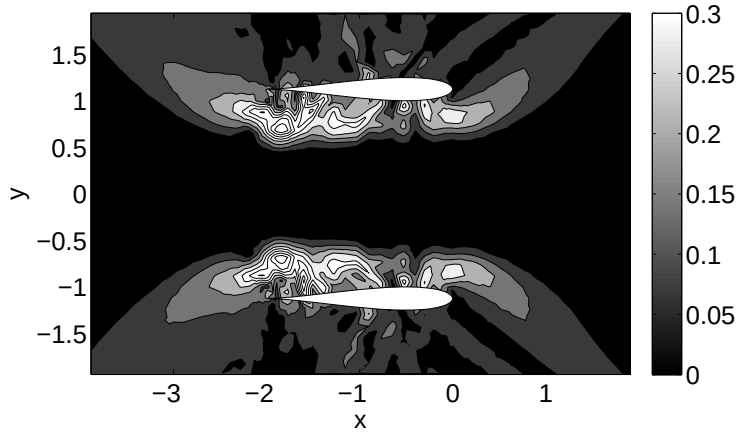

c) $\mathbf{\Omega_\infty = 0.6}$

Figure 6.4: Scattered pressure field on a plane bisecting the duct for varying Ω_∞; $M_\infty = 0.4$, $m = -12$, $M_t = 1.0$.

6.1.3 Comparison of the propagation in the duct and in the no-flow external area

The scattered pressure fields in the mean flow duct region and in the external region embedded in still air were compared. The fictitious cylinder defined for the far field analysis was used to propagate from the duct area to the no-flow near and far field. In order to show the noise field from the cylinder onwards, another section of the plotting plane was defined, surrounding the cylinder, extending in $-4.5 < x < 2.5$ and in $-3 < y < 3$. The comparison was performed using the cut-away views of the resulting noise field on the two sections, i.e. the one bisecting the duct and the one around the cylinder.

In some cases the patterns are in agreement, as shown in Figs. 6.5 and 6.6, referring to the case $M_\infty = 0.6$, $\Omega_\infty = 0.4$, $M_t = 1.2$, $m = 8$,-8. Both the propagations are mainly downstream, throught the intake, but wider for m = -8, due to the mean flow rotation effect. On the other hand, in other cases the propagations in the two regions are in the opposite directions. This is shown in Fig. 6.7, referring to the case $M_\infty = 0.4$, $\Omega_\infty = 0.4$, $M_t = 1.4$, m = -8. The in-duct propagation is mainly upstream, through the exhaust, whereas in the no-flow area it is mainly downstream, through the intake.

The reason for this discrepancy could be that in the transition between the two regions (with and without the mean flow) the flow areas where the scattered pressure is more intense are not necessarily the ones which propagate more in the external no-flow field. In fact, in Fig. 6.8 (case $M_\infty = 0.4$, $\Omega_\infty = 0.6$, $M_t = 1.0$, m = -8) the area around the downstream boundary of the cylinder is clearly intense in scattered pressure, but the one which propagates more is the upstream region. This is confirmed by the far field results, as shown in Fig. 5.14(b). This can also be noted in Fig. 6.9 (case $M_\infty = 0.4$, $\Omega_\infty = 0.6$, $M_t = 1.4$, m = -8), where both the in-duct and the cylinder near fields show an intense scattered pressure area upstream, from the exhaust, but in the no-flow region the propagation is more intense downstream.

Furthermore, Fig. 6.10 shows another interesting effect, occurring generally at M_∞ = 0.6, $\Omega_\infty = 0.6$, $m = 8$. In the near duct region the direction of the propagation is not clear. An intense scattered pressure area is only found on the region around the duct external boundary. However, in the no-flow region the propagation pattern is clear, wide and mainly in the upstream direction.

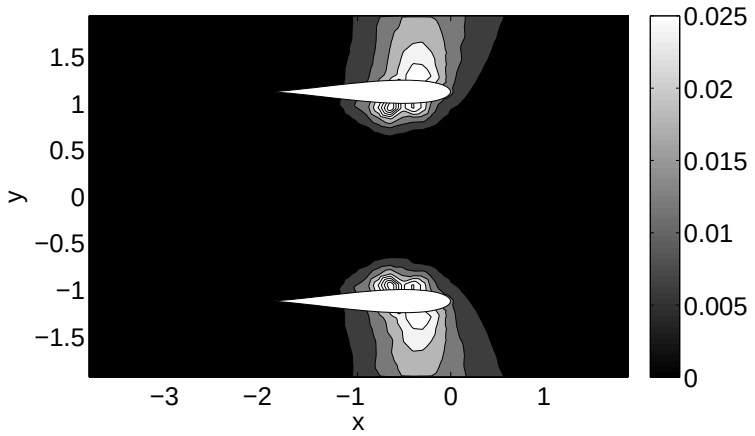

a) Propagation in the duct mean flow

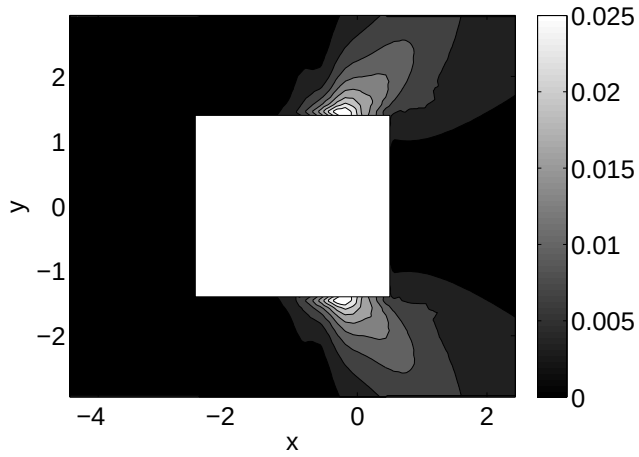

b) Propagation in the no-flow near field

Figure 6.5: Comparison of the scattered pressure in the duct near field (propagation in the mean flow) and in the fictitious cylinder near field (propagation in the absence of mean flow); $M_\infty = 0.6$, $\Omega_\infty = 0.4$, $m = 8$, $M_t = 1.2$.

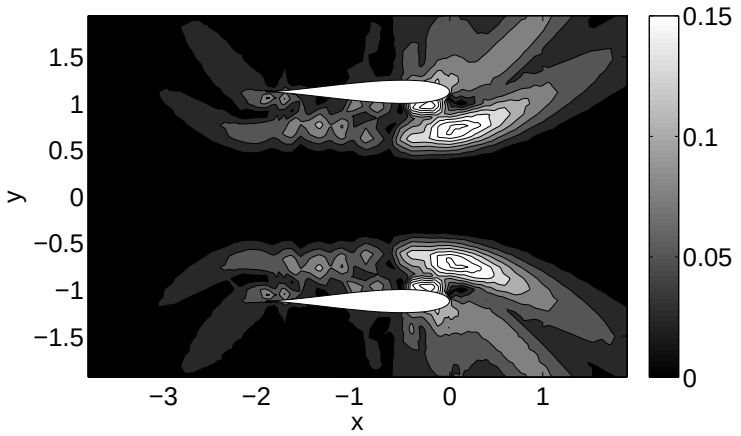

a) Propagation in the duct mean flow

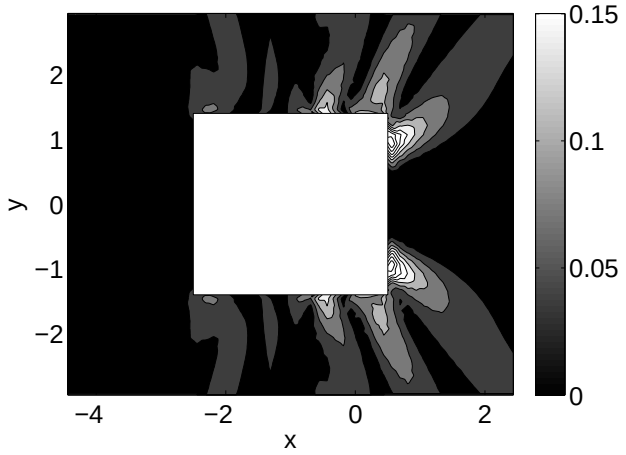

b) Propagation in the no-flow near field

Figure 6.6: Comparison of the scattered pressure in the duct near field (propagation in the mean flow) and in the fictitious cylinder near field (propagation in the absence of mean flow); $M_\infty = 0.6$, $\Omega_\infty = 0.4$, $m = -8$, $M_t = 1.2$.

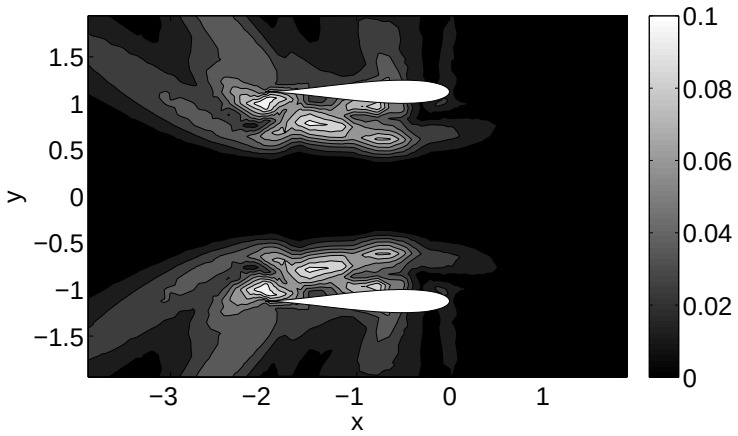

a) Propagation in the duct mean flow

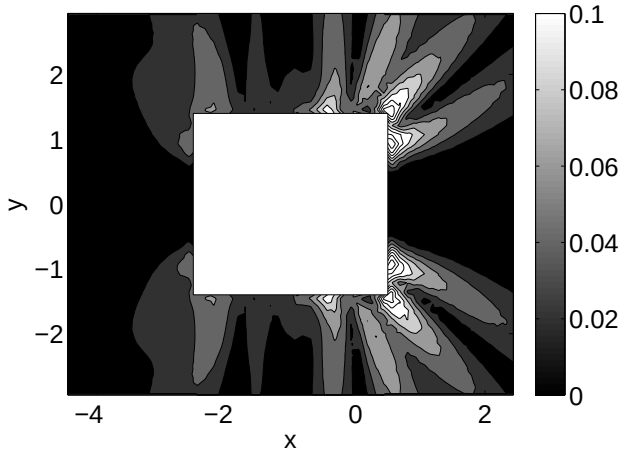

b) Propagation in the no-flow near field

Figure 6.7: Comparison of the scattered pressure in the duct near field (propagation in the mean flow) and in the fictitious cylinder near field (propagation in the absence of mean flow); $M_\infty = 0.4$, $\Omega_\infty = 0.4$, $m = -8$, $M_t = 1.4$.

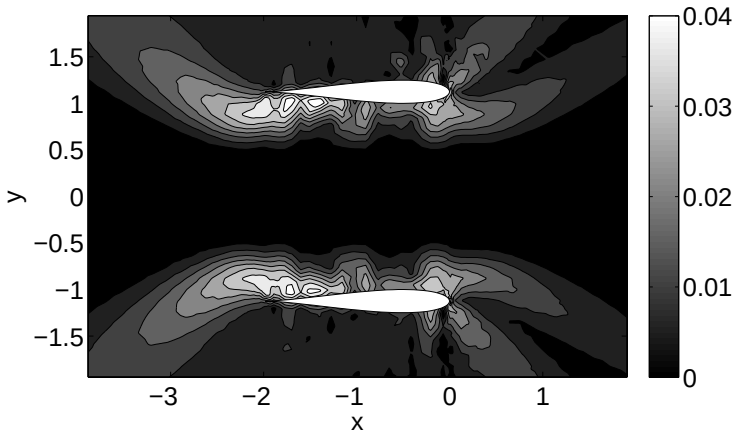

a) Propagation in the duct mean flow

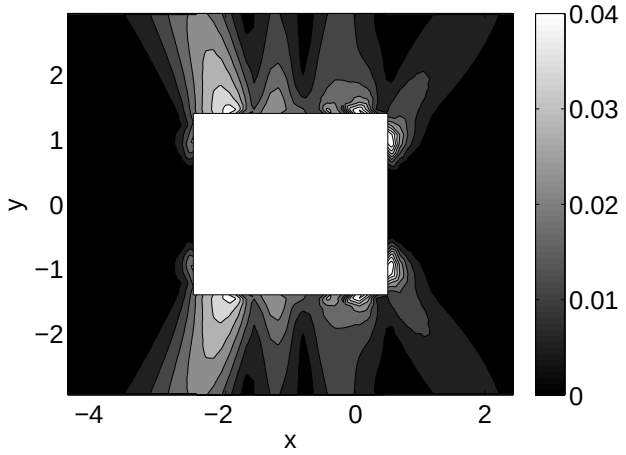

b) Propagation in the no-flow near field

Figure 6.8: Comparison of the scattered pressure in the duct near field (propagation in the mean flow) and in the fictitious cylinder near field (propagation in the absence of mean flow); $M_\infty = 0.4$, $\Omega_\infty = 0.6$, $m = -8$, $M_t = 1.0$.

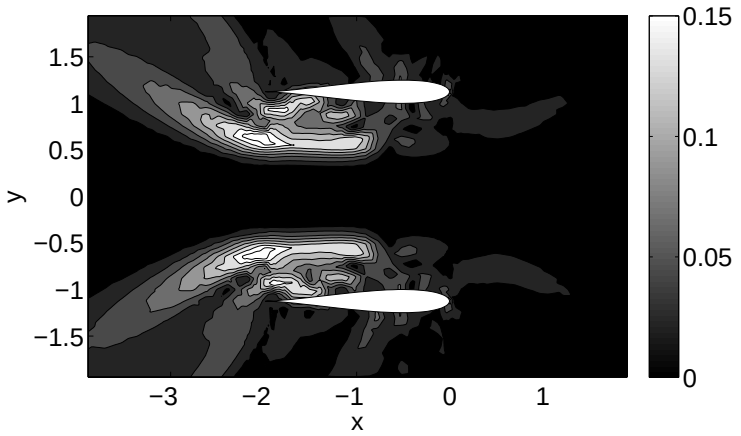

a) Propagation in the duct mean flow

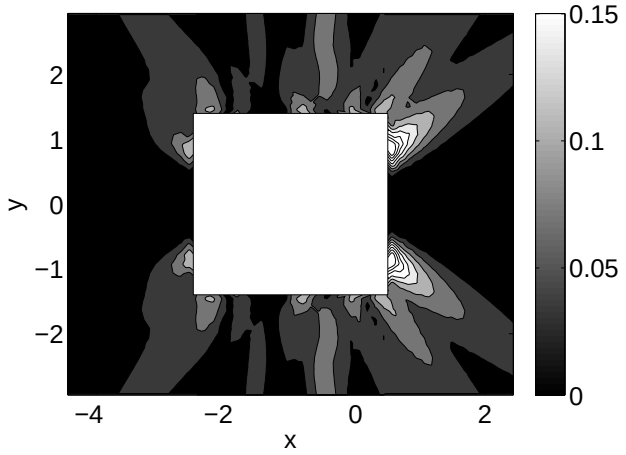

b) Propagation in the no-flow near field

Figure 6.9: Comparison of the scattered pressure in the duct near field (propagation in the mean flow) and in the fictitious cylinder near field (propagation in the absence of mean flow); $M_\infty = 0.4$, $\Omega_\infty = 0.6$, $m = -8$, $M_t = 1.4$.

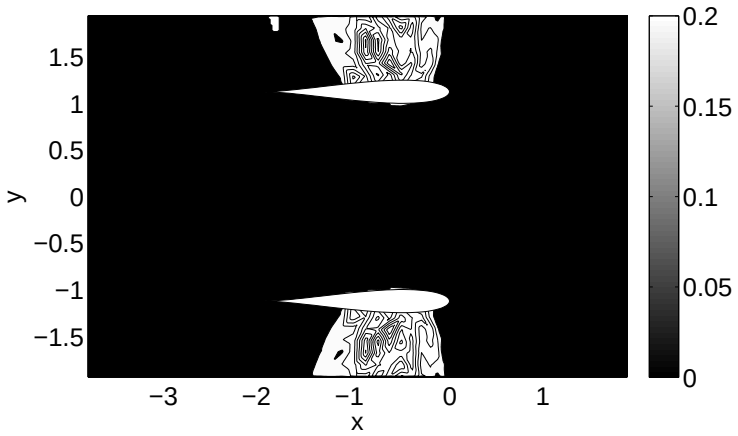

a) Propagation in the duct mean flow

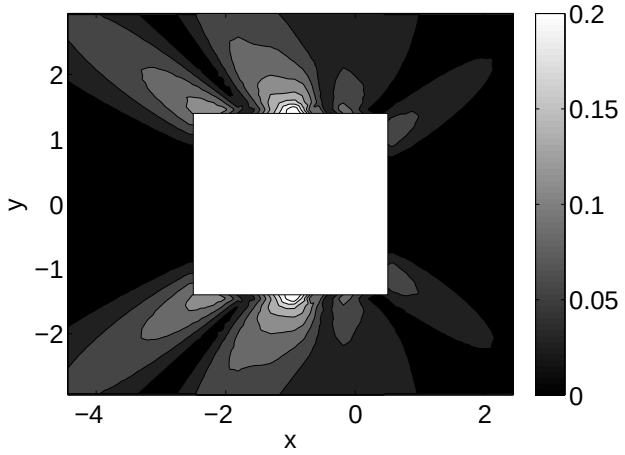

b) Propagation in the no-flow field

Figure 6.10: Comparison of the scattered pressure in the duct near field (propagation in the mean flow) and in the fictitious cylinder near field (propagation in the absence of mean flow); $M_\infty = 0.6$, $\Omega_\infty = 0.6$, $m = 8$, $M_t = 1.4$.

6.1.4 General comments on the in-duct propagation

From the analysis of the scattered pressure field in the duct area, two kinds of propagation can be identified: (i) low propagation, occurring at positive m and low M_∞; (ii) high propagation, occurring at negative m and high M_∞. The former is essentially through the intake, because the source is placed at one quarter of the duct length, towards the intake, and the noise does not propagate through the overall duct. The latter is characterized by a much more intense scattered pressure field which spans all over the duct, propagating both downstream and upstream. Generally, the noise field is higher towards the duct internal boundary, where the mean flow rotation is more effective.

In summary, the effect of the mean flow on the scattered pressure field is, essentially, to change the modal duct characteristics, by increasing or decreasing the noise propagation, therefore, resulting in a strong modification of the patterns. From the analysis of the near field results, this appears to be the main effect, more than a direct modification of the pattern itself.

Chapter 7

Conclusions

In this chapter the main results of the research project are summarized and the research contributions outlined. Furthermore, the questions arisen from this work are identified for a further investigation and future research activities are proposed.

7.1 Summary of the research project

A boundary element method was applied to the study of the noise radiation from a duct with the rotor as an acoustic source. Initially, two rotor source models were compared in absence of mean flow and considering a constant source intensity distribution. The rotor was modelled as a dipole and two components were considered: the thrust, directed along the duct axis, and the drag directed along the azimuth. The two source models were implemented and compared at different frequencies, by varying the acoustic parameters, the source radius, and the distance where the pressure was evaluated in the external field. The results revealed that the source radius is a crucial parameter. Perfect agreement between the normalized scattered pressure directivity patterns was found when the ring to disc radius ratio equals 0.9. Concerning the scattered power levels, the ring source model predicts higher levels, however, varying the tip Mach number M_t for a given azimuthal order m, the difference between the scattered power levels predicted by the two source models is around 1 dB.

The previous investigation was used for the main subject of this research: modelling

the effect of a swirling-translating mean flow on the duct scattered field. It is well known that the convection of sound is strongly modified by the mean fluid flow. In particular, as discussed in Chapter 3 and predicted analytically [69], modes cut on in absence of mean flow can be cut off in presence of a swirling flow co-rotating with the spinning azimuthal order, whereas modes cut off in absence of mean flow can be cut on in presence of a translating flow or a swirling flow counter-rotating with the spinning azimuthal order.

A boundary element method in the frequency domain was derived for scattering problems in conjunction with a spinning rotor source model. The method was applied to study the noise radiation from a duct and the rotor was modelled as a dipole representing the thrust directed along the duct axis, using the ring source model previously investigated.

Both the translating flow Mach number and the swirling flow angular velocity affect the overall noise propagation in the near and far field. The modal analysis showed that the modal content of the scattered field increases when increasing the translating flow Mach number. While, a swirling flow leads to a reduction of the mode propagation, if co-rotating with the azimuthal order, or an increasing of the propagation, if counter-rotating. This is clearly confirmed by the scattered pressure patterns and levels both in the far and in the duct near field for all the source frequencies.

From the in-duct and near field results and looking at the connection between the flow duct area and the no-flow external region in the near field, the comparison shows that in some cases the propagation patterns are in agreement, whereas, for other flow and source conditions they differ. This can be explained by the fact that in the no-flow region close to the cylinder boundaries there are areas of high scattered pressure, derived from the flow duct region, which do not necessarily propagate to the far field.

In summary, from the analysis of the far field results, the mean translating flow moves the main lobes of the directivity patterns downstream, whereas in some cases the mean swirling flow appears to neglect this effect and the downstream lobe is completely shifted. However, a further investigation into the in-duct propagation shows that the main effect of the convecting mean flow is to change the modal duct characteristics, more than the pattern itself. This results in turn in the strong modification of the patterns, also noted in the far field.

7.2 Steps undertaken to accomplish the research objectives

The steps followed to carry out this analysis are here outlined.

- A broad literature survey was conducted to validate the state-of-the-art of duct aeroacoustics and in particular of the BEM for internal aeroacoustic flows.
- Two rotor source models were implemented and their acoustic effect was investigated in the far field, by comparing both the directivity pattern of the scattered pressure and the power levels, varying the frequency and the spinning mode order of the source.
- A BEM approach for a translating-swirling mean flow was derived in the frequency domain from the Morino and Gennaretti's formulation.
- A source model was developed for the incident field including the effect of the translating-swirling mean flow.
- Both the BEM formulation and the source model were implemented in a parallel code using the MPI libraries.
- The far field, in-duct, and near field results were analyzed, varying the flow and source parameters.

7.3 Main research contributions

From the analysis of the two source models, it has been shown that no substantial difference can be related to using a ring or a source model. In spite of the higher complexity of the disc model, it has been shown that in the far field propagation there is a good agreement between the two, and this was also related to a specific ratio of the source radii.

However, the main target of this work was the investigation of the possibility to extend the BEM approach to duct aeroacoustics, by including the effect of complex mean flows. In the literature, BEM has been mainly applied to scattering in absence of mean flow or in case of uniform convecting flow, but a BEM formulation was

proposed for more complex mean flows. This has shown to be able to capture the main features of the duct propagation, in agreement with the duct modal analysis, and could lead to a better understanding of the phenomena involved, also taking advantage of the fully 3D applicability, to model the scattering from more complex geometries.

7.4 Open questions and future work

Several questions need to be investigated further. Concerning the ring and disc source models, the two models are shown to be in agreement on the directivity patterns, for a specific ratio of the source radii, but varying the order m, the difference between the scattered power levels is not constant, it depends on m. Furthermore, the effect of the duct geometry on the models was not investigated. It is clear that, changing the duct response, the directivity pattern changes, but, even if the variations of the source radius do not affect the agreement, the question of the effect of the duct geometry is not addressed here.

Another question regards the specific form of the source intensity used in the analysis. A constant load on the disc or annular modelling the rotor is not realistic. For an actual rotor, the dipole strengths f_x and f_θ are strongly dependent on the azimuth θ. In fact, the turbomachinery blades distort the flow, so that the aerodynamic loads, which depend on the relative velocity between the blade and the incident flow, have a strong azimuthal dependence. All these matters could be object of a future research project.

Furthermore, as a future work, the analysis of the convecting flow effect could be extended by involving the shear flow. This could be done by modelling the shear flow as a wake downstream. The wake is a surface of discontinuity for the velocity potential and can be modelled through an additional surface integral in the boundary integral equation, leading to a modification of the propagation response.

References

[1] L. Morino, "Boundary integral equations in aerodynamics," *Applied Mechanics Reviews*, vol. 46, no. 8, pp. 445–466, 1993.

[2] M. Gennaretti and L. Morino, "A boundary element method for the potential, compressible aerodynamics of bodies in abitrary motion," *Aeronautical Journal*, vol. 96, no. 951, pp. 15–19, 1992.

[3] M. Gennaretti, L. Luceri, and L. Morino, "A unified boundary integral methodology for aerodynamics and aeroacoustics of rotors," *Journal of Sound and Vibration*, vol. 200, no. 4, pp. 467–489, 1997.

[4] A. S. Lyrintzis, "Review: The use of Kirchhoff's method in computational aeroacoustics," *Journal of Fluids Engineering*, vol. 26, no. 7, pp. 665–676, 1994.

[5] J. E. F. Williams and J. E. Hawkings, "Sound generated by turbulence and surfaces in arbitrary motion," in *Philosophical Transaction of the Royal Society of London*, no. 264 in A, pp. 321–342, 1969.

[6] M. Lighthill, "On sound generated aerodynamically. I. General theory," in *Proceedings of the Royal Society*, vol. 221 of *A*, (London), pp. 564–587, 1952.

[7] M. J. Lighthill, "On sound generated aerodynamically. II. Turbulence as a source of sound," in *Proceeding of the Royal Society of London*, no. 222 in A, pp. 1–32, 1954.

[8] M. J. Lighthill, "The bakerian lectures, 1961. Sound generated aerodynamically," in *Proceeding of the Royal Society of London*, no. 267 in A, pp. 147–182, 1962.

[9] K. S. Wang and T. C. Tszeng, "On the radiation of sound from an unflanged circular pipe," *Physical Review*, vol. 73, pp. 383–406, 1948.

[10] J. M. Tyler and T. G. Sofrin, "Axial flow compressor noise studies," in *Transactions of the Society of Automative Engineers*, no. 70, pp. 309–332, 1962.

[11] K. S. Wang and T. C. Tszeng, "Propagation and radiation of sound in a finite length duct," *Journal of Sound and Vibration*, vol. 93, no. 1, pp. 57–79, 1984.

[12] J. B. Keller, "Geometrical theory of diffraction," *Journal of the Optical Society of America*, vol. 52, pp. 116–130, 1962.

[13] C. J. Chapman, "Sound radiation from a cylindrical duct. Part I. Ray structure of the duct modes and of the external field," *Journal of Fluid Mechanics*, vol. 281, pp. 293–311, 1994.

[14] G. M. Keith and N. Peake, "High-wavenumber acoustic radiation from a thin-walled scarfed cylinder," *Journal of Sound and Vibration*, vol. 255, no. 1, pp. 147–160, 2002.

[15] G. M. Keith and N. Peake, "High-wavenumber acoustic radiation from a thin-walled axisymmetric cylinder," *Journal of Sound and Vibration*, vol. 255, no. 1, pp. 129–146, 2002.

[16] R. J. Astley and W. Eversman, "Acoustic transmission in non-uniform ducts with mean flow. part ii: The finite element method," *Journal of Sound and Vibration*, vol. 74, no. 1, pp. 103–121, 1981.

[17] W. Eversman and I. D. Roy, "Ducted fan acoustic radiation including the effects of nonuniform mean flow and acoustic treatment," in *15th AIAA/CEAS Aeroacoustics Conference*, (Long Beach, CA), 1993. AIAA Paper 93–4424.

[18] Y. Kagana, T. Tsuchiya, T. Yamabuchi, H. Kawabe, and T. Fujji, "Finite element simulation of non-linear sound wave propagation," *Journal of Sound and Vibration*, vol. 154, no. 1, pp. 125–145, 1992.

[19] D. Giljohann and M. Bittner, "The three dimensional dtn finite element method for radiation problems of the helmholtz equation," *Journal of Sound and Vibration*, vol. 212, no. 3, pp. 383–394, 1998.

[20] P. Zhang, T. W. Wu, and L. Lee, "A coupled fem/bem formulation for acoustic radiation in a subsonic non-uniform flow," *Journal of Sound and Vibration*, vol. 192, no. 1, pp. 333–347, 1996.

[21] D. Casalino, P. di Francescantonio, and Y. Druon, "Gfd prediction of fan noise propagation," in *10th AIAA/CEAS Aeroacoustics Conference*, (Manchester, UK), 2004. AIAA Paper 2004–2989.

[22] C. K. W. Tam, "Recent advances in computational aeroacoustics," *Fluid Dynamics Research*, vol. 38, no. 9, pp. 591–615, 2006.

[23] A. S. Lyrintzis, "Surface integral methods in computational aeroacoustics - from the (CFD) near-field to the (acoustic) far-field," *International Journal of Aeroacoustics*, vol. 2, no. 2, pp. 95–128, 2003.

[24] C. Polacsek, S. Burguburu, S. Redonnet, and M. Terracol, "Numerical simulations of fan interaction noise using a hybrid approach," *AIAA Journal*, vol. 44, no. 6, pp. 1188–1196, 2006.

[25] S. Redonnet, E. Monoha, and O. Kenning, "Numerical simulation of the downstream fan noise of 3d coaxial engines," in *11th AIAA/CEAS Aeroacoustics Conference*, (Monterey, CA), 2005. AIAA Paper 2005–2816.

[26] D. A. Venditti, D. Ait-Ali-Yahia, M. Robichaud, and G. Girard, "Spectral-element/kirchhoff method for fan-tone directivity calculations," in *11th AIAA/CEAS Aeroacoustics Conference*, (Monterey, CA), 2005. AIAA Paper 2005–2926.

[27] A. Özyörük and V. Ahuja, "Numerical simulation of fore and aft sound fields of a turbofan," *AIAA Journal*, vol. 42, no. 10, pp. 2028–2034, 2004.

[28] S. Zheng, M. Zhuang, and F. Thiele, "Noise prediction and optimization system for turbofan engine inlet duct design," in *10th AIAA/CEAS Aeroacoustics Conference*, (Manchester, UK), 2004. AIAA Paper 2004–3031.

[29] D. G. Crighton, A. P. Dowling, J. E. F. Williams, M. Heckl, and F. G. Leppington, *Modern Methods in Analytical Acoustics*. London: Springer-Verlag, 1992.

[30] Y. Zhao and P. J. Morris, "The prediction of fan exhaust noise propagation," in *12th AIAA/CEAS Aeroacoustics Conference*, (Cambridge, MA), 2006. AIAA Paper 2006–2420.

[31] J. H. Lan, Y. Guo, and C. Breard, "Validation of acoustic propagation code with jt15d static and flight test data," in *10th AIAA/CEAS Aeroacoustics Conference*, (Manchester, UK), 2004. AIAA Paper 2004–2986.

[32] X. Zhang, X. X. Chen, C. L. Morfey, and B. J. Tester, "Computation of spinning modal radiation from an unflanged duct," *AIAA Journal*, vol. 42, no. 9, pp. 1795–1801, 2004.

[33] X. X. Chen, X. Zhang, C. L. Morfey, and P. A. Nelson, "A numerical method for computation of sound radiation from an unflanged duct," *Journal of Sound and Vibration*, vol. 270, no. 4, pp. 573–586, 2004.

[34] D. Nark, F. Farassat, D. S. Pope, and V. Vatsa, "The development of the ducted fan noise propagation and radiation code cduct-larc," in *9th AIAA/CEAS Aeroacoustics Conference*, (Hilton Head, SC), 2003. AIAA Paper 2003–3242.

[35] K. S. Brentner and F. Farassat, "Analytical comparison of the acoustic analogy and kirchhoff formulation for moving surfaces," *AIAA Journal*, vol. 36, no. 8, pp. 1379–1386, 1998.

[36] D. Colton and R. Kress, *Integral Equation Methods in Scattering Theory*. NY: John Wiley & Sons, 1983.

[37] A. J. Burton and G. F. Miller, "The application of integral equation methods to the numerical solution of some exterior boundary-value problems," in *Proceedings of the Royal Society*, vol. 323, (London), pp. 201–210, 1971.

[38] R. Leis, "Über das neumannsche randwertproblem für die helmholtzsche schwingungsgleichung," *Archive for Rational Mechanics and Analysis*, vol. 2, pp. 101–113, 1958.

[39] A. J. Burton, "The solution of Helmholtz equation in exterior domains using integral equations," Tech. Rep. NPL Rept. NAC30, National Physical Laboratory, Teddington, Middlesex, 1973.

[40] H. Schenck, "Improved integral formulation for acoustic radiation problems," *Journal of the Acoustical Society of America*, vol. 44, no. 5, pp. 41–58, 1968.

[41] C. Polacsek and F. Desbois-Lavergne, "Fan interaction noise reduction using a wake generator: experiments and computational aeroacoustics," *Journal of Sound and Vibration*, vol. 265, no. 4, pp. 725–743, 2003.

[42] E. Manoha, G. Elias, B. Troff, and P. Sagaut, "Towards the use of boundary element method in computational aeroacoustics," in *5th AIAA/CEAS Aeroacoustics Conference*, (Bellevue, WA), 1999. AIAA Paper 99–1980.

[43] E. Manoha, X. Juvigny, and F. Roux, "Numerical simulation of aircraft engine installation acoustic effects," in *11th AIAA/CEAS Aeroacoustics Conference*, (Monterey, CA), 2005. AIAA Paper 2005–2820.

[44] J. Chappuis and J. Ricouard, "Aft fan noise shielding by a lifting surface: Analytical, numerical and experimental results," in *12th AIAA/CEAS Aeroacoustics Conference*, (Cambridge, MA), 2006. AIAA Paper 2006–2617.

[45] A. Delnevo, S. L. Saint, G. Sylvand, and I. Terrasse, "Numerical methods: Fast multipole method for shielding effects," in *11th AIAA/CEAS Aeroacoustics Conference*, (Monterey, CA), 2005. AIAA Paper 2005–2971.

[46] R. J. Astley and J. G. Bain, "A three-dimensional boundary element scheme for acoustic radiation in low mach number flows," *Journal of Sound and Vibration*, vol. 109, no. 3, pp. 445–465, 1986.

[47] K. Taylor, "Acoustic generation by vibrating bodies in homentropic potential flow at low mach number," *Journal of Sound and Vibration*, vol. 65, pp. 125–136, 1979.

[48] M. H. Dunn, J. Tweed, and F. Farassat, "The prediction of ducted fan engine noise via a boundary integral equation method," in *2nd AIAA/CEAS Aeroacoustics Conference*, (State College, PA), 1996. AIAA Paper 96–1770.

[49] M. H. Dunn, J. Tweed, and F. Farassat, "The application of a boundary integral equation method to the prediction of ducted fan engine noise," *Journal of Sound and Vibration*, vol. 227, no. 5, pp. 1019–1048, 1999.

[50] B. Yang, T. Q. Wang, and Y. Guan, "An approach to predict ducted fan noise by boundary integral methods," in *11th AIAA/CEAS Aeroacoustics Conference*, (Monterey, CA), 2005. AIAA Paper 2005–3068.

[51] M. K. Myers, "Radiation of sound from a point source in a short duct," Tech. Rep. CP 3355, NASA, 1997. 2nd CAA Workshop on Benchmark Problems, edited by C. K. W. Tam and J. Hardin.

[52] S. Lidoine, H. Batard, S. Troyes, A. Delnevo, and M. Roger, "Acoustic radiation modeling of aeroengine intake comparison between analytical and numerical methods," in *7th AIAA/CEAS Aeroacoustics Conference*, (Maastricht, The Netherlands), 2001. AIAA Paper 2001–2140.

[53] M. K. Myers, "On the acoustic boundary condition in the presence of flow," *Journal of Sound and Vibration*, vol. 71, no. 3, pp. 429–434, 1980.

[54] Y. Druon, S. Lidoine, and M. Roger, "Acoustic radiation modeling of engine exhaust comparison between analytical and numerical methods," in *10th AIAA/CEAS Aeroacoustics Conference*, (Manchester, UK), 2004. AIAA Paper 2004–2990.

[55] A. Mosson, S. Caro, T. Knapen, M. Gontier, L. Enault, and S. Drouilhet-Peyre, "New advance in the use of ACTRAM/TM for nacelle simulations and optimization of ibm clusters for actram parallel computations," in *12th AIAA/CEAS Aeroacoustics Conference*, (Cambridge, MA), 2006. AIAA Paper 2006–2588.

[56] T. W. Wu and L. Lee, "A direct boundary integral formulation for acoustic radiation in a subsonic flow," *Journal of Sound and Vibration*, vol. 175, no. 1, pp. 51–63, 1994.

[57] L. Morino, "A general theory of unsteady compressible potential aerodynamics," Tech. Rep. CR-2464, NASA, 1973.

[58] L. Morino, L. Chen, and E. Suciu, "Steady and oscillatory subsonic and supersonic aerodynamics around complex configurations," *AIAA Journal*, vol. 13, no. 3, pp. 368–374, 1975.

[59] J. L. Kerrebrock, "Small disturbances in turbomachine annuli with swirl," *AIAA Journal*, vol. 15, no. 6, pp. 794–803, 1977.

[60] K. A. Kousen, "Pressure modes in ducted flows with swirl," in *2nd AIAA/CEAS Aeroacoustics Conference*, (State College, PA), 1996. AIAA Paper 96-1679.

[61] V. V. Gobulev and H. M. Atassi, "Acoustic-vorticity waves in swirling flows," *Journal of Sound and Vibration*, vol. 209, no. 2, pp. 203–222, 1998.

[62] A. A. Ali, O. V. Atassi, and H. M. Atassi, "Acoustic eigenmodes in a coannular duct with a general swirling flow," in *6th AIAA/CEAS Aeroacoustics Conference*, (Lahaina, Hawaii), 2000. AIAA Paper 2000–1954.

[63] C. K. W. Tam and L. Auriault, "The wave modes in ducted swirling flows," *Journal of Fluid Mechanics*, vol. 371, pp. 1–20, 1998.

[64] V. V. Gobulev and H. M. Atassi, "Unsteady swirling flows in annular cascades, part 1: Evolution of incident disturbances," *AIAA Journal*, vol. 38, no. 7, pp. 1142 – 1149, 2000.

[65] A. J. Cooper and N. Peake, "Propagation of unsteady disturbances in a slowly varying duct with mean swirling flow," *Journal of Fluid Mechanics*, vol. 445, pp. 207–234, 2001.

[66] A. J. Cooper and N. Peake, "Trapped acoustic modes in aeroengine intakes with swirling flow," *Journal of Fluid Mechanics*, vol. 419, pp. 151–175, 2000.

[67] A. J. Cooper, A. B. Parry, and N. Peake, "Acoustic resonance in aeroengine intake ducts," *Journal of Turbomachinery*, vol. 126, pp. 432 – 441, 2004.

[68] H. M. Atassi, A. A. Ali, O. V. Atassi, and I. V. Vinogradov, "Scattering of incident disturbances by annular cascade in a swirling flow," *Journal of Fluid Mechanics*, vol. 499, pp. 111–138, 2004.

[69] A. J. Cooper and N. Peake, "Upstream-radiated rotor-stator interaction noise in a mean swirling flow," *Journal of Fluid Mechanics*, vol. 523, pp. 219–250, 2005.

[70] C. J. Heaton and N. Peake, "Algebraic and exponential instability of inviscid swirling flow," *Journal of Fluid Mechanics*, vol. 565, pp. 279–318, 2006.

[71] S. Sawyer, M. Nallasamy, and R. Hixon, "Modal decomposition of rotor wake-stator interaction noise in a swirling shear flow," in *43rd AIAA/ASME/SAE/ASEE Joint Propulsion Conference & Exhibit*, (Cincinnati, OH), 2007. AIAA Paper 2007–5039.

[72] M. M. Logue and H. M. Atassi, "Scattering of acoustic waves by a rotor," in *14th AIAA/CEAS Aeroacoustics Conference*, (Vancouver, British Columbia Canada), 2008. AIAA Paper 2008–2989.

[73] M. Carley, "The sound field of a rotor in a stationary duct," *Journal of Sound and Vibration*, vol. 259, no. 5, pp. 1067–1079, 2003.

[74] W.-H. Jeon and D.-J. Lee, "A numerical study on the flow and sound fields of centrifugal impeller located near a wedge," *Journal of Sound and Vibration*, vol. 266, no. 4, pp. 785–804, 2003.

[75] H.-L. Choi and D.-J. Lee, "Development of the numerical method for calculating sound radiation from a rotating dipole source in an opened thin duct," *Journal of Sound and Vibration*, vol. 295, no. 3-5, pp. 739–752, 2006.

[76] M. V. Lowson, "The sound field for singularities in motion," in *Proceedings of the Royal Society (London)*, vol. 286 of *A*, pp. 559–572, 1965.

[77] A. Gerard, A. Berry, and P. Masson, "Control of tonal noise from subsonic axial fan. part 1: Reconstruction of aeroacoustic sources from far-field sound pressure," *Journal of Sound and Vibration*, vol. 288, no. 4-5, pp. 1049–1075, 2005.

[78] C. R. Lowis and P. F. Joseph, "Determining the strength of rotating broadband sources in ducts by inverse methods," *Journal of Sound and Vibration*, vol. 295, no. 3-5, pp. 614–632, 2006.

[79] I. E. Garrick and C. W. Watkins, "A theoretical study of the effect of forward speed on the free-space sound-pressure field around propellers," Tech. Rep. TN 3018, NACA, 1953.

[80] J. W. S. Rayleigh, *The Theory of Sound*. New York, NY: Dover, 1878.

[81] A. D. Pierce, *Acoustics, An Introduction to its Physical Principles and Applications*. Woodbury, NY: The Acoustical Society of America, 1989.

[82] M. E. Goldstein, *Aeroacoustics*. McGraw-Hill, 1976.

[83] M. Carley, "Propeller noise fields," *Journal of Sound and Vibration*, vol. 233, no. 2, pp. 255–277, 2003.

[84] L. Morino and M. Gennaretti, *Computational Nonlinear Mechanics in Aerospace Engineering*, vol. 146 of *AIAA Progress in Aeronautics and Astronautics*. Washington, DC: AIAA, 1992. Boundary integral equation methods for aerodynamics, 279–321.

[85] L. Morino and K. Tseng, *Boundary Element Methods in Nonlinear Fluid Dynamics*. London and New York: Elsevier Applied Science, 1990.

[86] T. Hahn, *CUBA, A Library for Multidimensional Numerical Integration*. Munich, Germany: Max-Planck-Institut für Physik, 2005.

[87] J. Berntsen, T. Espelid, and A. Genz, "An adaptive algorithm for the approximate calculation of multiple integrals," in *ACM Transactions on Mathematical Software*, vol. 17, pp. 437–451, 1991.

[88] R. Piessens, E. de Doncker, C. Uberhuber, and D. Kahaner, *QUADPACK, A Subroutine Package for Automatic Integration.* Berlin, Germany: Springler-Verlag, 1983.

[89] L. S. Blackford, J. Choi, A. Cleary, E. D'Azevedo, J. Demmel, I. Dhillon, J. Dongarra, S. Hammarling, G. Henry, A. Petitet, K. Stanley, D. Walker, and R. C. Whaley, *ScaLAPACK Users' Guide.* Philadelphia, PA: SIAM, 1997.

[90] E. Anderson, Z. Bai, C. Bischof, J. Demmel, J. Dongarra, J. D. Croz, A. Greenbaum, S. Hammarling, A. McKenney, S. Ostrouchov, and D. Sorensen, *LAPACK Users' Guide.* Philadelphia, PA: SIAM, 1995.

[91] J. Choi, J. Dongarra, and D. Walker, "Pb-blas: A set of parallel block basic linear algebra subroutines," in *Proceedings of Scalable High Performance Computing Conference*, (Knoxville, TN), pp. 534–541, IEEE Computer Society Press, 1994.

[92] J. Dongarra and R. C. Whaley, "A user's guide to the BLACS v1.1," Tech. Rep. CS-95-281, University of Tennessee, Knoxville, TN, 1995.

[93] C. L. Lawson, R. J. Hanson, D. Kincaid, and F. T. Krogh, "Basic linear algebra subprograms for fortran usage," in *ACM Transactions on Mathematical Software*, vol. 5, pp. 308–323, 1979.

[94] M. Snir, S. W. Otto, S. Huss-Lederman, D. W. Walker, and J. Dongarra, *MPI: The Complete Reference.* Cambridge, MA: MIT Press, 1995.

[95] A. Geist, A. Beguelin, J. Dongarra, W. Jiang, R. Manchek, and V. Sunderam, *PVM: Parallel Virtual Machine. A Users' Guide and Tutorial for Networked Parallel Computing.* Cambridge, MA: MIT Press, 1994.

[96] M. A. Hamdi and J. M. Ville, "Sound radiation from ducts: Theory and experiments," *Journal of Sound and Vibration*, vol. 107, no. 2, pp. 231–242, 1986.

Appendix A

Model of the Surface Gradient Integral Coefficient

The coefficients H_{kj} of Eq. (3.92) are derived by replacing the surface integral of the potential surface gradient by line integrals. Using the two identities

$$\int_{S_j} \nabla_{S_B} \phi^S \frac{-1}{4\pi \breve{\varrho}_k} dS = \int_{S_j} \nabla_{S_B} \left(\phi^S \frac{-1}{4\pi \breve{\varrho}_k} \right) dS - \int_{S_j} \phi^S \nabla_{S_B} \left(\frac{-1}{4\pi \breve{\varrho}_k} \right) dS, \quad \text{(A.1a)}$$

$$\int_{S_j} \nabla_{S_B} f(\mathbf{x}) dS = \int_{\partial S_j} f(\mathbf{x})\ \mathbf{n}_{\partial S_j} dl \qquad (\forall f(\mathbf{x}) \text{ function on } S_j), \quad \text{(A.1b)}$$

where $\mathbf{n}_{\partial S_j}$ is the outward normal to the boundary of S_j on the plane of S_j, the second integral of Eq. (3.79) can be rewritten as

$$\sum_{j=1}^{N} M_{n_j} e^{-i\omega\theta_{kj}} \mathbf{M}_i \cdot \left(\sum_{h=1}^{4} \frac{\phi_j^S - \phi_{jh}^S}{2} \int_{\partial S_{jh}} \frac{-1}{4\pi \breve{\varrho}_k} \mathbf{n}_{\partial S_{jh}} dl \right), \quad \text{(A.2)}$$

considering the four edges h of the panel. The potential at the boundary edge h is defined as the average between the potential at the panel S_j, ϕ_j^S, and the one at the boundary panel, ϕ_{jh}^S.

Considering the effective value of the index jh in the sum, Eq. (A.2) can be rewritten by collecting all the factors and multiplying each discretized potential ϕ_j^S, as

$$\sum_{j=1}^{N} \frac{M_{n_j}}{2} e^{-i\omega\theta_{kj}} \phi_j^S \mathbf{M}_j \cdot \left(\sum_{h=1}^{4} \int_{\partial S_{jh}} \frac{-1}{4\pi \breve{\varrho}_k} \mathbf{n}_{\partial S_{jh}} dl - \int_{\partial S_{j\alpha 3}} \frac{-1}{4\pi \breve{\varrho}_k} \mathbf{n}_{\partial S_{j\alpha 3}} dl \right.$$
$$\left. - \int_{\partial S_{j\beta 4}} \frac{-1}{4\pi \breve{\varrho}_k} \mathbf{n}_{\partial S_{j\beta 4}} dl - \int_{\partial S_{j\gamma 1}} \frac{-1}{4\pi \breve{\varrho}_k} \mathbf{n}_{\partial S_{j\gamma 1}} dl - \int_{\partial S_{j\delta 2}} \frac{-1}{4\pi \breve{\varrho}_k} \mathbf{n}_{\partial S_{j\delta 2}} dl \right), \quad \text{(A.3)}$$

where $S_{j\alpha}$, $S_{j\beta}$, $S_{j\gamma}$, and $S_{j\delta}$ are the panels at the boundary of S_j, and $\mathbf{n}_{\partial S_{j\alpha 3}}$, $\mathbf{n}_{\partial S_{j\beta 4}}$, $\mathbf{n}_{\partial S_{j\gamma 1}}$, and $\mathbf{n}_{\partial S_{j\delta 2}}$ are the corresponding normals at the edges. Figure (A.1) shows how these quantities are defined according to the local coordinates (ξ, η).

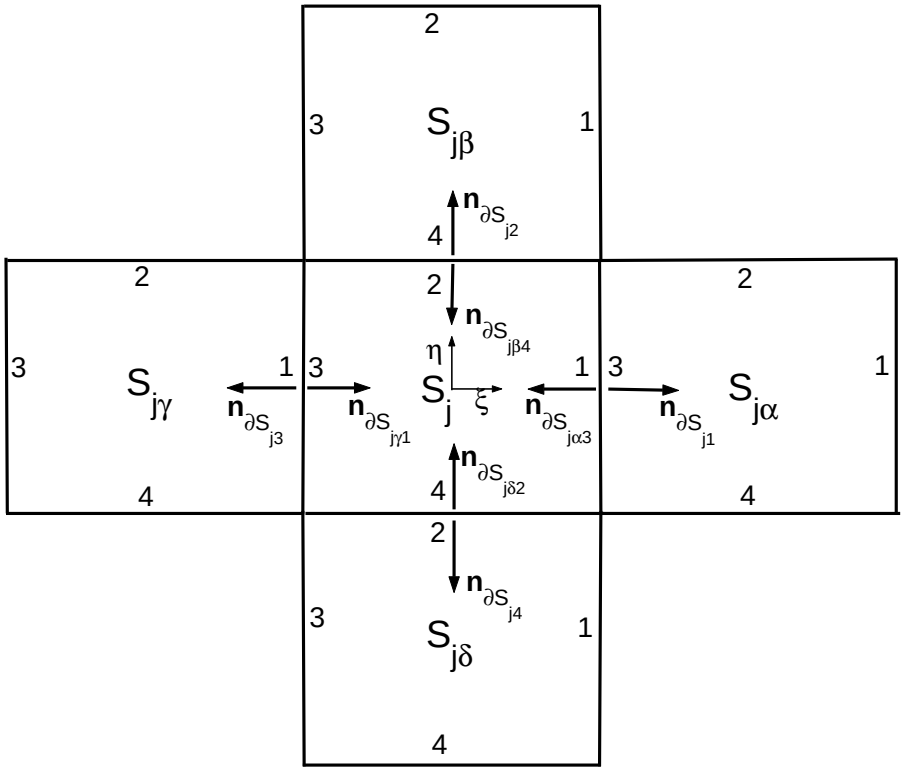

Figure A.1: Definition of the panels, edges, and normals at the S_j boundaries, according to the local coordinates (ξ, η).

Appendix B

Software Organization

Based on the BEM formulations presented in Chapter 3, a few parallel codes were developed to analyze the noise propagation duct characteristics. The codes are implemented in FORTRAN 90 and specifically they are derived from:

1. BIE (3.34) in the no-flow case, used for the acoustic analysis of the rotor source models;
2. BIR (3.34) in the no-flow case, used for the duct noise propagation from the fictitious cylinder to the far field in the absence of mean flow;
3. BIE (3.53) in the translating mean flow case, used for validation purposes;
4. BIE (3.79) in the swirling-translating mean flow case, used for the duct noise propagation in the in-duct and near field and for the propagation from the duct to the fictitious cylinder.

The software is structured so that the body surface discretization is implemented separately from the BEM solver. Two separate codes were developed

- The geometry generator, which deals with the discretized body surface geometry, by providing the arrays storing the panel nodal coordinates and topology;
- The BEM solver, which implements the specific BIE solution in the numerical form.

In this appendix details on the software organization are provided.

B.1 Geometry generator

The code is based on a BEM formulation, therefore the body surface has to be discretized in panel elements. Quadrilater hyperboloidal panels are used. Each panel is identified by four nodes, one centroid, the topology array, which defines the nodes belonging to the panel, and the normal vector to the panel surface.

Every body geometry can be discretized and used for the acoustic scattering analysis, provided that it is a closed body. Several possible geometry discretizations were implemented, among them

- the sphere, used for validation purpose;
- the cylinder duct;
- the axisymmetric duct generated by the complete rotation of a Joukowsky profile;

Figure 4.2 shows some examples of the implemented discretized geometries.

The geometry generator reads all the input data dimensions and geometry parameters from a data file, then it produces unformatted files, storing the panel nodal coordinates and topology, and the coordinates of the points in the external field where the solution is evaluated. The parameters used for the array dimensions are stored in a data file. Furthermore, an output file is generated to plot the discretized geometry and the normal vectors, through a Matlab postprocessor.

In the case of the swirling-translating mean flow the panel nodal coordinates and topology of the fictitious cylinder are also generated to provide the body surface geometry for the code using the BIR in the absence of flow for the propagation to the far field.

B.2 BEM codes

All of the BEM codes are structured through a main module, which sets up the communication among the processors working in parallel and manages the other modules, and three submodules

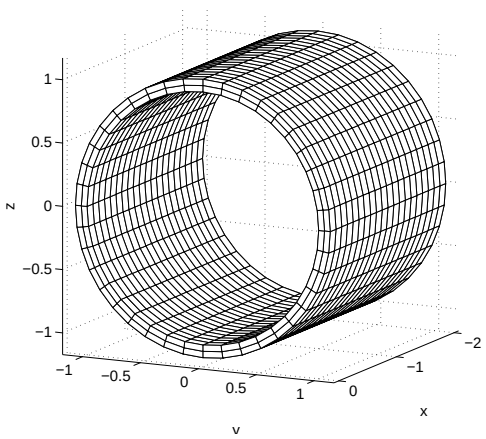

a) Cylinder

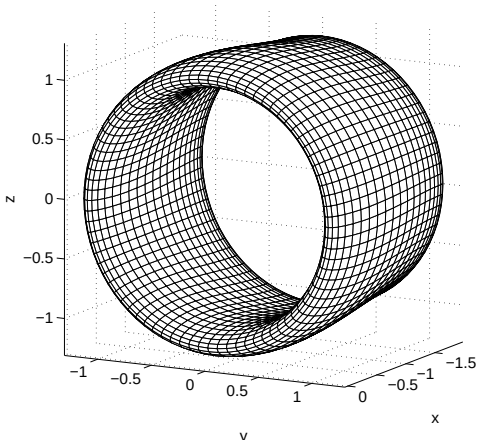

b) Joukowsky profile cylinder

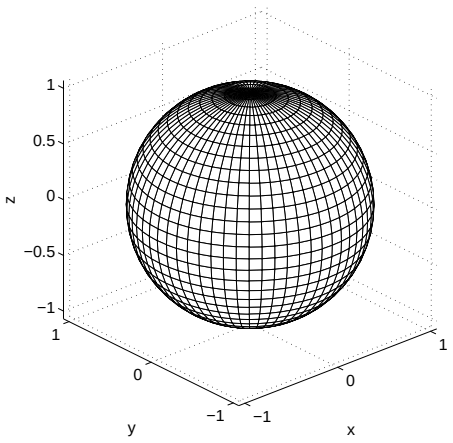

c) Sphere

Figure B.1: Implemented discretized geometries.

1. the module for calculating the integral coefficients on the body surface for the solution of the BIE;

2. the module for calculating the integral coefficients in the field for the solution of the BIR;

3. the solver module for calculating the solution for both the BIE on the body and the BIR in the field.

Only the code based on the BIR in absence of flow does not calculate the solution of the BIE, but uses the scattered velocity potential, output of the code based on the BIE for the swirling-translating mean flow, to calculate the solution in the far field.

Each module writes the parameters necessary to the next module to dimension the arrays on a data file. Furthermore, the modules which calculate the integral coefficients write the output arrays on unformatted files read by the solver module for the BIE and BIR solution.

As the final output, the codes evaluate the acoustic scattered pressure in the volume field, which can be post-processed through a Matlab script to plot either the directivity pattern in the far field or the scattered pressure on the plane bisecting the duct in the near field.

Specifically, in the case of the swirling-translating mean flow there are two possible outputs

- the scattered velocity potential solution on the fictitious cylinder to be post-processed by the code based on the BIR in absence of flow for the propagation to the far field;

- the scattered pressure on the plane bisecting the duct for the in-duct analysis.

Appendix C

Parallel Implementation

The parallel versions of the codes were developed during this project, using the MPI library, which is a communication protocol independent of the computing language used for high performance parallel computers, running on distributed memory system. In order to deal with the solution of the BEM linear system, the BLACS and ScaLAPACK libraries were also employed. The latter provides the linear algebra routines for distributed memory computers, whereas the former is a linear algebra oriented message passing interface, easy to use and portable, used as the communication layer for the ScaLAPACK project.

In general, the parallel programming has the purpose to decrease both run time and allocated memory by dividing the calculation among parallel processors. The steps required can be summarized as

1. Initializing the library (using standard routines);
2. Setting up a processor grid;
3. Mapping the data structure onto the processor grid;
4. Calling the appropriate parallel solver;
5. Recomposing the global solution.

The processor grid is a two-dimensional array whose size and shape is controlled by the program. A processor is identified by its row and column number in the processor grid rather than its traditional MPI identifier or rank. The MPI rank for

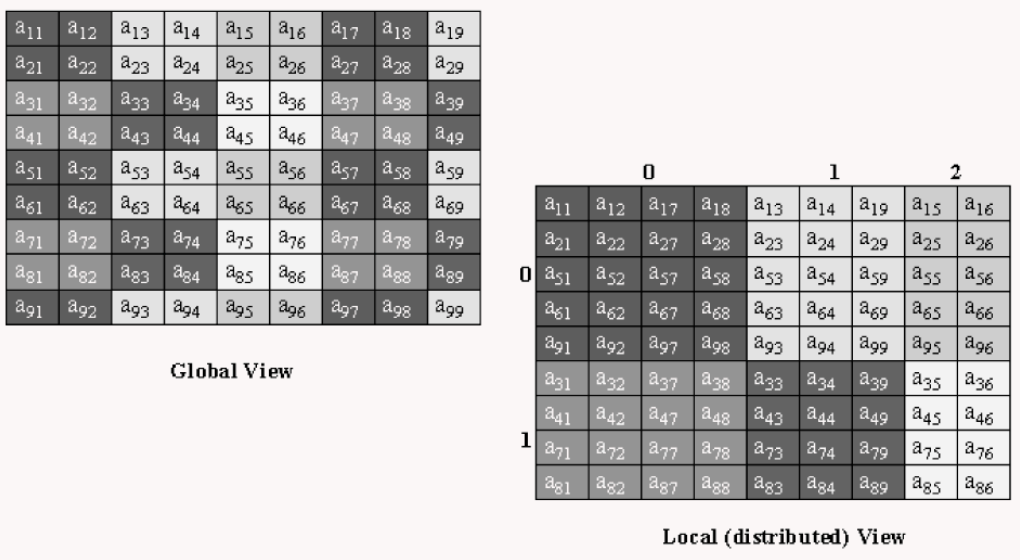

Figure C.1: Distribution of the data among the processors.

a processor is given by its position in the processor grid, for example, in a 2×3 grid where the processors are inserted by row, the processor with MPI rank 4 has grid coordinates (1,2). Note that the row and column numbering both begin with zero.

The work distribution procedure (step 3) is the most important and delicate part of the whole process. It allows each processor to be responsible for the calculation on some subset of the data.

A common approach for creating a parallel version of a matrix solving code is to evaluate the global arrays and split up their elements among the processors, each processor has a local array that holds only the global elements for which it is responsible. In Fig. (C.1) [1] an example of a data distribution is shown. The matrix A is divided in blocks 2×2, each block is allocated to a processor in the 2×3 processor grid, as shown in Figure (C.1), e.g. the processor (0,0) holds all the black blocks. This approach has the advantage that, for an existing code in which the global arrays are already specified (e.g. to work in the serial mode), the only required changes to the code are

1. the inclusion of the local array definition,

2. the modification of the call to the solver itself,

[1] *http://foxtrot.ncsa.uiuc.edu:8900/SCRIPT/PNLIB/scripts/serve_home*

3. the recomposition of the global solution.

On the other hand, this approach has the disadvantage that both the global and the local arrays have to be allocated by each processor, so that, while the parallelization leads to decreased run time, no saving on allocated memory is obtained.

For this reason, a different approach was applied, which fully takes advantage of the parallel work distribution. Instead of working in terms of global variables, it is possible to define (allocate) every array directly as local to the single processor. No global arrays are allocated at all. Basically the two approaches differ because in one the arrays are defined and then split among the processor in the processor grid, while in the other one they are directly defined in the processor grid.

The advantage of the second approach is that each processor allocates and works on its own part of the computation from the beginning to the final solution; hence, the distribution of the matrix is complete. However, the conversion from a serial code to this type of parallel approach requires to rewrite the code completely.

In particular the following procedure was applied. After the communication starts and the processor grid is initialized, each processor mainly takes the following steps (note that here every array is local to the processor itself)

1. evaluating the frequency independent coefficient arrays $\mathrm{Q}^i(\mathbf{x_k})$ $(i = 1, 5)$ and stores them on unformatted files, for the set of collocation points $\mathbf{x_k}$ local to the processor itself;

2. evaluating the boundary condition array $\underline{\chi}^S$ (3.35), applying the QUADPACK and CUBA integration packages;

3. assembling the matrix Z^{C} (3.107);

4. multiplying Z^{C} times $\underline{\chi}^S$, using the ScaLAPACK routine, PCGEMV;

5. assembling the matrix Y^{C} (3.107);

6. evaluating the scattered velocity potential array $\underline{\phi}^S$, by solving the system (3.106) in the least square sense using the ScaLAPACK routine, PCGELS;

7. sending its local solution $\underline{\phi}^S$ to the master processor, which gathers all the local arrays to recompose the global ones.

Specifically, the coefficient arrays $\mathrm{Q}^i(\mathbf{x_k})$ are defined as

$Q_j^1(\mathbf{x_k}) \rightarrow$ source coefficients B_{kj}, Eqs. (3.93a), (3.95a), and (3.97a);

$Q_j^2(\mathbf{x_k}) \rightarrow$ doublet coefficients C_{kj}, Eqs. (3.93b), (3.95b), and (3.97b);

$Q_j^3(\mathbf{x_k}) \rightarrow$ ratelet coefficients D_{kj}, Eqs. (3.93c), (3.95c), and (3.97c);

$Q_j^3(\mathbf{x_k}) \rightarrow$ ratelet coefficients H_{kj}, Eqs. (3.93d) and (3.97d);

$Q_j^5(\mathbf{x_k}) \rightarrow$ acoustic delay coefficients θ_{kj}, Eqs. (3.94), (3.96), and (3.98).

Once the solution is evaluated in terms of the body scattered velocity potential, the solution in the field is obtained by means of Eq. (3.102). The coefficient arrays Q_V^i are evaluated in the acoustic volume field and the scattered velocity potential ϕ_V^S is obtained following the same steps described above, but replacing the step (d) with another call to the ScaLAPACK routine, PCGEMV. Then, use of the linearized Bernouilli's theorem (3.36), (3.82) gives the scattered pressure p_V^S.